PPLN-WAVEGUIDE BASED ENTANGLED-PHOTON SOURCES FOR MULTI-USER QKD OVER METROPOLITAN-SCALE FIBER-OPTIC NETWORKS

VIKASH KUMAR YADAV

DEPARTMENT OF PHYSICS

INDIAN INSTITUTE OF TECHNOLOGY DELHI

APRIL 2025

PPLN-waveguide based entangled-photon sources for multi-user QKD over metropolitan-scale fiber-optic networks

A THESIS

submitted by

Vikash Kumar Yadav

Department of Physics

in partial fulfillment of the requirements for the degree of

Doctor of Philosophy

to the

INDIAN INSTITUTE OF TECHNOLOGY DELHI

APRIL 2025

Dedicated to my parents and my wife

Certificate

This is to certify that the thesis entitled **"PPLN-waveguide based entangled-photon sources for multi-user QKD over metropolitan-scale fiber-optic networks"**, submitted by **Vikash Kumar Yadav** to the **Indian Institute of Technology Delhi**, for the award of the degree of **Doctor of Philosophy** in **Physics**, is a record of the original, bonafide research work carried out by him under our supervision and guidance. The thesis has reached the standards fulfilling the requirements of the regulations related to the award of the degree.

The results contained in this thesis have not been submitted in part or in full to any other University or Institute for the award of any degree or diploma to the best of our knowledge.

Prof. Joyee Ghosh
Associate Professor
Department of Physics
Indian Institute of Technology Delhi

Prof. Vivek Venkataraman
Associate Professor
Department of Electrical Engineering
Indian Institute of Technology Delhi

Date:
Place:

Acknowledgements

I want to express my heartfelt gratitude to everyone who supported me in this Ph.D. journey.

First and foremost, I would like to thank my supervisors, Prof. Joyee Ghosh and Prof. Vivek Venkataraman, for their invaluable guidance, encouragement, and advice throughout my research. Their guidance, trust, and continuous support have shaped my research. I am indebted to my mentors for providing me with this fantastic opportunity to pursue this research and for their suggestions, knowledge, and lessons on research ethics and detailed-oriented work. This has been really beneficial because I have acquired new skills and learned how to conduct quality scientific research.

I am also grateful to my research committee members, Prof. M. R. Shenoy, Prof. Sunil Kumar, and Prof. Amol Choudhary, for their constructive feedback and fruitful suggestions in the SRC review meetings that have enriched the quality of this research work.

I want to acknowledge CSIR India for the junior and senior research fellowship/assistance (09/086(1351)/2018-EMR-I) during my Ph.D and DST India for the project grant (DST/ICPS/QuST/Theme-1/2019/Q-62). Without their support, this work would not have been possible. I also wish to acknowledge IIT Delhi for providing me with the RSTA grant to travel and attend an international conference in the USA. I would also like to thank the Department of Physics and its non-teaching staff members for their help during my Ph.D.

I wish to extend my deepest thanks to Dr. Vaishnavi Rajagopal for the invaluable lessons on scientific writing and effective technical presentation. I have learned a lot from you. Thank you for being such a good teacher and motivator.

An exceptional thanks to all (former and present) my colleagues and friends of Quantum Photonics Lab, Dr. Ramesh Kumar, Dr. Vineet Kumar Shukla, Dr. Shivani Sharma, Omshankar (soon-to-be Dr. Omshankar), Dr. Rajni Bala, Akanksha Angural, Bharti, Vijay, Nilesh Tiwari, and S K Wasim Ahamed with whom I had

a lot of interaction. All of you have been fantastic individuals, and your discussions, feedback, and companionship made this journey enjoyable and memorable. I wish to extend my appreciation to Dr. Arun Kumar, Dr. Mitali Sisodia, Ashish Samantaray, Samyak Gothi, Nikunj, Khushboo, Abhishek, Gourav, and Shibam for memorable interactions and research discussions. I thank Dr. Ramesh Kumar and Ashish Samantaray for being excellent collaborators. A special thanks to Omshankar for being a good friend and helping me in the early experiments. I appreciate your support and encouragement, and thanks for providing a vibrant and stimulating research environment.

I thank my friends, Dr. Vipul Upadhyay, Vishal Patel, Manjeet, Ankit, Chanderkant, and Krishankant, for being a part of my life. Your constant support and company have been precious in this journey.

Last but not least, I owe my deepest appreciation to my parents, siblings, wife, and in-laws for their unwavering love, patience, encouragement, and emotional support. To my wife, thank you for understanding and believing in me even during the most challenging times. I am fortunate to have you in my life.

Once again, I thank you all for being a part of this wonderful journey.

Abstract

This thesis primarily focuses on the characterization of fully fiber-integrated quantum light sources at telecommunication wavelength for diverse quantum applications, such as quantum key distribution (QKD), quantum communication, cryptography, and information processing over existing fiber-optic networks. We exploit a periodically poled lithium niobate (PPLN) waveguide in a spontaneous parametric down-conversion (SPDC) process to generate different types of photonic quantum states in the telecom band. We present an extensive analytical derivation of the Schmidt decomposition for spectral purity estimation of the SPDC biphoton state and theoretically show the generation of spectrally pure (purity $\sim$ 90%, without filtering) telecom photons in a chip-scale lithium niobate on insulator (LNOI) ridge waveguide. A comparison between the analytical and numerical solutions of Schmidt decomposition is carried out through the detailed analysis of the spectral purity in the LNOI waveguide, and the effect of scattering losses on purity is studied to find the robustness of the waveguide. We perform an experimental and theoretical thorough characterization of a fiber-pigtailed Zn-indiffused MgO-doped PPLN (MgO:PPLN) ridge waveguide via second harmonic generation (SHG). We further show the generation of spectrally correlated photon pairs over a broad telecom region, which spans the S-, C-, and L-bands, via completely guided-wave SPDC in the same Zn-indiffused MgO:PPLN waveguide. The photon emission spectrum has a full-width half-maximum bandwidth of $\sim$ 46 nm and a high coincidence-to-accidental ratio (CAR). Next, we demonstrate a fully fiber-coupled source of broadband polarization entanglement over the telecom C- and L-bands in a Zn-indiffused MgO:PPLN waveguide. The high brightness (2×10^8 pairs/s/mW/nm) and active-stabilization free source generate broadband entanglement with $>$ 89% fidelity. The entangled state shows the violation of CHSH inequality by 29 standard deviations (S = 2.49 $\pm$ 0.017), and this source can be directly used in wavelength-division-multiplexed QKD. Finally, we characterize and demonstrate a fiber-integrated multi-user source for long-distance metropolitan-scale ($\sim$ 100 km) QKD and communication. The proposed source can generate both $|\Phi^+\rangle$ (fidelity $>$ 89%) and $|\Phi^-\rangle$ (fidelity $>$ 90%) Bell state in 14 International Telecommunication Union (ITU) channel pairs simultaneously, which allows 14 different user pairs to utilize the source for simultaneous quantum communication and secure key distribution. The source's potential for

long-distance entanglement transmission to remote users is tested by transmitting the entangled photons up to a distance of 100 km, and the effect of polarization mode dispersion (PMD) on entanglement distribution is studied in detail. The proposed source can be used over the existing fiber optic network for multi-user QKD and to develop a complete quantum communication network.

This thesis proposes the on-chip and fiber-integrated PPLN waveguide-based quantum sources of telecom photons, which have wide applications in fiber-based quantum communication, QKD, sensing, and metrology. The proposed fiber-integrated sources are efficient and stable and do not require high optical alignment. These can be easily deployed in the existing fiber infrastructure to scale up the quantum communication network.

सार

यह थीसिस मुख्य रूप से पूरी तरह से दूरसंचार तरंग दैर्ध्य पर फाइबर-एकीकृत क्वांटम प्रकाश स्रोत के लक्षण वर्णन पर केंद्रित है जो मौजूदा फाइबर-ऑप्टिक नेटवर्क पर विविध क्वांटम अनुप्रयोगों जैसे क्वांटम कुंजी वितरण (क्यूकेडी), क्वांटम संचार, क्रिप्टोग्राफी, और सूचना प्रसंस्करण के लिए उपयोग किये जा सकते है। हम विभिन्न प्रकार के फोटोनिक क्वांटम अवस्था को दूरसंचार बैंड में उत्पन करने के लिए एक पेरिऑडिकालय पोलेंड लिथियम नाइओबेट (पीपीएलएन) वेवगाइड का स्वत:स्फूर्त पैरामीट्रिक डाउन-रूपांतरण (एसपीडीसी) प्रक्रिया में प्रयोग करते है। हम एसपीडीसी बाइफोटोन स्थिति की वर्णक्रमीय शुद्धता आकलन के लिए श्मिट डेकोम्पोसिशन की एक व्यापक विश्लेषणात्मक व्युत्पत्ति प्रस्तुत करते है और सैद्धांतिक रूप से वर्णक्रमीय रूप से शुद्ध (शुद्धता $\sim 90\%$, बिना फ़िल्टर किए) टेलीकॉम फोटॉन का एक चिप-स्केल लिथियम नाइओबेट ऑन इंसुलेटर (एलएनओआई) रिज वेवगाइड पर उत्पादन दिखाते है। श्मिट अपघटन के विश्लेषणात्मक और संख्यात्मक समाधान के बीच तुलना एलएनओआई वेवगाइड में वर्णक्रमीय शुद्धता के विस्तृत विश्लेषण के माध्यम से किया जाता है, और वेवगाइड की मजबूती का पता लगाने के लिए शुद्धता पर पड़ने वाले प्रकीर्णन नुकसान के प्रभाव का अध्ययन किया जाता है। हम दूसरी हार्मोनिक उत्पादन (एसएचजी) के माध्यम से एक फ़ाइबर-पिगटेल्ड जिंक-इंडिफ़्यूज़्ड मैग्नेसियम-डोप्ड पीपीएलएन (ऍमजीऔ:पीपीएलएन) रिज वेवगाइड का गहनता से प्रायोगिक और सैद्धांतिक लक्षण वर्णन का प्रदर्शन करते है। हम आगे उसी वेवगाइड में पूरी तरह से निर्देशित तरंग एसपीडीसी के माध्यम से एक व्यापक दूरसंचार क्षेत्र में वर्णक्रमीय रूप से सहसंबद्ध फोटॉन जोड़े के उत्पादन को दिखाते हैं, जो एस- सी- और एल-बैंड को कवर करता है। फोटॉन उत्सर्जन स्पेक्ट्रम की आधी अधिकतम पूर्ण-चौड़ाई ~ 46 एनएम है और एक उच्च संयोग-से-आकस्मिक अनुपात (कार) है। इसके बाद, हम जिंक इंडिफ़्यूज़्ड ऍमजीऔ:पीपीएलएन वेवगाइड में टेलीकॉम सी- और एल-बैंड के ऊपर पूरी तरह से फाइबर-युग्मित एक ब्रॉडबैंड ध्रुवीकरण उलझाव के स्रोत को प्रदर्शित करते हैं। उच्च चमक (2×10^8 जोड़े/सेकंड/मिली वाट/नैनो मीटर) और सक्रिय-स्थिरीकरण मुफ़्त स्रोत $> 89\%$ फिडेलिटी के साथ ब्रॉडबैंड उलझाव उत्पन्न करता है। उलझी हुइ अवस्था 29 मानक विचलन (एस = 2.49 ± 0.017) द्वारा सीएचएसएच असमानता का उल्लंघन दर्शाती है, और इस स्रोत का उपयोग सीधे तरंग दैर्ध्य-विभाजन-मल्टीप्लेक्स क्यूकेडी में किया जा सकता है। अंत में, हम लंबी दूरी के संचार और महानगरीय पैमाने (~ 100 किमी) क्यूकेडी के लिए फाइबर-एकीकृत बहु-उपयोगकर्ता स्रोत को वर्णित और प्रदर्शित करते हैं। प्रस्तावित स्रोत 14 अंतर्राष्ट्रीय दूरसंचार संघ (आईटीयू) चैनल जोड़े में एक साथ दोनों $|\Phi^+\rangle$ (फिडेलिटी $> 89\%$) और $|\Phi^-\rangle$ (फिडेलिटी $> 90\%$) बेल स्थिति उत्पन्न कर सकता है, जो क्वांटम संचार और सुरक्षित कुंजी वितरण के लिए 14 अलग-अलग उपयोगकर्ता जोड़े को एक साथ स्रोत का उपयोग करने की अनुमति देती है। दूरस्थ उपयोगकर्ताओं के लिए लंबी दूरी की उलझाव संचरण की स्रोत की क्षमता का परीक्षण 100 किमी की दूरी तक उलझे हुए फोटॉन का संचारण द्वारा किया जाता है, और ध्रुवीकरण मोड फैलाव (पीएमडी) के उलझाव वितरण पर प्रभाव का विस्तार से अध्ययन किया गया है। प्रस्तावित स्रोत का उपयोग मौजूदा फाइबर ऑप्टिक नेटवर्क पर बहु-उपयोगकर्ता क्यूकेडी और एक संपूर्ण क्वांटम संचार नेटवर्क विकसित करने के लिए किया जा सकता है।

यह थीसिस टेलीकॉम फोटॉनों के ऑन-चिप और फाइबर-एकीकृत पीपीएलएन वेवगाइड-आधारित क्वांटम स्रोतों का प्रस्ताव करती है, जिनका फाइबर-आधारित क्वांटम संचार, क्यूकेडी, सेंसिंग और मेट्रोलॉजी में व्यापक अनुप्रयोग है। प्रस्तावित फाइबर-एकीकृत स्रोत कुशल और स्थिर हैं और उन्हें उच्च ऑप्टिकल संरेखण की आवश्यकता नहीं है। इन्हे क्वांटम संचार नेटवर्क.की मात्रा को बढ़ाने के लिए मौजूदा फाइबर बुनियादी ढांचे में आसानी से तैनात किया जा सकता है।

Contents

List of Figures

List of Tables

List of Acronyms

AWG	**A**rrayed **W**aveguide **G**rating
APD	**A**valanche **P**hoto**D**etector
BBO	**B**eta **B**arium **B**orate
CAR	**C**oincidence to **A**ccidental **R**atio
CHSH	**C**lauser **H**orne **S**himony **H**olt
CW	**C**ontinuous **W**ave
DGD	**D**ifferential **G**roup **D**elay
DWDM	**D**ense **W**avelength **D**ivision **M**ultiplexed
FWHM	**F**ull **W**idth **H**alf **M**aximum
FPBS	**F**iber **P**olarization **B**eam **S**plitter
HWP	**H**alf **W**ave **P**late
ITU	**I**nternational **T**elecommunication **U**nion
JSA	**J**oint **S**pectral **A**mplitude
JSI	**J**oint **S**pectral **I**ntensity
KTP	**P**otassium **T**itanyl **P**hosphate
LNOI	**L**ithium **N**iobate **O**n **I**nsulator
LPF	**L**ong **P**ass **F**ilter
MgO:PPLN	**MgO** doped **P**eriodically **P**oled **L**ithium **N**iobate
MgO:LN	**MgO** doped **L**ithium **N**iobate
PPKTP	**P**eriodically **P**oled **P**otassium **T**itanyl **P**hosphate
PPLN	**P**eriodically **P**oled **L**ithium **N**iobate
PMD	**P**olarization **M**ode **D**ispersion
PBS	**P**olarization **B**eam **S**plitter
PEF	**P**ump **E**nvelope **F**unction
PMF	**P**hase **M**atching **F**unction
PM	**P**olarization **M**aintaining

PC	**P**olarization **C**ontroller
QKD	**Q**uantum **K**ey **D**istribution
QPM	**Q**uasi **P**hase **M**atching
QWP	**Q**uarter **W**ave **P**late
QST	**Q**uantum **S**tate **T**omography
QBER	**Q**uantum **B**it **E**rror **R**ate
SHG	**S**econd **H**armonic **G**eneration
SPDC	**S**pontaneous **P**arametric **D**own **C**onversion
SFWM	**S**pontaneous **F**our **W**ave **M**ixing
SM	**S**ingle **M**ode
SPAD	**S**ingle **P**hoton **A**valanche **P**hoto**D**etector
TM	**T**ransverse **M**agnetic
VOA	**V**ariable **O**ptical **A**ttenuator
WDM	**W**avelength **D**ivision **M**ultiplexer
WDM-QKD	**W**avelength **D**ivision **M**ultiplexing based **Q**uantum **K**ey **D**istribution

List of Symbols

c	Speed of light in vacuum
ω	Angular frequency
λ	Wavelength
ϵ_o	Permittivity of free space
k	Propagation vector
n_{eff}	Effective refractive index
$\chi^{(2)}$	Second-order nonlinear susceptibility
Λ	Poling period
P	Polarization
E	Electric field
$\Delta\lambda_p$	Pump bandwidth
Δk	Phase-mismatch
λ_n	Schmidt coefficient
K	Schmidt number
α	Scattering loss
L	Waveguide length
$\hat{a}^\dagger$	Creation operator
H	Horizontal polarization
V	Vertical polarization
D	Diagonal polarization
A	Anti-diagonal polarization
C	Concurrence
F	Fidelity

Chapter 1

Introduction

1.1 Quantum photonic telecom source for long-distance quantum communication

In the last two decades, quantum entanglement has transformed the fields of optics [1, 2], communication [3, 4], measurement [5], imaging [6, 7], sensing [8], and computation [9]. Unique attributes of quantum entanglement, such as the functional inability to copy the exact quantum state (known as the no-cloning theorem) and the ability to retain correlations over large distances for long periods, help in the transmission of information in fundamentally secure way, faster computation, and precision improved metrology [5, 10, 11]. Entanglement is a key aspect of quantum communication where a highly secure cryptographic key can be generated by exploiting the fundamental laws of quantum mechanics that are impervious to eavesdropping. Quantum communication, information, and computation at its core uses quantum bits or qubits, which can exist in multiple states simultaneously by leveraging the property of superposition and are impossible to clone, thus offering significant advantages over classical bits [1]. There are several means by which we

can generate qubits such as trapped ions [12], quantum dots [13], photons [14, 15], and superconducting circuits [16, 17]. Each qubit technology has its own advantages and challenges. For example, trapped ion qubits are difficult to scale and comparatively slow in operation [18], quantum dot qubits require precise manipulation, and superconducting qubits require a cryogenic environment [19, 17], and they also decohere quickly. The photonic qubits offer several advantages over others due to their long coherence time, room temperature operation, ease of transmission, scalability, and versatility [4, 20]. These mentioned key benefits make them promising candidates for various applications such as quantum computing, communication, and information processing [20, 10, 21].

Photon offers various degrees of freedom such as energy-time [22, 23], polarization [4, 24], spatial mode [25], orbital angular momentum [26], time-bin [23, 27], and path-polarization [28] to generate a wide variety of entangled states. Among these, polarization-entangled states are advantageous for quantum communication and information processing due to the ease of comprehensive manipulation via well-developed standard optics. Some of the prominent technologies for this polarization-entangled photonic state generation are spontaneous parametric down-conversion (SPDC) [29], spontaneous four-wave mixing (SFWM) [30], integrated photonic chips [31], quantum dots [32], and atomic ensembles [33]. Out of these, SPDC is the most effective and widely used technique for photonic qubit generation owing to high photon flux, mature fabrication, well-developed dispersion compensation technique, and easy pump rejection (since the pump and down-converted photons are well separated in frequency).

SPDC process is frequently used to generate visible and telecom photons for free space and fiber-based quantum communication applications. Free space quantum communication uses low-loss visible photons and highly efficient compact avalanche

photodetectors to transmit the information to remote users. The main challenges in free space quantum communication come from atmospheric interference (such as scattering, absorption, and turbulence) [34], line-of-sight requirement, optical alignment, and stability. These factors limit its scalability for ground-to-ground communication. On the other hand, fiber-based quantum communication (telecom photonic entanglement) reaps from the existing fiber network infrastructure to transmit secure information to remote users.

In the last two decades, telecom-photon-pair generation through SPDC has been realized in several materials, including beta barium borate (BBO) [35], periodically poled potassium titanyl phosphate (PPKTP) [36], and periodically poled lithium niobate (PPLN) [4]. Among these, PPLN-based sources provide the highest spectral brightness (high photon flux $\sim 10^6$ pairs/s/mw/GHz) and large bandwidth ($\sim$ 40 nm) [37], which is essential for long-distance quantum key distribution (QKD) and communication applications. The SPDC photons often have high spectral correlation [38, 39], which is useful for multi-user QKD and communication applications where no crosstalk is desired between the channels/users. However, specific applications such as linear optical quantum computing [40] and quantum interference-based photonic processors [41] require spectrally uncorrelated (pure) photons. Now, such sources can also be achieved through the SPDC process by tailoring the phase-matching function of the material via geometry-induced dispersion [42]. This thesis involves the theoretical/experimental generation and characterization of spectrally pure, spectrally correlated, and polarized entangled photons at telecom wavelengths in a PPLN ridge waveguide.

The photonic entanglement-based cryptography holds the potential to generate a secure key over a longer distance than decoy-based quantum cryptography [43]. For example, time-bin entanglement has been demonstrated over 200 km [44] and

300 km [45] distance via fiber spools, and polarization entanglement has been distributed over 192 km of deployed optical fiber [4]. This reflects the potential of photonic entanglement for long-distance QKD. Polarization-entanglement is often preferred over time-bin entanglement for higher key generation, but there is one major concern, which is its susceptibility to environmental influences like stress, movement, and temperature change along the fiber link [4]. These factors introduce the polarization-mode-dispersion (PMD) in the transmission channel, which degrades the entanglement quality and limits the range of transmission. Recently some small area quantum communication networks have also been demonstrated utilizing an SPDC source where each user shares an entangled photon with the other [46, 47, 48, 49].

Despite these advances in fiber-based quantum communication, the scalability of the quantum communication network continues to be inadequate due to the difficulty of source deployment, lack of realistic scalable quantum repeaters [50, 51], and not exploiting the broadband entanglement to its full potential [51]. The scalability of a city-wide or local-area quantum communication network requires widespread connectivity, trusted-node-free operation, and an efficient and easily deployable source that can be located at the center of the network. The source acts as a service provider and will generate highly entangled photon pairs and distribute them to remote users through the fiber network. In this regard, a single broadband source that generates entangled photons can serve this purpose with a suitable wavelength-division-multiplexer (WDM) or arrayed-waveguide-grating (AWG), which demultiplexes the spectrum or distributes the entanglement in multiple wavelength channels. Such optical-alignment-free, efficient, stable, and easily deployable sources are not fully explored. In this work, we aim to explore such fully fiber-integrated sources of entangled photons for long-distance QKD and communication over a city-wide fiber

network.

In this thesis, we theoretically study the generation of spectrally pure photons at telecom wavelength through lithium niobate on insulator (LNOI) waveguide and compare the analytical and numerical methods of spectral purity estimation. We experimentally demonstrate the generation of spectrally correlated and polarization-entangled telecom photons through a fiber-pigtailed PPLN waveguide in a completely fiber-integrated setup. We also characterize a multi-user source for long-distance (metropolitan-scale) QKD and study the effect of PMD on polarization entanglement distribution.

To generate these different types of telecom photons, we utilize the SPDC process and also make use of the second harmonic generation (SHG) process to characterize (to find the parameters such as phase-matching temperature, efficiency, etc) the source (especially in the experimental work). Therefore, providing a brief background on these processes would be appropriate here. Also, the theoretical underpinnings of SHG and SPDC would later be helpful in understanding the two experimental processes in fiber-integrated PPLN waveguides.

1.2 Second harmonic generation (SHG)

In nonlinear optical media, polarization has a nonlinear dependence on the electric field when the amplitude of the applied electric field is of the order of atomic electric field strength $\sim 10^{11}$ V/m. This sufficient high electric field can be obtained through an intense laser beam, and when such an intense beam is passed through a nonlinear optical media, the polarization can be expressed as [52, 53, 54]

$$\vec{P} = \epsilon_o \chi^{(1)} \vec{E} + \epsilon_o \chi^{(2)} \vec{E}\vec{E} + \epsilon_o \chi^{(3)} \vec{E}\vec{E}\vec{E} + ... \tag{1.1}$$

where ϵ_o is the permittivity of free space, $\chi^{(1)}$ is the linear susceptibility, and $\chi^{(2)}$ and $\chi^{(3)}$ are the second and third order nonlinear optical susceptibilities, respectively. In noncentrosymmetric materials, such as BBO, KTP, and $LiNbO_3$, $\chi^{(2)} \neq 0$ and it is responsible for the phenomenon namely sum frequency generation, difference frequency generation, SHG, and SPDC.

SHG is a second-order nonlinear process where two photons of frequency ω combine to generate a photon of frequency 2ω, providing the phase-matching conditions are satisfied (see Fig. 1.1). This is a classical process, and the efficiency can be calculated

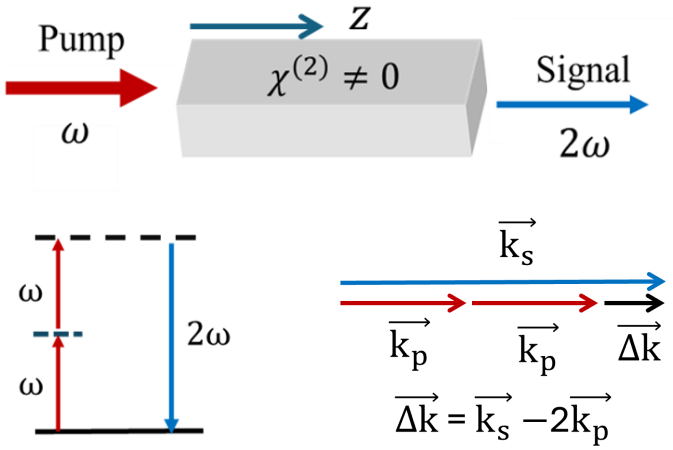

FIGURE 1.1: Schematic of second harmonic generation (SHG) process. A pump photon at frequency ω interacts with the $\chi^{(2)}$ material to generate a signal at frequency at 2ω by satisfying the energy and momentum conservation conditions.

from the coupled differential equations [52, 54, 55]

$$\frac{dE_2}{dz} = \frac{i\omega d}{cn_2} E_1^2 e^{-i\Delta kz} \tag{1.2}$$

$$\frac{dE_1}{dz} = \frac{i\omega d}{cn_1} E_2 E_1^* e^{i\Delta kz} \tag{1.3}$$

where d is the nonlinear coefficient ($d = \frac{1}{2}\chi^{(2)}$), and c is the speed of light; E_1, E_2 are the field amplitudes, and n_1, n_2 are the refractive indices at frequency ω (pump) and 2ω (signal), respectively. $\Delta k = k_s - 2k_p = \frac{2\omega}{c}(n_2 - n_1)$ is the the phase-matching

condition or phase-mismatch. The efficiency is given as [52, 53, 54, 55]

$$\eta = \frac{2\mu_o \omega^2 d^2 P_1}{c n_1^2 n_2 A} \frac{sin^2(\Delta k z/2)}{(\Delta k/2)^2} \tag{1.4}$$

where μ_o is the permeability of free space, P_1 is the pump power, and A is the Area. It is clear that if $\Delta k \neq 0$, then SHG efficiency will vary sinusoidally along the waveguide/crystal length (z), and if $\Delta k = 0$, then efficiency will vary quadratically (z^2) with length. In practice, due to dispersion $n_2 \neq n_1$ and thus $\Delta k \neq 0$, it requires some technique to satisfy the phase-matching condition. Quasi-phase-matching (QPM) is one such technique that is usually employed in KTP and $LiNbO_3$ to satisfy the phase-matching condition.

Quasi phase-matching (QPM)

In QPM, the crystal/waveguide is poled with a suitable period (i.e. crystal domains are periodically inverted to result in a periodic sign change in $\chi^{(2)}$ nonlinearity) as shown in Fig. 1.2, which results in a factor of $\frac{2\pi}{\Lambda}$ (where Λ is known as poling period) in phase-mismatch. The periodic poling is performed by placing periodic electrodes (i.e. after a distance interval of Λ) along the waveguide length and then applying a very high voltage pulse of the order of a few kV ($\sim$ 11 kV) or an electric field of the order of $\sim$ 22 kV/mm . This process inverts the sign of nonlinear coefficient d and allows the effective constructive interference of newly generated photons with the previously generated photons, resulting in an increase in the generated photons as the input light propagates through the material. The nonlinear coefficient modifies to $d(z) = d_{eff} sign(cos(\frac{2\pi z}{\Lambda}))$ or simply (after Fourier series expansion) $d(z) = \frac{2d_{eff}}{\pi} e^{\frac{i2\pi z}{\Lambda}}$ [52].

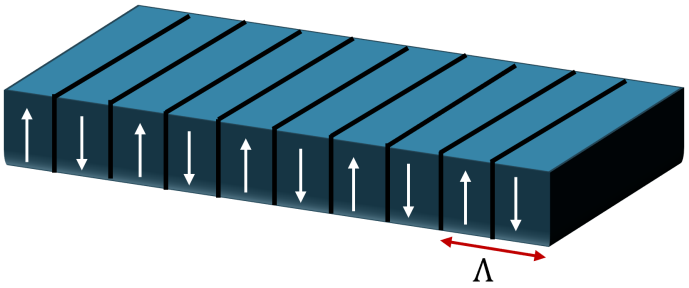

FIGURE 1.2: Schematic of QPM (periodic poling) in a $\chi^{(2)}$ nonlinear material.

Thus, with QPM, the phase-mismatch gets modified to

$$\Delta k = k_s - 2k_p - \frac{2\pi}{\Lambda} \tag{1.5}$$

where a suitable Λ helps in phase-matching i.e. in making $\Delta k = 0$. The value of Λ will depend on the type of process and the wavelength that we want to phase-match; for example, if we want to do the SHG of, say, 1550 nm light and 800 nm light in PPLN waveguide with the type-II process, then we need two different poling periods to satisfy the phase-matching conditions. Equation (1.4) can also be written as

$$\eta = \frac{2\mu_o \omega^2 d^2 P_1 z^2}{c n_1^2 n_2 A} sinc^2(\Delta k z/2) \tag{1.6}$$

which indicates that under perfect phase-matching, the second harmonic power will have quadratic dependence on input pump power, and the efficiency will grow quadratically with waveguide length. This equation is valid only for low conversion efficiency assuming E_1 is constant i.e. no depletion of the pump beam [52, 53, 54].

1.3 Spontaneous parametric down-conversion (SPDC)

Spontaneous parametric down-conversion (SPDC) is a quantum mechanical process where a pump photon of frequency ω_p annihilates to generate two photons of new frequency ω_s and ω_i (known as *signal* and *idler*) in a $\chi^{(2)}$ nonlinear media (see Fig. 1.3) [1, 56, 57]. Vacuum fluctuation seeds this process, and the frequencies of the down-converted signal and idler photons are constrained by the energy and momentum conservation conditions given as [1]

$$\omega_p = \omega_s + \omega_i \tag{1.7}$$

$$\vec{k}_p = \vec{k}_s + \vec{k}_i \tag{1.8}$$

where $\omega_{p,s,i}$ are the frequencies and $\vec{k}_{p,s,i}$ are the propagation vectors of pump, signal, and idler, respectively. In a waveguide, the photon emission is colinear i.e. all the propagation vectors are aligned in the same direction, so the momentum conservation can be written as

$$k_p = k_s + k_i \tag{1.9}$$

where $k_{p,s,i}$ can be computed as $k_{p,s,i} = \frac{2\pi}{\lambda_{p,s,i}} \times [n_{eff}]_{p,s,i}$ where λ is the wavelength and n_{eff} is the effective refractive index of the corresponding photon. As discussed above, momentum conservation (phase-matching) is not satisfied due to dispersion. i.e. $\Delta k = k_p - k_s - k_i \neq 0$. This is again satisfied through QPM technique [52, 53], and thus, Δk can be given as

$$\Delta k = k_p - k_s - k_i - \frac{2\pi}{\Lambda} \tag{1.10}$$

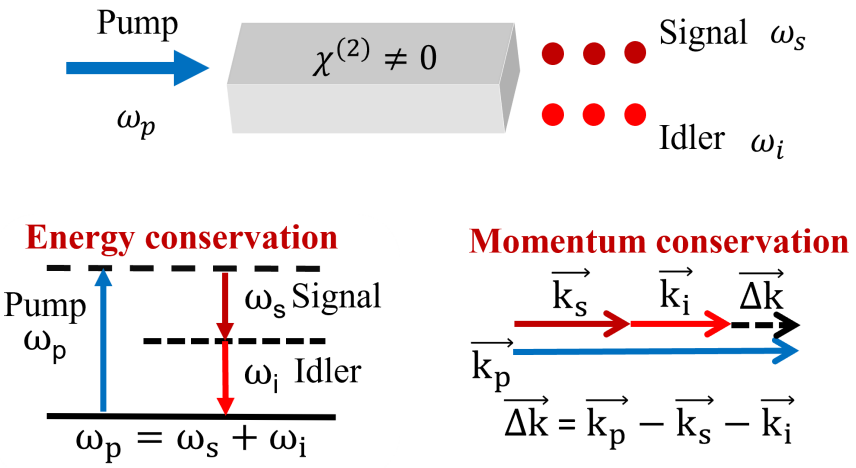

FIGURE 1.3: Schematic of spontaneous parametric down-conversion (SPDC) process in a $\chi^{(2)}$ waveguide. A pump photon at frequency ω_p interacts with the $\chi^{(2)}$ material to generate two photons at frequency ω_s (signal) and ω_i (idler) by satisfying phase-matching conditions.

where Λ is the poling period of the waveguide.

Next, we briefly discuss the quantum-mechanical picture of SPDC by considering the Hamiltonian of nonlinear interaction and vacuum state. The Hamiltonian governing SPDC inside a nonlinear interaction volume can be expressed as [56, 58]

$$\hat{H} = \int_v \hat{P}(r,t)E(r,t)d^3r \tag{1.11}$$

considering the nonlinear dependence of polarization on the electric field, it can be approximated as

$$\hat{H} \propto \chi^{(2)} E_p(r,t)\hat{E}_s(r,t)\hat{E}_i(r,t) \tag{1.12}$$

if we assume the pump to be a classical plane wave which remains undepleted and quantize the electric field of output photons (i.e. $\hat{E}(r,t) \propto [\hat{a}e^{i(kr-\omega t)} - \hat{a}^\dagger e^{-i(kr-\omega t)}]$), then Eq. 1.12 modifies to [56, 58, 57]

$$\hat{H} \propto i\hbar G\hat{a}_s^\dagger \hat{a}_i^\dagger + H.c \tag{1.13}$$

where $G \propto \chi^{(2)}\sqrt{P_p}$, P_p is the pump power, $\hat{a}_s^\dagger$ and $\hat{a}_i^\dagger$ are the creation operators corresponding to signal and idler photons and $H.c$ is the Hermitian conjugate. The vacuum state evolves with time, and the output state at the waveguide facet is given as

$$|\Psi(t)\rangle = e^{\frac{-i}{\hbar}\int_0^t H dt} |\Psi(0)\rangle \tag{1.14}$$

considering the Hamiltonian of Eq. 1.13 it can also be written as

$$|\Psi(t)\rangle = e^{Gt\hat{a}_s^\dagger \hat{a}_i^\dagger} |0_s\rangle |0_i\rangle \tag{1.15}$$

Thus, the above expression can be approximated as [1, 56]

$$|\Psi(t)\rangle = |0_s\rangle |0_i\rangle + Gt |1_s\rangle |1_i\rangle + (Gt)^2 |2_s\rangle |2_i\rangle + ... \tag{1.16}$$

In the weak pump regime, the above series can be truncated after the first two terms i.e., $|\Psi(t)\rangle = |0_s\rangle |0_i\rangle + Gt |1_s\rangle |1_i\rangle$, where the non-trivial term is $|1_s\rangle |1_i\rangle$, which shows the generation of a biphoton (two-photon) state. The probability of the biphoton generation strongly depends on waveguide length, pump power, and $\chi^{(2)}$ susceptibility/nonlinear strength. It also depends on the spatial mode overlap (A_{lmn}) of the pump, signal, and idler photon, where a higher mode overlap increases the probability of biphoton generation [59].

$$A_{lmn} = \int E_p^{(l)}(r) E_s^{*(m)}(r) E_i^{*(n)}(r) d^2r \tag{1.17}$$

where l, m, n represents the l^{th}, m^{th}, and n^{th} mode field of pump, signal, and idler photons, respectively. Depending on the polarization of the pump, signal, and idler photon, the SPDC process is categorized into three types:

1. Type-0 (pump, signal, and idler have identical polarization): $H_p \rightarrow H_s + H_i$ or

$V_p \rightarrow V_s + V_i$.

2. Type-I (signal and idler have identical polarization but orthogonal to pump polarization): $H_p \rightarrow V_s + V_i$ or $V_p \rightarrow H_s + H_i$.

3. Type-II (signal and idler have orthogonal polarization): $H_p \rightarrow V_s + H_i$ or $V_p \rightarrow V_s + H_i$.

In this work, we will deal with type-0 and type-II SPDC processes for telecom photon pair generation through a PPLN ridge waveguide.

1.4 Measures of the SPDC source quality

1.4.1 Spectral brightness

The quality of an SPDC source is characterized by spectral brightness, which is a measure of photon flux. A high photon flux/spectral brightness indicates high quality, which is desired for long-distance QKD and communication applications. Spectral brightness is generally defined as the photon pair generated per unit input pump power per unit photon emission bandwidth, and it is reported in the unit of pairs/s/mW/nm or pairs/s/mW/GHz. The number of photon pairs can be calculated from $N_{pair} = \frac{N_s N_i}{N_c}$, where N_s, N_i, and N_c are the signal counts, idler counts, and coincidence counts, respectively [60, 61]. If we know the signal and idler counts and the corresponding efficiencies of two paths, then N_{pair} can also be estimated via the relation $N_s = \eta_s N_{pair}$ and/or $N_i = \eta_i N_{pair}$. Here in this thesis, we take the latter approach to calculate the spectral brightness because, in the first approach, the effect of the coincidence detection window is not incorporated. The number of coincidence counts/s can change for fixed single counts by changing the coincidence detection time window. We take the minimum of the detected signal

and idler counts and consider the efficiencies of all components that are connected between the point of generation and detection in that path to estimate the N_{pair}. The spectral brightness is then calculated by dividing the N_{pair} with pump power (which is used to generate the photons) and the filter bandwidth of that path i.e. $\frac{N_{pair}(\text{pairs/s})}{\text{pump power (mW)}\times\text{spectral bandwidth (nm or GHz)}}$.

1.4.2 Coincidence-to-accidental ratio (CAR)

CAR is another important parameter to measure the quality of an SPDC source, which defines the temporal correlation between the generated signal/idler photons [62] in a biphoton state. It is defined as the ratio of *true coincidences* and *accidental coincidences*, CAR $= C_t/C_a$ [63], where C_t (*true coincidences*) is the peak coincidence rate measured at zero time delay between the two output photons and C_a (*accidental coincidences*) is the background coincidence rate at any finite time delay (larger than the measurement bin-width and/or the coherence time of the biphotons). The peak of the histogram shown in Fig. 1.4 indicates the true coincidence counts (C_t), and the wing shows the accidental counts (C_a).

Accidental coincidences in a quantum source can arise from several factors, such as some background fluorescence/scattering process, multi-photon generation events, detector dark counts, and/or pump photons leaking through the optical components. CAR is an important figure of merit in estimating how many undesired noise photons are being generated along with the desired photons. A high CAR value ensures high quality of the photon-pair source, and it is also a measure of cross-correlation function ($g^{(2)}_{si}(0)$) which is related to CAR via the relation $g^{(2)}_{si}(0) = \text{CAR} + 1$ [64] (note that this is not the conditional self-correlation or heralded $g^{(2)}(0)$). To test the emission of single photons or anti-bunched photons from a quantum source, one

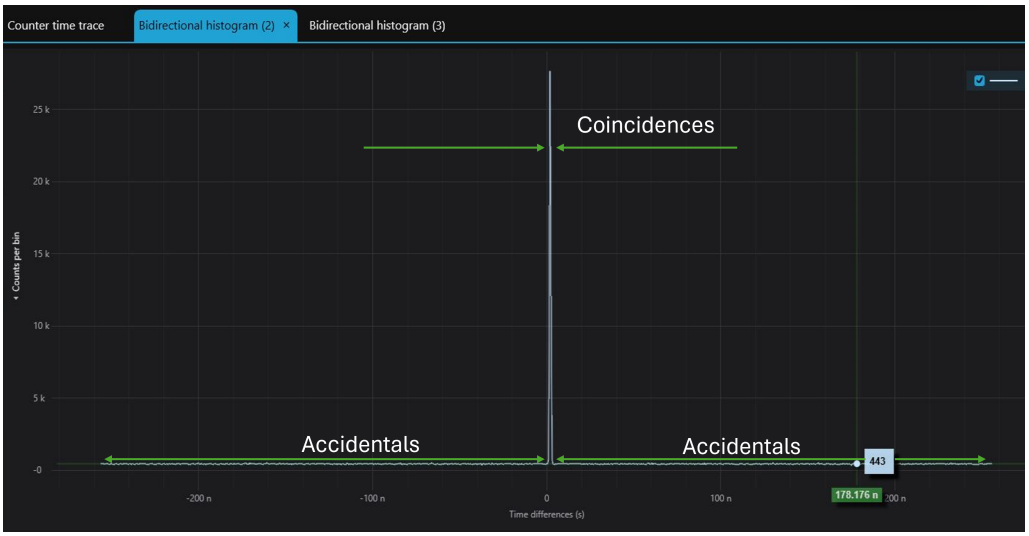

FIGURE 1.4: Histogram showing the true coincidences and accidental counts between the down-converted photons.

has to perform the heralded $g^{(2)}(0)$ measurement and not $g_{si}^{(2)}(0)$ [64, 65] because $g_{si}^{(2)}(0)$ is a measure of photon-pair generation.

1.5 Polarization entanglement

The state of a multi-particle system can be described as an entangled state if its wave function can not be factored into a product of the wave functions of individual particles. EPR or Bell states are two-qubit entangled states that show the non-local nature of quantum mechanics. These states have a wide range of applications in quantum teleportation, cryptography, communication, computing, etc. The Bell states can be generated in a variety of systems, such as photons, electrons, atoms, ions, etc. Here, we are interested in photons and especially in their polarization degree of freedom. The photon in the polarization degree of freedom can be easily manipulated with the help of standard optics to generate a Bell state. These Bell states are categorized into four types depending on the polarization of two particles (say signal and idler).

$$\left|\Phi^{+}\right\rangle = \frac{1}{\sqrt{2}}(|H_s\rangle\,|H_i\rangle + |V_s\rangle\,|V_i\rangle) \tag{1.18}$$

$$\left|\Phi^{-}\right\rangle = \frac{1}{\sqrt{2}}(|H_s\rangle\,|H_i\rangle - |V_s\rangle\,|V_i\rangle) \tag{1.19}$$

$$\left|\Psi^{+}\right\rangle = \frac{1}{\sqrt{2}}(|H_s\rangle\,|V_i\rangle + |V_s\rangle\,|H_i\rangle) \tag{1.20}$$

$$\left|\Psi^{-}\right\rangle = \frac{1}{\sqrt{2}}(|H_s\rangle\,|V_i\rangle - |V_s\rangle\,|H_i\rangle) \tag{1.21}$$

Here $|H_s\rangle$ ($|V_s\rangle$) and $|H_i\rangle$ ($|V_i\rangle$) represent horizontally (vertically) polarized signal and horizontally (vertically) polarized idler photons. In Bell states, a measurement on one photon allows us to predict the result of the measurement on the other photon with 100% certainty. Various parameters can be used to test these non-local correlations of Bell states and to verify the quantum entanglement. In this thesis, we have used four parameters to characterize the generation of a polarization-entangled Bell state through a fiber-integrated telecom source.

1.6 Parameters of entanglement characterization

1.6.1 Two-photon interference

The polarization-entangled photon pairs exhibit non-local correlations, which can be checked by two-photon interference by projecting the photons into different linear polarization states [66]. The probability of finding the entangled photon pair in the projected state $|\theta_s, \theta_i\rangle$ is given by

$$P(\theta_s, \theta_i) = \frac{1}{2}\cos^2(\theta_s \mp \theta_i) \tag{1.22}$$

or

$$P(\theta_s, \theta_i) = \frac{1}{2}\sin^2(\theta_s \pm \theta_i) \tag{1.23}$$

where $\theta_{s,i}$ is the signal and idler arm's polarizer angle, respectively, and Eq. 1.22 stands for Bell state $|\Phi^{\pm}\rangle$ and Eq. 1.23 stands for $|\Psi^{\pm}\rangle$ [67]. In our case, for two-photon interference measurement, the signal photon is projected onto one of the four polarizations i.e. horizontal (H), vertical (V), diagonal (D), or anti-diagonal (A), via a half-wave plate (HWP) and polarization beam splitter (PBS), and the polarization of idler photon is varied by rotating the angle of HWP placed before the PBS in the idler arm (see Fig. 1.5). The coincidence counts between the signal and idler photon are measured during this process, and the state is then identified by the interference fringe pattern (which follows Eq. 1.22 or Eq. 1.23). The visibility of interference fringes can be calculated from the observed coincidence counts via the relation

$$V = \frac{C_{max} - C_{min}}{C_{max} + C_{min}} \tag{1.24}$$

where C_{max} and C_{min} correspond to the maximum and minimum coincidence counts of a considered fringe.

1.6.2 CHSH-Bell's inequality

The violation of CHSH-Bell's inequality is an important parameter to verify the generation of quantum entanglement [68, 14, 69]. The CHSH inequality was proposed by J. Clauser, M. Horne, A. Shimony, and R. Holt [68], which is similar to Bell's inequality [70] but easily applicable in experiments, states that if the local hidden variable theory is correct, then the inequality will be satisfied. However,

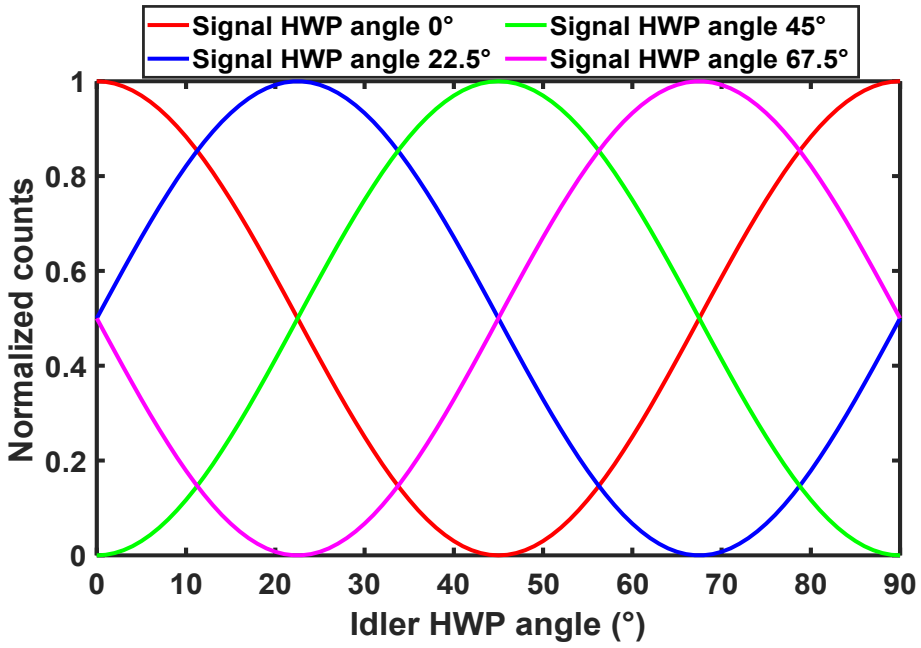

FIGURE 1.5: Two-photon interference pattern of an ideal $|\Phi^+\rangle$ Bell state.

the inequality is routinely violated by the modern experiments of quantum mechanics and quantum optics. The polarization-entangled Bell states violate the CHSH inequality, which is expressed by [14, 69]

$$\mathrm{S} = |(\mathrm{E}(\theta_a, \theta_b) - \mathrm{E}(\theta_a, \theta_b^{'}) + \mathrm{E}(\theta_a^{'}, \theta_b) + \mathrm{E}(\theta_a^{'}, \theta_b^{'})| \leq 2 \tag{1.25}$$

where E is the correlation coefficient, $\mathrm{E}(\theta_a, \theta_b) = \frac{\mathrm{C}(\theta_a,\theta_b)+\mathrm{C}(\theta_a^{\perp},\theta_b^{\perp})-\mathrm{C}(\theta_a^{\perp},\theta_b)-\mathrm{C}(\theta_a,\theta_b^{\perp})}{\mathrm{C}(\theta_a,\theta_b)+\mathrm{C}(\theta_a^{\perp},\theta_b^{\perp})+\mathrm{C}(\theta_a^{\perp},\theta_b)+\mathrm{C}(\theta_a,\theta_b^{\perp})}$, $\mathrm{C}(\theta_a,\theta_b)$ is the coincidence counts when signal arm polarizer is set at an angle θ_a and idler arm polarizer is set at an angle θ_b, and $\theta_{a,b}^{\perp} = \theta_{a,b} + 90°$. The CHSH-Bell's inequality is violated for angles $\theta_a = 0°$, $\theta_a^{'} = 45°$, $\theta_b = 22.5°$, and $\theta_b^{'} = 67.5°$ [14, 67].

However, if we use a half-wave plate (HWP) and a polarization beam splitter (PBS) for Bell state analysis (to project the photon in a particular polarization state), the correlation coefficient $\mathrm{E}(\theta_a, \theta_b)$ can be calculated from

$$\mathrm{E}(\theta_a, \theta_b) = \frac{\mathrm{C}(\theta_a, \theta_b) + \mathrm{C}(\tilde{\theta}_a, \tilde{\theta}_b) - \mathrm{C}(\tilde{\theta}_a, \theta_b) - \mathrm{C}(\theta_a, \tilde{\theta}_b)}{\mathrm{C}(\theta_a, \theta_b) + \mathrm{C}(\tilde{\theta}_a, \tilde{\theta}_b) + \mathrm{C}(\tilde{\theta}_a, \theta_b) + \mathrm{C}(\theta_a, \tilde{\theta}_b)} \tag{1.26}$$

where C(θ_a,θ_b) denotes the coincidence counts corresponding to the case when the signal-arm HWP is at an angle θ_a and the idler-arm HWP is at an angle θ_b, and $\tilde{\theta}_{a,b} = \theta_{a,b} + \frac{\pi}{4}$. The Bell state ($|\Phi^{\pm}\rangle$ or $|\Psi^{\pm}\rangle$) violates Eq. (1.25) at the HWP angle $\theta_a = 0°$, $\theta_a^{'} = 22.5°$, $\theta_b = 11.25°$, and $\theta_b^{'} = 33.75°$. The maximum violation is observed for an ideal Bell state, which has S value = $2\sqrt{2}$. The violation of CHSH-Bell's inequality can be estimated in terms of standard deviation by [71]

$$\text{violation (in terms of standard deviation)} = \frac{\text{S} - \text{B}}{\sigma} \tag{1.27}$$

where S is the experimentally observed S-parameter value, B is the classical limit of the S-parameter (i.e., S = 2), and σ is the standard deviation in the experimentally observed S-parameter.

1.6.3 Quantum state tomography

Quantum state tomography (QST) characterizes the complete quantum state of a system through a series of measurements on identical copies of the same state, where each measurement illuminates a new dimension of the unknown state. In order to find the generated state, at least 16 measurements are performed by projecting the signal and idler photons in different polarization bases and measuring a coincidence event between the two photons [72, 73]. The density matrix is then reconstructed, and its overlap with the ideal Bell state is checked through a parameter known as fidelity (F), which is defined as [72, 74]

$$\text{F} = (\text{trace}\{\sqrt{\sqrt{\sigma}\rho\sqrt{\sigma}}\})^2 \tag{1.28}$$

where σ is the density matrix of the desired ideal Bell state, and ρ is the density matrix of the experimentally observed state. A fidelity value of 0.7 is considered the

classical threshold i.e. F > 0.7 indicates the generation of an entangled quantum state [4]. In this thesis, to find the fidelity of the generated Bell state, we perform the

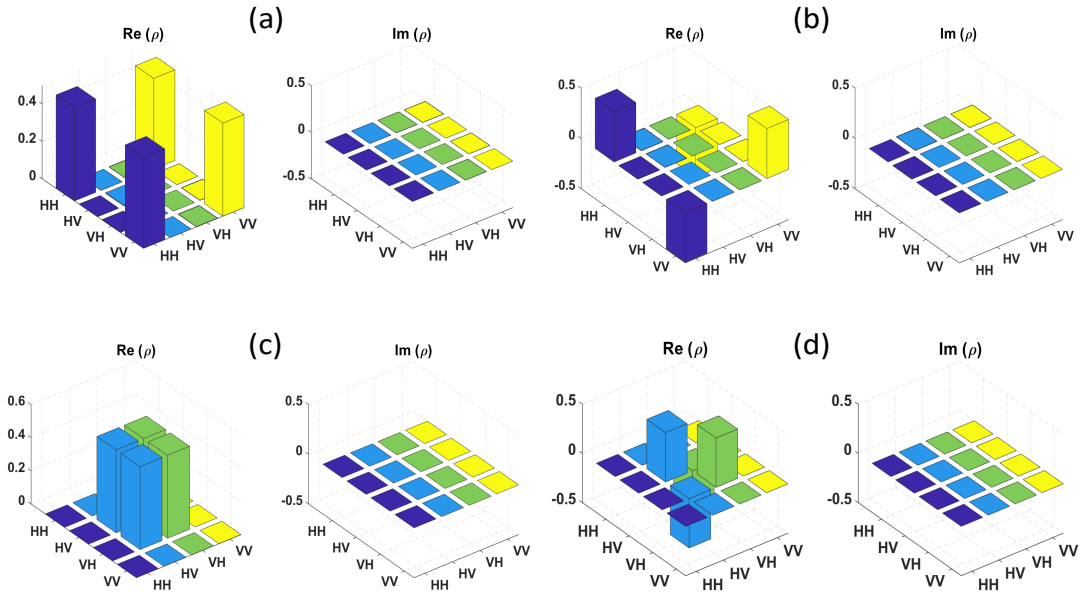

FIGURE 1.6: Density matrix of an ideal Bell state (a) $|\Phi^+\rangle$ (b) $|\Phi^-\rangle$ (c) $|\Psi^+\rangle$ (d) $|\Psi^-\rangle$. Various colors in the density matrix are intended for presentation purposes only and do not reflect any information.

QST measurement by projecting signal and idler photon in 16 different combinations of polarizations (see TABLE 1.1) via a combination of a quarter-wave plate, a half-wave plate, and polarization beam splitter [73]. Figures 1.6 (a), (b), (c), and (d) represent the density matrices of the ideal $|\Phi^+\rangle$, $|\Phi^-\rangle$, $|\Psi^+\rangle$, and $|\Psi^-\rangle$, Bell states respectively.

1.6.4 Concurrence

In a two-qubit state, the entanglement can also be certified by the parameter known as concurrence (C), and it can be calculated from the reconstructed density matrix of the QST measurement. Concurrence is defined as [75]

$$C(\rho) = \max\{0, \sqrt{\lambda_1} - \sqrt{\lambda_2} - \sqrt{\lambda_3} - \sqrt{\lambda_4}\} \tag{1.29}$$

TABLE 1.1: Quarter-wave plate (QWP) and half-wave plate (HWP) angles in the signal and idler path for QST measurement [73].

	Signal path		Idler path	
S.N.	QWP angle	HWP angle	QWP angle	HWP angle
1	0°	45°	0°	45°
2	0°	45°	0°	0°
3	0°	0°	0°	0°
4	0°	0°	0°	45°
5	0°	22.5°	0°	45°
6	0°	22.5°	0°	0°
7	45°	22.5°	0°	0°
8	45°	22.5°	0°	45°
9	45°	22.5°	0°	22.5°
10	45°	22.5°	45°	22.5°
11	0°	22.5°	45°	22.5°
12	0°	45°	45°	22.5°
13	0°	0°	45°	22.5°
14	0°	0°	90°	22.5°
15	0°	45°	90°	22.5°
16	0°	22.5°	90°	22.5°

where $\lambda_i (i = 1, 2, 3, 4)$ are the eigenvalues in decreasing order of the matrix $\rho\tilde{\rho}$, which is defined as

$$\rho\tilde{\rho} = \rho(\sigma_y \otimes \sigma_y)\rho^*(\sigma_y \otimes \sigma_y) \tag{1.30}$$

where σ_y is the Pauli matrix, ρ is the density matrix of the polarization-entangled state reconstructed through QST, and ρ^* is the complex conjugate of the density matrix. A concurrence (C) value of 0 indicates that the state is completely separable, and C = 1 indicates that the state is maximally entangled. C value of ~ 0.5 indicates the classical threshold i.e. if C > 0.5, it represents the quantum state, and if C is below 0.5, then it shows that the state is classical. Without QST, the lower bound of concurrence i.e. the minimum concurrence of the state, can also be estimated from the two-photon interference visibility via [67]

$$\mathrm{C}(\rho) \geq V_{H-V} + V_{D-A} - 1 \tag{1.31}$$

where V_{H-V} and V_{D-A} are the visibilities in the H-V and D-A basis, respectively.

1.7 Objective of the thesis

The main objective of this work is to design, characterize, and develop an efficient multi-user source of polarization-entangled photon pairs at telecommunication wavelength for long-distance WDM-QKD, secure communication, and metrology applications. The thesis presents a) A LNOI ridge waveguide design for spectrally pure telecom photon generation and a comparison of analytical and numerical solutions of spectral purity measurement. b) A fully fiber-integrated setup based on type-0 quasi-phase-matched Zn-indiffused MgO:PPLN waveguide for the generation of highly spectrally/temporally correlated photon pairs at telecom wavelength. c) A broadband polarization-entangled photon pair source at telecom wavelength. d) The generation and characterization of tunable Bell states in 14 channel pairs of the International Telecommunication Union (ITU) (dense WDM, 100-GHz spacing) grid around 1550-nm for multi-user QKD & communication, and the demonstration of entanglement distribution up to 100 km.

The primary results of this thesis are as follows:

1) A robust LNOI waveguide design for spectrally pure ($\sim 90\%$) telecom photons; a comparison of analytical and numerical solutions of Schmidt decomposition for quantifying spectral purity parameter.

2) Zn-indiffused MgO:PPLN ridge waveguide characterization, along with both theoretical and experimental study of second-harmonic-generation (SHG).

3) Experimental demonstration of broadband generation of spectrally and temporally correlated photon pairs in telecom band (S, C, and L) in Zn-indiffused MgO:PPLN waveguide.

4) Experimental demonstration/verification of a high-brightness source of broadband polarization-entangled photon pairs spanning the telecom C ($\sim$ 1520 - 1550 nm)- and L ($\sim$ 1550 - 1580 nm)-bands.

5) A novel design, along with the experimental characterization of a multi-user source of polarization-entangled photon pairs in 14 different channel pairs of the ITU grid around 1550 nm; experimental demonstration of long-distance transmission (100-km) of polarization-entangled photon pairs through fiber spools and the impact of PMD on entanglement distribution.

1.8 Thesis layout

The thesis structure is as follows: Chapter 1 introduces the background of this field, the definition of all the nonlinear processes involved in the generation of photon pairs, and the parameters used in the characterization of the PPLN source. Chapter 2 discusses the two metrics (joint spectral intensity (JSI), and Schmidt decomposition) used to measure the spectral correlation of photon pairs and also presents a LNOI waveguide design for spectrally pure telecom photon generation. A comparison between the analytical and numerical solutions of spectral purity measurement is also studied in this chapter. Chapter 3 shows a numerical simulation of Zn-indiffused MgO:PPLN ridge waveguide and a theoretical & experimental study of second harmonic generation (SHG) for source characterization. Following this, Chapter 4 presents a complete characterization of a fiber-integrated broadband source of spectrally and temporally correlated photon pairs at telecom wavelength. Chapter 5

demonstrates a broadband source of polarization-entangled photon pairs spanning the telecom C- and L-bands. Finally, Chapter 6 presents a fiber-coupled telecom source of tunable polarization-entanglement for long-distance multi-user QKD and communication. The suitability of the source for long-distance (metropolitan scale) multi-user QKD is shown by the successful transmission of polarization-entangled photon pairs up to a distance of 100 km through single-mode fiber spools; the detailed study of the effect of PMD on entanglement distribution is also presented. Finally, Chapter 7 summarizes the work and discusses the future direction of this research work.

The appendix section A details the characterization of all fiber-optical components (through a classical tunable telecom source) that are used in the experiments (which are presented in this thesis).

Chapter 2

Spectral purity analysis via Schmidt decomposition: LNOI design for spectrally pure telecom photon-pair generation[1]

In this chapter, we discuss two methods, joint spectral intensity (JSI) and Schmidt decomposition, that can be used for SPDC photon pair spectral correlation characterization. We present a detailed derivation of Schmidt decomposition along with a

[1]

Parts of this chapter have been published in the followings
a) Ramesh Kumar, **Vikash Kumar Yadav**, Vivek Venkataraman, and J. Ghosh, "Temporal Properties and Schmidt Decomposition of the Biphoton State in a ppLN Ridge Waveguide", **Frontiers in Optics + Laser Science 2021**, paper JW7A.94.
b) **Vikash Kumar Yadav**, Vivek Venkataraman, and Joyee Ghosh, "Spectral purity of telecom photon pairs from on-chip LNOI waveguides: comparison between analytical and numerical calculations" **Quantum Inf Process** 24, 11 (2025).

simple analytical formula of Schmidt mode coefficients which can be used to calculate the spectral purity of the biphoton state. We also propose an experimentally feasible robust lithium niobate on insulator (LNOI) waveguide design for spectrally pure telecom (1560 nm) photon pair generation and show a comparison between the analytical and exact numerical solutions of Schmidt decomposition by observing the effect of pump bandwidth and waveguide length on spectral purity. The proposed waveguide can be used to generate heralded pure single photons, which have direct applications in quantum computing, communication, and quantum simulation.

2.1 Introduction

The spectral correlation information of photon pairs generated from a quantum light source based on nonlinear optical processes is beneficial in determining its potential application. Spectrally correlated photons are helpful for applications such as quantum cryptography [11, 76], information processing [77], and to mitigate chromatic dispersion in communication [38, 78], whereas applications such as linear optical quantum computing (LOQC) [40], prepare-and-measure based QKD protocols [79], quantum repeaters [50], and other quantum interference experiments [80] require spectrally uncorrelated (pure) high brightness single photon source. The energy and momentum conservation relations associated with nonlinear processes such as SPDC and SFWM generally lead to the generation of spectrally correlated photons [77, 81, 82, 59, 83, 84]. To obtain a pure heralded single-photon source, simply heralding one of the photons does not help as it projects the partner heralded photon into a mixed state, limiting its usability [85]. Also, the spectral correlation filtering through a narrow-band filter degrades the brightness [86], and it limits the degree of purity. The elimination of spectral correlations requires stringent conditions, such

as perfect dispersion engineering, specific pump bandwidth, and crystal length. A pure heralded single photon source based on SPDC or SFWM can be achieved by tailoring these required conditions [85, 87, 88, 89].

Here, we discuss two measures viz. JSI [59, 90, 89] and the Schmidt decomposition [89, 91, 92] to study the spectral correlations of SPDC photon pairs and derive all the essential conditions for spectrally pure biphoton state generation. We present a detailed derivation of Schmidt decomposition and validate our analytical expression of Schmidt coefficients from two published results in the literature. We also propose an on-chip source design based on the LNOI ridge waveguide to generate spectrally pure telecom photons at 1560 nm. The waveguide dimensions and poling period are well within modern nano-fabrication tolerances [42, 93, 94, 95] and justify its practical implementation. The spectral purity of the generated biphoton state is estimated through both analytical and numerical solutions, and a comparison is carried out between the two methods by extensively studying the effect of pump bandwidth and waveguide length on spectral purity. Finally, we check the robustness of the LNOI waveguide by considering the effect of scattering losses on spectral purity. The proposed source can be used as a heralded pure single-photon source in various quantum applications such as communication, multi-port quantum interferometer-based computing, and information processing [41].

2.2 Metrics for spectral correlation measurement

The biphoton state generated from SPDC or SFWM may or may not possess the spectral correlation. This spectral correlation information is vital to undermine the applicability of the source for various quantum applications. Here, we discuss two metrics, JSI and Schmidt decomposition, to measure the spectral correlation of the

biphoton state generated through SPDC. The former gives a qualitative picture of the spectral correlation in the two-photon state, while the latter gives a quantitative measure.

2.2.1 Joint spectral intensity (JSI)

The wave function of an output biphoton state of the SPDC process is defined as [89, 91, 90]

$$|\Psi\rangle \approx S_o \int\int d\omega_s d\omega_i f(\omega_s, \omega_i)\hat{a}^\dagger(\omega_s)\hat{a}^\dagger(\omega_i)\,|vac\rangle \tag{2.1}$$

where S_o is the spatial overlap of pump, signal, and idler modes; $|vac\rangle$ is the vacuum state; $\hat{a}^\dagger(\omega_{s,i})$ is the creation operators of signal, and idler, respectively. $f(\omega_s, \omega_i)$ is the biphoton amplitude or joint spectral amplitude (JSA) function defined as [59, 89, 90, 25]

$$f(\omega_s, \omega_i) = e^{-(\frac{\omega_s+\omega_i-\omega_p}{\sigma_p})^2}\text{sinc}(\frac{\Delta kL}{2})e^{-i\Delta k\frac{L}{2}} \tag{2.2}$$

where L is the crystal or waveguide length, ω_p and σ_p are the pump central frequency and spectral bandwidth, respectively, and Δk is the phase-mismatch as defined earlier. Here, the spectral bandwidth is defined as $\sigma_p = \frac{2\pi c\Delta\lambda_p}{\lambda_p^2}$, where c, λ_p, and $\Delta\lambda_p$ are the speed of light, pump central wavelength, and pump bandwidth respectively. The first term ($e^{-(\frac{\omega_s+\omega_i-\omega_p}{\sigma_p})^2}$) on the right-hand side of Eq. 2.2 corresponds to the pump envelope function (PEF), and the remaining terms correspond to the phase-matching function (PMF). The modulus square of the JSA is the JSI, i.e. JSI = $|f(\omega_s, \omega_i)|^2$.

The JSI profile unveils the spectral correlation present in the biphoton state. In the $[\omega_s, \omega_i]$ or $[\lambda_s, \lambda_i]$ space, if the JSI profile is a circle or normal ellipse parallel to either signal or the idler-axis, then the biphoton state has no spectral correlations (see Fig. 2.1(a)) [89, 85]. The generated photons do not require any tight filtering to

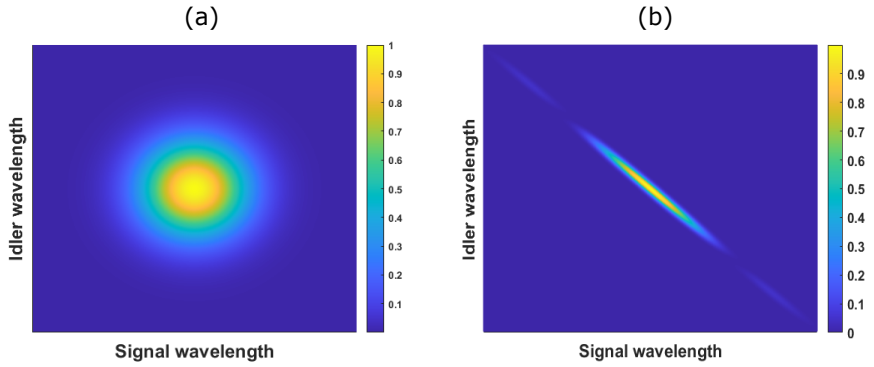

FIGURE 2.1: Schematic of joint spectral intensity (JSI) for (a) spectrally uncorrelated biphoton state (b) spectrally correlated biphoton state.

eliminate the spectral correlations since, in this scenario, the photons are inherently spectrally uncorrelated or pure. Such uncorrelated photon pair source can be used as a heralded pure single-photon source. If the JSI spectrum is an ellipse with an inclination other than 0° and 90° (see Fig. 2.1(b)), it signifies the existence of a finite spectral correlation between the signal and idler photons [89, 96]. These spectrally correlated photons are essential for entanglement-based quantum key distribution and quantum metrology applications [77, 46].

2.2.2 Schmidt decomposition

When a quantum system that is comprised of many interacting subsystems develops correlations in certain parameters amongst the subsystems, the correlation or entanglement can be described by Schmidt decomposition, where a preferred orthonormal basis is constructed to emphasize the correlation [92]. Let us consider a two-component composite system whose state can be written as

$$|\Psi\rangle = \Sigma_{i,j} g_{i,j} |a_i\rangle |b_j\rangle \tag{2.3}$$

where, $|\Psi\rangle \in H$ ($H = H_u \otimes H_v$) (Hilbert state space), is the pure state with density matrix $\rho = |\Psi\rangle\langle\Psi|$. Then there exists a set of orthogonal bases $|u_i\rangle \in H_u$ and $|v_j\rangle \in H_v$ such that $|\Psi\rangle$ can be written as

$$|\Psi\rangle = \Sigma_i c_i |u_i\rangle |v_i\rangle \tag{2.4}$$

where $\Sigma_i |c_i|^2 = 1$. Such a representation is known as Schmidt decomposition [92]. It provides a quantitative method to find the degree of entanglement or separability of the constituent subsystems.

A similar approach can be applied in SPDC, where the JSA can be decomposed to find the spectral correlation of the biphoton state. In general, JSA is not factorable, i.e., $f(\omega_s, \omega_i) \neq \psi(\omega_s)\phi(\omega_i)$, which means that the state is not separable, signifying the presence of spectral correlations. However, under certain conditions, it can be factorized i.e. $f(\omega_s, \omega_i) \approx \psi(\omega_s)\phi(\omega_i)$, which are discussed next in this section. Let us consider a general down-converted signal and idler photon pair through SPDC at frequencies ω_s and ω_i, respectively; let $\bar{\omega_p}, \bar{\omega_s}$ and $\bar{\omega_i}$ are the perfectly phase-matched ($\Delta k = 0$) or central frequencies of pump, signal, and idler, respectively such that $\bar{\omega_p} = \bar{\omega_s} + \bar{\omega_i}$. The phase-mismatch ($\Delta k = k_p(\omega_s + \omega_i) - k_s(\omega_s) - k_i(\omega_i) - \frac{2\pi}{\Lambda}$) is zero only for these central frequencies by the choice of poling period Λ. Now consider a Taylor series expansion up to the first order of the propagation vectors about their respective central frequencies, the phase-mismatch becomes

$$\Delta k = k_p(\bar{\omega_p}) - k_s(\bar{\omega_s}) - k_i(\bar{\omega_i}) - \frac{2\pi}{\Lambda} + (\omega_s + \omega_i - \bar{\omega_p})k_p^{'} - (\omega_s - \bar{\omega_s})k_s^{'} - (\omega_i - \bar{\omega_i})k_i^{'} \tag{2.5}$$

where $k'_\mu = \frac{dk_\mu(\omega)}{d\omega}|_{\omega=\bar{\omega_\mu}}$, $\mu = p, s, i$. Now $k_p(\bar{\omega_p}) - k_s(\bar{\omega_s}) - k_i(\bar{\omega_i}) - \frac{2\pi}{\Lambda} = 0$ since phase matching is perfectly satisfied for the central frequencies. Therefore

$$\Delta k = (\omega_s - \bar{\omega_s})(k'_p - k'_s) + (\omega_i - \bar{\omega_i})(k'_p - k'_i) \tag{2.6}$$

We leave the term $e^{(-i\Delta kL/2)}$ in Eq. 2.2 for the mathematical simplification since JSA can also be defined as $\sqrt{JSI}$. To find an analytical solution, the sinc function in Eq. 2.2 is approximated with a Gaussian function by neglecting the contribution from side lobes ($\text{sinc}(\frac{\Delta kL}{2}) \approx e^{-\gamma(\Delta kL)^2}$). The factor $\gamma = 0.04822$ is chosen such that full width at half maximum (FWHM) of sinc and Gaussian functions are equal [89, 87]. Using this approximation and Δk from Eq. 2.6, we get

$$f(\omega_s, \omega_i) = e^{-A(\omega_s - \bar{\omega_s})^2} e^{-B(\omega_i - \bar{\omega_i})^2} e^{-2C(\omega_s - \bar{\omega_s})(\omega_i - \bar{\omega_i})} \tag{2.7}$$

where $A = \frac{1}{\sigma_p^2} + \gamma(k'_p - k'_s)^2 L^2$, $B = \frac{1}{\sigma_p^2} + \gamma(k'_p - k'_i)^2 L^2$ and $C = \frac{1}{\sigma_p^2} + \gamma(k'_p - k'_s)(k'_p - k'_i)L^2$. It is clear from Eq. 2.7 that the two-photon state or $f(\omega_s, \omega_i)$ is factorable only if $C = 0$ i.e., if $\frac{1}{\sigma_p^2} = -\gamma(k'_p - k'_s)(k'_p - k'_i)L^2$ which is possible if $k'_s < k'_p < k'_i$ or $k'_i < k'_p < k'_s$ (these inequalities implies that the group velocity of the pump should lie between the group velocities of the signal and idler). Thus, for a factorable biphoton state, the first condition is that the pump photon's group velocity should be between the signal and idler photon's group velocity, and then the complete condition (C=0) is satisfied with the help of pump bandwidth and crystal or waveguide length. The effect of pump bandwidth and waveguide length in spectral correlation elimination is detailed later in this chapter.

To characterize the degree of separability of the given biphoton state, we expand the JSA (Eq. 2.7) in frequency eigenbasis such that

$$f(\omega_s, \omega_i) = \Sigma_n \sqrt{\lambda_n} \psi_n(\omega_s) \phi_n(\omega_i) \tag{2.8}$$

where $\Sigma_n \lambda_n = 1$, and $\psi_n(\omega_s)$, $\phi_n(\omega_i)$ are the solutions of eigenvalue equations

$$\int k_1(\omega_s, \omega) \psi_n(\omega) d\omega = \lambda_n \psi_n(\omega_s) \tag{2.9}$$

$$\int k_2(\omega_i, \omega) \phi_n(\omega) d\omega = \lambda_n \phi_n(\omega_i) \tag{2.10}$$

with $k_1(\omega_s, \omega) = \int f(\omega_s, \omega_i) f^*(\omega, \omega_i) d\omega_i$ and $k_2(\omega_i, \omega) = \int f(\omega_s, \omega_i) f^*(\omega_s, \omega) d\omega_s$ [89, 91]. For the biphoton state, which has no frequency correlation, $f(\omega_s, \omega_i)$ is completely factorable i.e., only the first term (n = 0) on the right-hand side of Eq. 2.8 is non-zero, and all other terms (n > 0) are zero; whereas for the biphoton state, which has frequency correlations, $f(\omega_s, \omega_i)$ is not factorable i.e., first few terms (n $\geq$ 0) are non-zero. The degree of factorizability or spectral correlation of the state is quantified by the Schmidt number (K) or the entropy of entanglement (S) [89, 91, 97], given as

$$\mathrm{K} = \frac{1}{\Sigma_n \lambda_n^2} \tag{2.11}$$

$$\mathrm{S} = -\Sigma_{n=0}^{\infty} \lambda_n \log_2 \lambda_n \tag{2.12}$$

The purity of the biphoton state can be calculated from the inverse of K (i.e. purity = $\frac{1}{\mathrm{K}}$) [85, 98]. A high value of S and K indicates a large spectral correlation between signal and idler photon. Specifically, for a non-factorable (entangled) biphoton state i.e., having a finite spectral correlation between photons, K > 1 and S > 0, whereas for a factorable (pure) state i.e. when signal and idler photon do not have any spectral correlation, K = 1 and S = 0 [89, 91, 97].

To obtain the Schmidt coefficient (λ_n), we solve Eq. 2.9 and 2.10 analytically by using $f(\omega_s, \omega_i)$ from Eq. 2.7 and choosing appropriate $\psi_n(\omega)$ and $\phi_n(\omega)$ functions. We first normalize Eq. 2.7 and then used it to find $k_1(\omega_s, \omega)$

$$k_1(\omega_s, \omega) = T\sqrt{\frac{\pi}{2B}} e^{-A((\omega_s-\bar{\omega_s})^2+(\omega-\bar{\omega_s})^2)} e^{\frac{C^2(\omega_s+\omega-2\bar{\omega_s})^2}{2B}} \tag{2.13}$$

where $T = \frac{2\sqrt{AB-C^2}}{\pi}$ is the normalization coefficient of JSA (Eq. 2.7), and then consider $\psi_0(\omega) = e^{\frac{-(\omega-\bar{\omega_s})^2}{\sigma^2}}$, a fundamental Hermite-Gaussian (HG_{00}) function, where σ is the spectral bandwidth of the Gaussian function, and check if it satisfies the eigenvalue Eq. 2.9. The left-hand side (L.H.S) of Eq. 2.9 ($\int k_1(\omega_s, \omega)\psi_n(\omega)d\omega$) results in

$$\text{L.H.S} = \frac{2\sqrt{AB-C^2}}{\sqrt{2AB-C^2+\frac{2B}{\sigma^2}}} exp(-(\omega_s-\bar{\omega_s})^2(A - \frac{C^2}{2B} - \frac{C^4}{2B(2AB-C^2+\frac{2B}{\sigma^2})})) \tag{2.14}$$

This satisfies the eigenvalue equation if $(A - \frac{C^2}{2B} - \frac{C^4}{2B(2AB-C^2+\frac{2B}{\sigma^2})}) = \frac{1}{\sigma^2}$ which leads to the condition that $\sigma = (\frac{B}{A^2B-AC^2})^{1/4}$. Thus we find that $\lambda_0 = \frac{2\sqrt{AB-C^2}}{\sqrt{2AB-C^2+\frac{2B}{\sigma^2}}}$. If we consider $\psi_1(\omega) = \frac{2(\omega-\bar{\omega_s})}{\sigma} e^{\frac{-(\omega-\bar{\omega_s})^2}{\sigma^2}}$, a first order Hermite-Gaussian (HG_{10}) function, and solve the Eq. 2.9 then it gives $\lambda_1 = \frac{2C^2\sqrt{AB-C^2}}{(2AB-C^2+\frac{2B}{\sigma^2})^{\frac{3}{2}}}$. Similarly, a second order HG function will give $\lambda_2 = \frac{2C^4\sqrt{AB-C^2}}{(2AB-C^2+\frac{2B}{\sigma^2})^{\frac{5}{2}}}$. Note that these Schmidt coefficients would be the same if we solve Eq. 2.10 instead of Eq. 2.9.

From the above Schmidt coefficients, we conclude that these follow a geometric progression, and thus, the nth coefficient can be calculated as

$$\lambda_n = \frac{2C^{2n}\sqrt{AB-C^2}}{(2AB-C^2+\frac{2B}{\sigma^2})^{n+\frac{1}{2}}} \tag{2.15}$$

We note that Eq. 2.15 satisfies the condition $\Sigma_n\lambda_n = 1$, and Hermite Gaussian

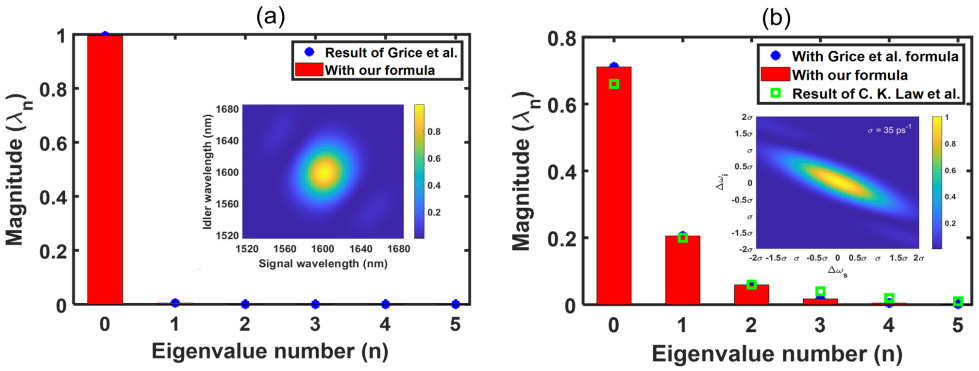

FIGURE 2.2: Reproduced Schmidt decomposition results of (a) Ref. [89] (degenerate type-II SPDC in BBO with pump wavelength = 800 nm, crystal length L = 2.6 mm and pump bandwidth = 15 nm). (b) Ref. [91] ($(k_p^{'} - k_s^{'})L = 0.061$ ps, $(k_p^{'} - k_i^{'})L = 0.213$ ps and $L = 0.8$ mm, $\sigma_p = 35$ ps^{-1}). The insets show the corresponding JSI profiles.

functions are a suitable choice for the functions $\psi_n(\omega_s)$ and $\phi_n(\omega_i)$. The accuracy of our analytical expression of the Schmidt coefficient, given by Eq. 2.15, is verified against two sets of published results of Ref. [89, 91] (The reported results of W. P. Grice et al. [89] are based on an analytical expression [89, 99], and the reported results of C. K. Law et al. [91] are numerically computed.). Figures 2.2(a) and 2.2(b) show the reproduced Schmidt decomposition results for spectrally uncorrelated and spectrally correlated biphoton states, respectively (the insets show the corresponding JSI profile). The results from our analytical expression match well with the published results. For spectrally uncorrelated photon pair (see Fig. 2.2(a)) the calculated K is $\sim$ 1.01, S is $\sim$ 0.05, and purity $\sim$ 99%, whereas, for the spectrally correlated photon pair (see Fig. 2.2(b)) the calculated K is $\sim$ 1.81, S is $\sim$ 1.22, and purity is 55.25%. Further analysis shows that our analytical formula is same as the normalized expression of W. P. Grice et al. [89], but we note that the authors in Ref. [89] have not provided a detailed derivation of the Schmidt coefficients, and the reported expression is not normalized. These missed details are fulfilled in this study.

2.3 Spectrally pure biphoton state from LNOI-ridge-waveguide

The recent developments of the thin-film lithium niobate on insulator (LNOI) photonic platform [100, 101] have given a boost to the on-chip integrated quantum light sources. The condition of spectrally pure biphoton state generation can be easily achieved in these LNOI waveguides because of the geometry-induced dispersion i.e., the group velocities can be tailored by choosing an appropriate waveguide dimension. Here, we propose such an LNOI ridge waveguide to generate spectrally uncorrelated (pure) photons at telecom wavelength via SPDC. The waveguide is X-cut and Y-propagating and has a height of H = 0.72 µm, width of W = 1.2 µm, length of L = 5 mm, and slant angle of $\theta \sim 80°$. Figure 2.3(a) shows the air-clad LNOI waveguide cross-section in which SiO_2 is the substrate and 5% MgO doped lithium niobate (MgO:LN) is the guiding channel, and it is phase-matched for a degenerate type-II SPDC process (780 nm (pump, o-ray) $\rightarrow$ 1560 nm (signal, o-ray) + 1560 nm (idler, e-ray)).

The waveguide modes are numerically analyzed in COMSOL multiphysics using the finite element method by considering the material dispersion through Sellmeier equations (SiO_2 [102] and MgO:LN [103] at room temperature 26°C). The Sellmeier equations are detailed in the Appendix A section. The waveguide-supported fundamental modes at pump, signal, and idler wavelengths (shown in Fig. 2.3(b)) are well confined due to high refractive index contrast. We find that the requisite poling period for the considered type-II down-conversion process is $\Lambda \sim 3.015$ µm. Although the current technology allows such small periodic poling, if there is any fabrication imperfection in the poling period, it can be compensated by tuning the temperature of the waveguide. To generate spectrally pure telecom photon at 1560

nm, we consider a pulsed pump at 780 nm having a FWHM bandwidth of 2 nm and a Gaussian-shaped PEF (see Fig. 2.3(c)), which satisfies the necessary condition of factorizable/pure state generation. Figure 2.3(d) shows the dispersion-engineered PMF, and Fig. 2.3(e) shows the resultant JSA. The JSA profile indicates the generation of a spectrally pure state, and the parameters required to achieve spectral purity are within the practical domain [42].

Our analytical formula (Eq. 2.15) suggests that for the generated biphoton state, the Schmidt number (K) is ~ 1, and the entanglement entropy (S) is ~ 0; however, the exact numerical solution (without Gaussian approximation in PMF) computes K ~ 1.11 and S ~ 0.37 (this corresponds to a purity value of $\sim 90\%$). We notice that both results indicate the generation of spectrally pure telecom photons around 1560 nm though the values from the analytical formula and exact numerical solutions differ slightly. The main reason for this difference is the Gaussian approximation, which disregards the side lobes of the PMF and, hence, the losses in spectral purity. To find a comparison between the two methods, we further investigate their results for different waveguide lengths and pump bandwidths.

2.4 A comparison between analytical and numerical solutions of Schmidt decomposition

In this section, we study the behavior of spectral purity with respect to waveguide length and pump bandwidth. The spectral purity is calculated using both analytical and numerical solutions. For our analytical solution as described above, we have considered PMF as a Gaussian function (i.e., we have taken only the central lobe of the sinc function), whereas, for the numerical solution, we consider the PMF to

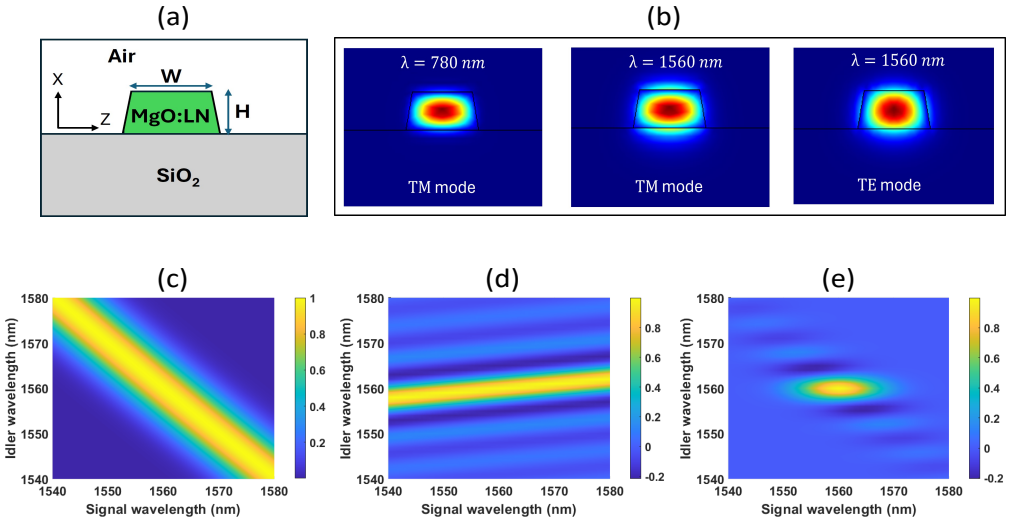

FIGURE 2.3: (a) Schematic of an X-cut LNOI ridge waveguide which is phase-matched for type-II degenerate SPDC process: 780 nm (pump, o-ray) → 1560 nm (signal, o-ray) + 1560 nm (idler, e-ray). The waveguide cross-section is H = 0.72 µm, W = 1.2 µm. (b) Waveguide-supported modes at pump, signal, and idler wavelengths. (c) Pump (780 nm) envelope function (PEF) with bandwidth ($\Delta\lambda_P$) 2 nm. (d) Phase-matching function (PMF) for waveguide length (L) 5 mm. (e) Joint spectral amplitude (JSA) indicating the generation of spectrally uncorrelated (pure) photons.

be the exact sinc function. Here (for the numerical solution), we consider a large wavelength range (1460 nm - 1660 nm) for the calculation of PEF, PMF, and JSA such that the effect of a large number of side lobes of sinc function can be taken into the calculation.

Figures 2.4(a) and 2.4(b) show the effect of pump bandwidth on spectral purity for fixed waveguide lengths of 5 mm and 13 mm, respectively. From Fig. 2.4(a) and its inset, we notice that a detuning of the pump bandwidth (from 2 nm) increases K and S and decreases the purity, i.e. causing a transition from the spectral pure to spectrally correlated photon pair generation. A careful observation of both figures (2.4(a) and 2.4(b)) shows that the analytical formula slightly overestimates the spectral purity than the exact numerical solution, and the two methods agree only for the smaller pump bandwidths. Similarly, Fig. 2.4(c) and 2.4(d) show the effect of waveguide length on K/purity at a fixed pump bandwidth of 2 nm and 15 nm,

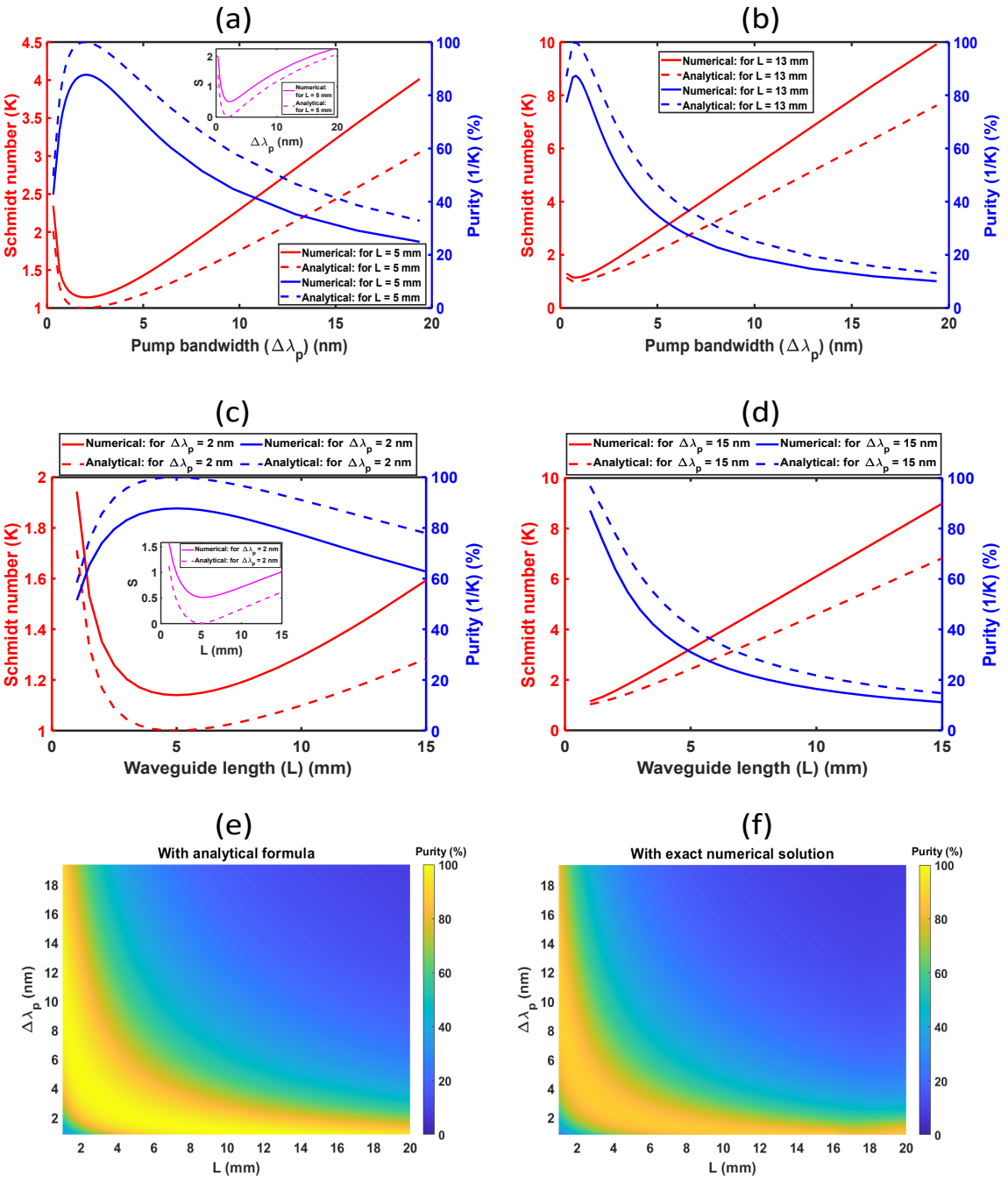

FIGURE 2.4: Effect of pump bandwidth on Schmidt number (K) and Purity (1/K) using analytical formula and exact numerical solution for fixed waveguide length (a) L = 5 mm (b) L = 13 mm. Effect of waveguide length on Schmidt number (K) and Purity (1/K) using analytical formula and exact numerical solution for fixed pump bandwidth (c) $\Delta\lambda_p = 2$ nm (d) $\Delta\lambda_p = 15$ nm. Insets show the variation of entropy of entanglement (S). Surface plot of purity for different waveguide lengths and pump bandwidths using (e) analytical formula (Eq. 2.15) (f) exact numerical solution.

respectively. Again, we note that (from Fig. 2.4(c) and its inset) a detuning of the waveguide length from 5 mm increases K and S and decreases the purity. Both Figs. 2.4(c) and 2.4(d) suggest that the analytical solution slightly overestimates the purity, and the two methods agree for smaller waveguide lengths. To completely understand the effect of pump bandwidth and crystal length on spectral purity, we show the surface plot through both the analytical expression (Fig. 2.4(e)) and exact numerical solution (2.4(f)). The analytical solution shows a slightly higher tolerance in the pump bandwidth and waveguide length than the exact numerical solution for highly spectrally pure state generation.

From the above results, we conclude that under very specific conditions or critical parameters (in this case $\Delta\lambda = 2$ nm, L = 5 mm), a source generates spectrally pure photons and a deviation from these conditions leads to a large spectral correlation in the output biphoton state. This can be understood in the following manner, for example, for fixed waveguide dimensions and fixed pump, signal and idler wavelengths, the terms γ, $k_p^{'}$, $k_s^{'}$, $k_i^{'}$ and L are fixed thus only a certain value of pump bandwidth (σ_p) will satisfy the condition $\frac{1}{\sigma_p^2} = -\gamma(k_p^{'} - k_s^{'})(k_p^{'} - k_i^{'})L^2$ and will make C = 0 (see Eq. 2.7) i.e. will make the JSA factorizable or, in other words, the waveguide will generate spectrally pure photons. A deviation from this condition will make C $\neq$ 0 and thus lead to large spectral correlations, because now Eq. 2.7 is no longer factorizable or separable. We note that the numerical solution yields lower spectral purity than the analytical formula, which shows that the side lobes of sinc degrade the purity. The side lobes can be suppressed to achieve high purity by employing an appropriately apodized quasi-phase-matched (QPM) poling pattern, resulting in a Gaussian-shaped PMF [104]. The photon pair spectrum can also be filtered to suppress the side lobes, which will enhance the purity value close to the predicted value of the analytical formula. Thus, the analytical expression can be safely used

to compute the correct Schmidt number or purity if the output state is either filtered or an apodized QPM poling pattern (resulting in a Gaussian-shaped PMF) is used in the crystal or waveguide. This suggests that the results of the analytical and numerical solutions will converge when the effect of side-lobes in PMF (in sinc function) is minimized.

2.5 Effect of scattering loss on spectral purity

In LNOI ridge waveguides, the main source of propagation loss is the scattering loss, and it arises from the rough sidewalls, which are a result of fabrication limitations [105]. Here, we have studied the impact of scattering losses on the spectral purity of the biphoton state. As the pump, signal, and idler photon propagate through

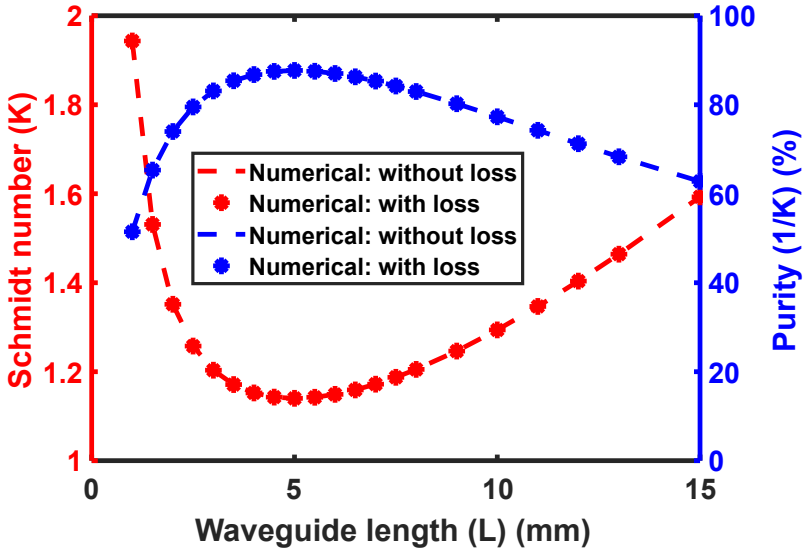

FIGURE 2.5: Effect of LNOI ridge waveguide length on Schmidt number (K) and purity (1/K) in presence and absence of scattering loss at fixed pump bandwidth (2 nm). Here, spectral purity is calculated using the exact numerical solution; the scattering losses of pump, signal, and idler photons are considered as 4 dB/cm, 2 dB/cm, and 2 dB/cm, respectively.

the LNOI ridge waveguide, they experience scattering from the sidewall roughness

of the ridge channel, and in such a scenario, the JSA becomes [105]

$$f(\omega_s, \omega_i) \approx e^{-(\frac{\omega_s+\omega_i-\omega_p}{\sigma_p})^2} e^{\frac{\alpha_p L}{4}} e^{-(\alpha_s r_s+\alpha_i r_i)\frac{L}{4}} \text{sinc}[(\delta k - i\frac{(\alpha_s r_s + \alpha_i r_i - \alpha_p)}{2})\frac{L}{2}] \quad (2.16)$$

where $\delta k = (\frac{2\pi}{\Lambda} + k_s + k_i - k_p)$; $\alpha_{p,s,i}$ are the propagation losses of pump, signal, and idler photons due to scattering from the sidewall roughness of the ridge channel, respectively; $r_s = \frac{V_s}{V_p}$ is the ratio of group velocities of signal (V_s) and pump (V_p), and $r_i = \frac{V_i}{V_p}$ is the ratio of group velocities of idler (V_i) and pump (V_p) photon. For our LNOI ridge waveguide dimensions, the typical values of scattering losses without any advanced fabrication techniques are approximately $\alpha_p(780 \text{ nm}) = 4$ dB/cm, $\alpha_s(1560 \text{ nm}) = 2$ dB/cm, and $\alpha_i(1560 \text{ nm}) = 2$ dB/cm respectively [93, 94, 106]. For our wavelength region of interest (1460 nm - 1660 nm), we consider a constant loss profile, and we numerically compute the JSA to find the spectral purity. Figure 2.5 shows the effect of waveguide length on spectral purity at fixed pump bandwidth (2 nm) in the presence and absence of scattering loss. We notice that the spectral purity and K remain the same for both cases, which indicates that the scattering losses do not affect the spectral purity, thus highlighting the robust nature of the waveguide.

2.6 Conclusion

We present a comprehensible derivation of analytical formulae that can be used to find the Schmidt mode coefficients (λ_n) in an SPDC-biphoton state. The analytical expression (Eq. 2.15) is verified against two sets of published results (Ref. [89] and [91]), and it satisfies all the necessary conditions of Schmidt decomposition and can be used to find the spectral correlation between photon pairs generated in any SPDC process. We also present an experimentally feasible LNOI ridge waveguide

design to generate spectrally pure telecom photons at 1560 nm using type-II SPDC. The estimated spectral purity of the biphoton state is $\sim 90\%$ (obtained through the numerical solution) without any external filtering. We compare our analytical expression of Schmidt decomposition with the exact numerical solution by extensively studying the effect of pump bandwidth and waveguide length on spectral purity or K number. The results show that under very specific conditions, a source can generate spectrally pure photons, and a slight deviation from these conditions leads to a large spectral correlation in the output biphoton state. The results from these two methods converge when the effect of side lobes of PMF is minimized.

We also note that the scattering losses in the LNOI ridge waveguide do not affect the spectral purity of the generated biphoton state. The proposed on-chip source design generates degenerate spectrally pure photons at telecom wavelength that can be used in multi-port quantum interferometer-based applications like quantum computing, quantum simulation, and communication [40, 79, 50, 80, 41]. Further, these degenerate photons can be entangled in the polarization degree-of-freedom either through post-selection [107] or via a Sagnac interferometer [108] with simple optics. Thus, the proposed source can provide simultaneous spectrally-pure polarization-entangled photon pairs, which is required for most photonic quantum computing schemes [41, 109, 36, 110].

Chapter 3

SHG characterization in a Zn-indiffused MgO:PPLN ridge waveguide[1]

In this chapter, we present a numerical modal analysis of Zn-indiffused MgO:PPLN ridge waveguide and experimental demonstration of second harmonic generation (SHG). The waveguide supports near circular quasi-TM modes at 775 nm (multi-mode) and 1550 nm (single-mode), which are the wavelengths of our interest. The waveguide is commercially available, but we customize it slightly, i.e. we ask the manufacturer to fiber-pigtail it with PM 1550 fibers on both ends because we use this waveguide in the Sagnac configuration for entanglement generation later in Chapter 5 and Chapter 6. Here, we characterize two such Zn-indiffused MgO:PPLN ridge

[1]

Part of this chapter has been published in -**Vikash Kumar Yadav**, Vivek Venkataraman, and Joyee Ghosh, "Broadband telecom photon pairs from a fiber-integrated PPLN ridge waveguide", **Optics Letters** 47(19), 5132-5135 (2022).

waveguides having a phase-matching temperature of 41°C and 36.5°C, respectively, via SHG. The experimentally observed normalized SHG efficiency of both waveguides are $\sim 30\%/\text{W}$ and $\sim 40.4\%/\text{W}$, respectively. The efficient SHG generation in these waveguides from off-the-shelf telecom lasers shows that these waveguides can be used in frequency-doubled lasers, high-resolution optical microscopy, and quantum devices (for telecom photon generation through the SPDC process).

3.1 Introduction

The guided-wave optics provides an efficient way to implement linear and nonlinear photonic circuits for many practical applications such as telecommunication, sensing, imaging, and advanced quantum technologies [53, 37]. The guided wave approach provides low loss, high confinement, enhanced nonlinear effects, and less sensitivity to optical alignment, which results in improved efficiency [53]. Processes such as guided wave SHG have applications in high-resolution optical microscopy [111], frequency-doubled lasers [112], and ultra-short pulse characterization [113]. It is also an important first step in the characterization of a quantum light source as well [114]. Here, our primary interest in SHG is solely for the characterization of fiber-integrated Zn-indiffused MgO:PPLN ridge waveguide for quantum applications. As we described earlier, SHG and SPDC are two reverse processes that have the same phase-matching parameters [114]. Though the latter is a quantum process that generates quantum light, the former is easy to perform and detect (generation at a near-visible wavelength in our case), and it also helps in determining the waveguide efficiency and its operating parameters such as temperature, wavelengths, etc beforehand for SPDC process.

In this chapter, we first study the Zn-indiffused MgO:PPLN ridge waveguide through numerical simulation to find the supported modes and theoretically expected SHG signal. Later, we show the experimental generation of the SHG signal at near-visible wavelength and study the effect of pump wavelength, waveguide temperature, and pump power on the SHG signal.

3.2 Zn-indiffused MgO:PPLN ridge waveguide

In this section, we study a Zn-indiffused MgO:PPLN ridge waveguide whose dimensions are height (H) = 10 µm, width (W) = 10 µm and length (L) = 4 cm (Covesion Ltd.: WGP-1550-40_18.5µm, S.N. Y1299_S9) (see Fig. 3.1(a)). The waveguide has a poling period of 18.5 µm and is fabricated in z-cut (i.e., "z" denoting the optic-axis points in the vertical direction) MgO doped lithium niobate (MgO:LN) substrate. It is phase-match for the following SHG process $V_p(1550-nm, pump)+V_p(1550-nm, pump) \rightarrow V_s(775-nm, signal)$, where $V_{p,s}$ is the vertically polarized pump, and signal respectively (values in the parenthesis denotes the corresponding wavelengths) or in other words for the following SPDC process $V_p(775-nm, pump) \rightarrow V_s(1550-nm, signal)+V_s(1550-nm, idler)$, where $V_{p,s,i}$ are the vertically polarized pump, signal, and idler photon, respectively. The waveguide is type-0 phase-matched to access the highest nonlinear coefficient (d_{33} = 25.3 pm/V [115]) of the d-tensor matrix of lithium niobate ($LiNbO_3$, LN).

$$d \text{ tensor matrix of thium niobate} = \begin{pmatrix} 0 & 0 & 0 & 0 & d_{31} & -d_{22} \\ -d_{22} & d_{22} & 0 & d_{31} & 0 & 0 \\ d_{31} & d_{31} & d_{33} & 0 & 0 & 0 \end{pmatrix}.$$

Here d_{22} = 2.59 pm/V, d_{31} = 4.85 pm/V, and d_{33} = 25.3 pm/V [115].

3.2.1 Refractive index modeling

The waveguide is fabricated by coating a metallic Zn layer onto the MgO:PPLN wafer using a commercial sputter tool, followed by the diffusion process in a furnace with an oxygen atmosphere, and finally, it is optically diced in ridge shape such that the cut depth exceeds the diffused layer [116]. According to the manufacturer (Covesion Ltd), the optimum parameters for the diffusion process are diffusion time (t_{diff}) = 1 h, diffusion temperature (T_{diff})= 950°C, and Zn film thickness (d) = 100 nm [116, 117]. For these specified parameters, we find that the diffusion coefficient (D) = 8.5 $\frac{\mu m^2}{h}$ and change in refractive index per mole concentration of Zn ($\frac{\Delta n_e}{Zn(mole\%)}$) = 1.22×$10^{-3}$ [118]. Since the diffusion is only along one dimension (1-D), i.e., along the z-cut axis of the MgO:PPLN waveguide, the Zn concentration profile can be obtained using the 1-D diffusion equation

$$\frac{\partial C}{\partial t} = D\frac{\partial^2 C}{\partial z^2} \tag{3.1}$$

where t is the diffusion time, D is the diffusion coefficient, and C is the concentration. Let t_1 be the depletion time, i.e., the time taken by the whole Zn film (deposited on top) to diffuse into the MgO:PPLN substrate. When $t < t_1$ the solution of Eq. 3.1 will be a complementary error function

$$C(z,t) = C_0(erfc(\frac{z}{4Dt})) \tag{3.2}$$

where mass conservation gives $t_1 = (\frac{kd}{1.128C_0})^2 \frac{1}{D}$ with $k = \frac{\rho(Zn)M_{MgO:LN}}{\rho(MgO:LN)M_{Zn}} = 2.23$. On the other hand, if $t > t_1$, then the solution is given by

$$C(z,t) = (\frac{kd}{\sqrt{\pi Dt}}) \exp\left\{\frac{-z^2}{4Dt}\right\} \tag{3.3}$$

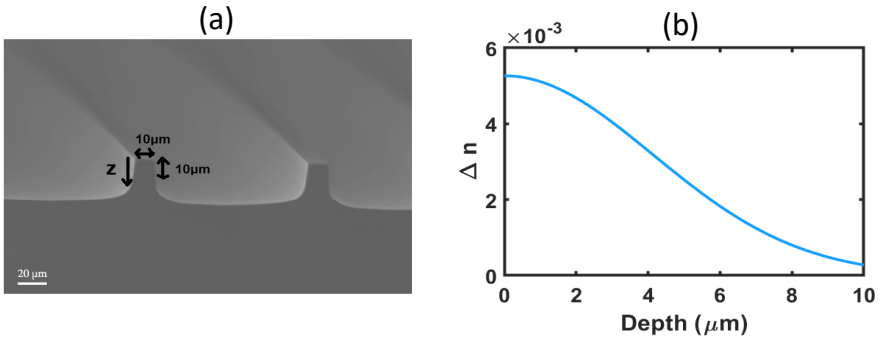

FIGURE 3.1: (a) Scanning electron microscope (SEM) image of Zn-indiffused MgO PPLN ridge waveguide (credit-Covesion Ltd) [116]. (b) Change in refractive index due to Zn diffusion along waveguide depth.

In our case, the diffusion time is much greater than t_1, so Eq. 3.3 can be used to calculate the concentration $C(z,t)$ which, when multiplied by $\frac{\Delta n_e}{Zn(mole\%)}$ will give us the refractive index change due to Zn diffusion.

$$\Delta n = \frac{C(z,t)\Delta n_e}{Zn(mole\%)} \tag{3.4}$$

Figure 3.1(b) shows the change in refractive index over the depth of the waveguide, and we note that the depth at which Δn becomes $\frac{1}{e}$ of its maximum value is 5.83 μm (which is in agreement with the manufacturer- that Zn diffusion is limited to within 10 μm depth of the waveguide). This calculation of Zn-indiffusion and the corresponding change in refractive index serves as the recipe in our numerical simulation of this waveguide, which is shown in the next section.

3.2.2 Numerical modal analysis of the waveguide

We simulate the waveguide geometry shown in Fig. 3.2(a) in COMSOL Multiphysics to see the modal field profiles. First, in order to check the correctness of our simulation structure, we have plotted the variation of the refractive index along waveguide depth (see Fig. 3.2(b)) from the data generated through COMSOL. This shows that

the effect of Zn-indiffusion is correctly considered in the waveguide simulation. The red circles of Fig. 3.2(b) represent the refractive index values that are obtained from the simulated waveguide in COMSOL by fixing the X coordinate and varying the Y coordinate value and then finding the refractive index value at each (X, Y) point. Thus, we effectively obtained the refractive index along the waveguide depth. The inset of Fig. 3.2(b) shows the n_{eff} value for 775-nm and 1550-nm wavelengths at different waveguide temperatures which is obtained by mode analysis. We then use the numerical finite element method (FEM) in COMSOL to extract the supported transverse magnetic (TM) modes (having vertical polarization) and the corresponding effective refractive indices (n_{eff}) at the phase-matched wavelengths. The material dispersion of 5% MgO doped lithium niobate is included through the Sellmeier equation [103], which considers the effect of both wavelength and temperature (see Appendix A for more details on Sellmeier equation). The n_{eff} of the fundamental modes (TM_{00}) of this waveguide has near-linear temperature dependence at phase-matched wavelengths (775 nm (pump) and 1550 nm (signal/idler), see inset of Fig. 3.2(b)). Figure 3.2(c) and 3.2(d) show the fundamental modes of the waveguide at 775 nm and 1550 nm, respectively. The waveguide has a single-mode operation at telecom wavelengths around 1550 nm and multi-mode at 775 nm (higher order modes are also supported, not shown here). We note that the fundamental modes at both wavelengths are well confined and near-circular (Gaussian), resulting in high mode overlap ($\sim 70.9\%$) and efficient coupling into and out of standard single-mode fibers.

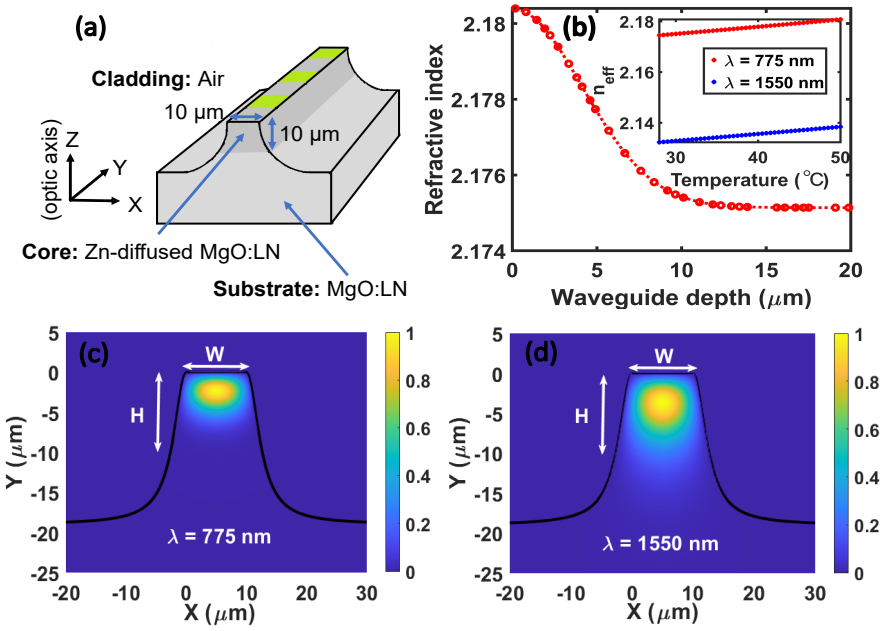

FIGURE 3.2: (a) Zn-indiffused MgO:PPLN ridge waveguide structure. (b) variation of refractive index along waveguide depth. Inset shows the variation of n_{eff} versus waveguide temperature. (c) Fundamental mode at 775 nm. (d) Fundamental mode at 1550 nm.

3.3 SHG in Zn-indiffused MgO:PPLN waveguide

In this section, we have experimentally characterized two Zn-indiffused MgO:PPLN waveguides (dimensions as defined earlier), which we will later use for spectrally correlated and/or polarization-entangled photon pair generation (through SPDC). To characterize these waveguides, we perform SHG and study their efficiency and phase-matching parameters such as waveguide temperature, phase-matching wavelengths, etc. We also compare our experimental results with the theoretically expected results, which we have found through the numerical simulation of the waveguide. As introduced earlier in Chapter 1, a priori phase-mismatch (Δk) is not zero for SHG to take place due to dispersion, but it is possible to make $\Delta k = 0$ using the QPM technique which leads to the phase-matching condition $\Delta k = \frac{2\pi}{\lambda_s}(n_{eff})_s - 2\frac{2\pi}{\lambda_p}(n_{eff})_p - \frac{2\pi}{\Lambda}$. Here, we will exploit this condition in two PPLNs to generate SHG at near visible wavelength.

3.3.1 Waveguide 1

Our first waveguide is phase-matched for vertically polarized 1550 nm to vertically polarized 775 nm generation i.e. the pump wavelength is 1550 nm, and the SHG signal wavelength is 775 nm.

3.3.1.1 Experimental setup

Figure 3.3(a) and 3.3(b) show the schematic and on-table experimental setup for SHG, respectively. The Zn-indiffused MgO:PPLN waveguide (WGP-1550-40_18.5µm, S.N. Y1299_S9) is mounted on an oven and is butt coupled to polarization-maintaining fibers (PM 1550-nm) on both sides. The whole assembly is packaged in a box such that the temperature of the waveguide (mounted on an oven), can be tuned with an external temperature controller (OC2). A C-L band telecom tunable laser (EXFO: T100S-HP-CL) with a maximum power $\sim$ 19 mW is connected to a single-mode fiber (SM 1550-nm) of 1-m length to pump the Zn-indiffused MgO:PPLN waveguide. The waveguide output is collected via another single-mode fiber (SM 775-nm) of 1-m length and then collimated into free space. A dichroic mirror is placed after the collimator to filter out the SHG signal (775 nm) from the pump beam (1550 nm). Finally, a power meter with a photodiode sensor is used to measure the power of the SHG signal.

3.3.1.2 Results

We pump the waveguide at 1550 nm with $\sim$ 17 mW power i.e. the power at the end of SM 1550 fiber, and monitor the generated SHG signal power through a power meter as we tune the waveguide temperature through a temperature controller. Figure

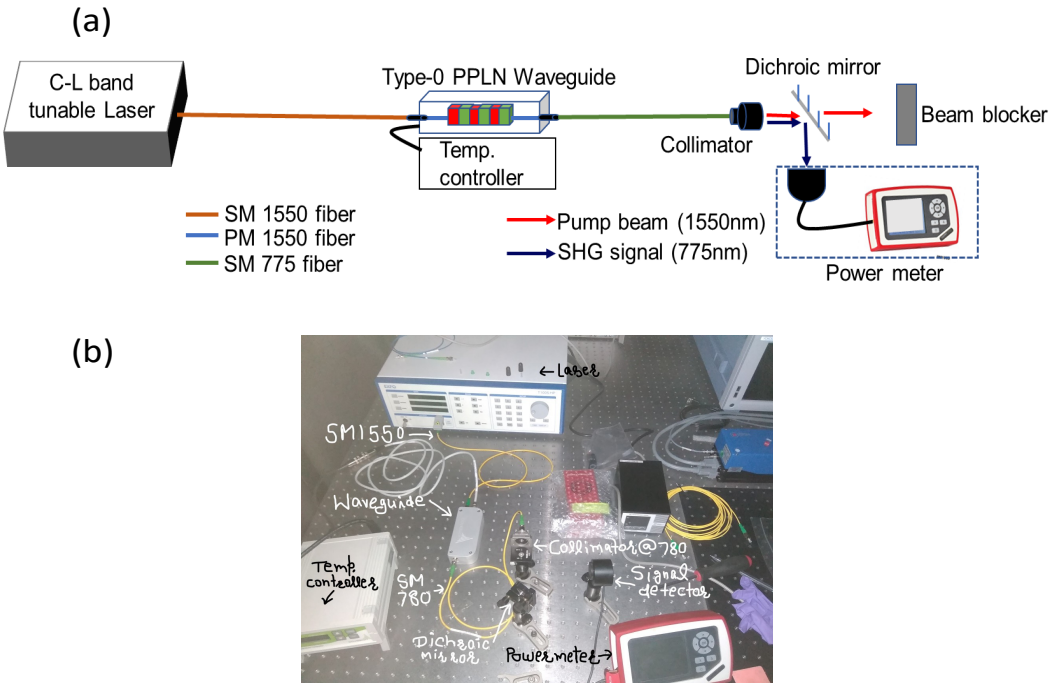

FIGURE 3.3: (a) Schematic of the experimental setup for second harmonic generation (SHG) in Zn-indiffused MgO:PPLN ridge waveguide. (b) Real setup of SHG on an optical table. SM 775 or SM 780 fiber: Single-mode fiber at 775 nm, SM 1550: Single-mode fiber at 1550 nm, PM 1550: Polarization-maintaining fiber at 1550 nm.

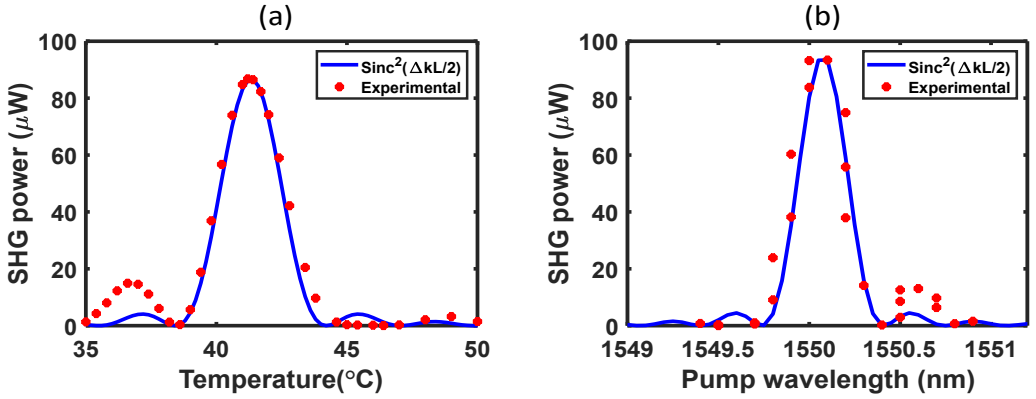

FIGURE 3.4: (a) Effect of waveguide temperature on SHG power. The waveguide input pump power is $\sim$ 17 mW, and the pump wavelength is fixed at $\sim$ 1550 nm. (b) Effect of pump wavelength on SHG power. The waveguide temperature and pump power are fixed at $\sim$ 41°C and $\sim$ 17 mW, respectively. The red dots represent the experimental data, and the solid blue curve is the theoretical $\text{sinc}^2(\frac{\Delta kL}{2})$.

3.4(a) shows the effect of waveguide temperature on SHG power where the red dots are the experimental value, which follows a sinc^2 profile, and the solid blue line is the theoretically expected variation. The results indicate a maximum SHG power generation of $\sim$ 87 µW at $\sim$ 41℃, which corresponds to a normalized conversion efficiency of $\sim$ 30%/W ($\eta = \frac{P_{out}}{P_{in}^2} = \frac{0.087\text{mW}}{17\text{mW}\times 17\text{mW}} \approx 30\%/\text{W}$). The FWHM bandwidth is $\sim$ 2.5℃, which indicates that to harness the maximum efficiency, we have to keep the waveguide within 41 $\pm$ 1.25℃. Figure 3.4(b) shows the effect of pump wavelength on SHG power at constant waveguide temperature (41℃) and pump power ($\sim$ 17 mW). This also follows the sinc^2 behavior, where the dots represent the experimental values and the solid blue line is the theoretically estimated behavior. We note that the SHG process is perfectly phase-matched for only 1550 nm, and a slight deviation decreases the SHG efficiency. A slightly different pump wavelength can be phase-matched by tuning the waveguide temperature as the device has a slope of $\sim$ 0.105 nm/℃ i.e. if we want to phase-match 1550.5 nm for SHG, then we have to keep the waveguide at $\sim$ 45.7℃. In Fig. 3.4(a) and 3.4(b), the theoretical behavior ($\text{sinc}^2(\frac{\Delta kL}{2})$, where Δk is the phase-mismatch for SHG, as mentioned above) is plotted using the n_{eff} data obtained through the waveguide simulation in COMSOL. The theoretical sinc^2 (which has a maximum value of 1) is multiplied by the maximum experimental value to match the peak of the experimental and simulated curves. The theoretical and experimental results are in good agreement, especially the main central lobe; the slight asymmetry and larger sidelobes in our experimental results could be due to inhomogeneous Zn doping along the waveguide length and/or the non-uniformity of the width and/or poling period of the waveguide [119], and fabrication limits of the waveguides [120].

For the theoretical results, we use a poling period of $\sim$ 18.33 µm with a small tolerance of 0.006 µm to get the best fit with the experimental result. Since, in

the experiment, a small change in the parameters, namely pump wavelength or temperature of the waveguide, can lead to a slight deviation of the experimental result from theory. We have compensated for this with the help of tolerance in the poling period. We find that our poling period of 18.328 ± 0.006 µm is less than the nominal value of 18.5 µm given by the manufacturer. This difference might be due to the indirect temperature dependence of the poling period and/or the non-uniformity of the poling period along the waveguide length. A similar discrepancy in the poling period has also been reported by Ref. [77].

The above results outline that the maximum efficiency of this device can be harnessed by operating it at a phase-matching temperature (41℃) and using an exact phase-matched wavelength. There is a large scope for further improvement in the SHG efficiency in our system; for example, by carefully controlling the input pump polarization, the efficiency can be enhanced (here, due to the unavailability of a polarization controller at 1550 nm, we could not optimize the input polarization perfectly). In the next section, we have characterized another Zn-indiffused MgO:PPLN waveguide where the input polarization is also optimized for maximum SHG conversion.

Note: We use this waveguide with Covesion's OC2 temperature controller module. If we use this waveguide with another temperature module, say OC3, the phase-matching temperature might vary slightly, depending on the cable and the temperature controller module used (According to the manufacturer). We note that even with Covesion's OC2 temperature controller, our waveguide's phase-matching temperature varied slightly with different ambient temperatures, indicating that the whole assembly (packed waveguide, see Fig. 3.3(b)) was not thermally insulated. We got better consistency in phase-matching temperature when we kept the waveguide assembly in a thermally insulated box (a box made with polystyrene foam).

Later in Chapter 4, we use this waveguide (Waveguide 1) for the SPDC process.

3.3.2 Waveguide 2

Our second waveguide (Covesion: WGP-S-1550-40-custom) is the same as the first waveguide, but it has a high-quality thermally insulated case (see Fig. 3.5), which gives high consistency in the phase-matching temperature even with different ambient conditions. We procured it much later when our Waveguide 1 was damaged, which is why it has a different casing and different model number, and we utilize this device (Waveguide 2) for the results of Chapter 5 and 6 of this thesis. Waveguide 2 is also phase-matched for the same SHG process, i.e., vertically polarized 1550 nm (pump) generates the vertically polarized 775 nm (SHG signal).

3.3.2.1 Experimental setup

Figure 3.5 shows the schematic of the experimental setup for SHG in the second Zn-indiffused MgO:PPLN waveguide (Waveguide 2). The experimental setup is the same as described earlier, except here, we use OC3 temperature controller and a fiber polarization controller (Thorlabs) at 1550 nm in the input side of the waveguide. We optimize the input pump polarization for maximum SHG and study the effect of pump wavelength, pump power, and waveguide temperature on the SHG signal.

3.3.2.2 Results

Figure 3.6(a) shows the effect of waveguide temperature on SHG signal power at fixed pump wavelength $\sim$ 1550-nm and pump power $\sim$ 13.5 mW. The temperature dependence follows the expected sinc^2 profile where the slight asymmetry in the

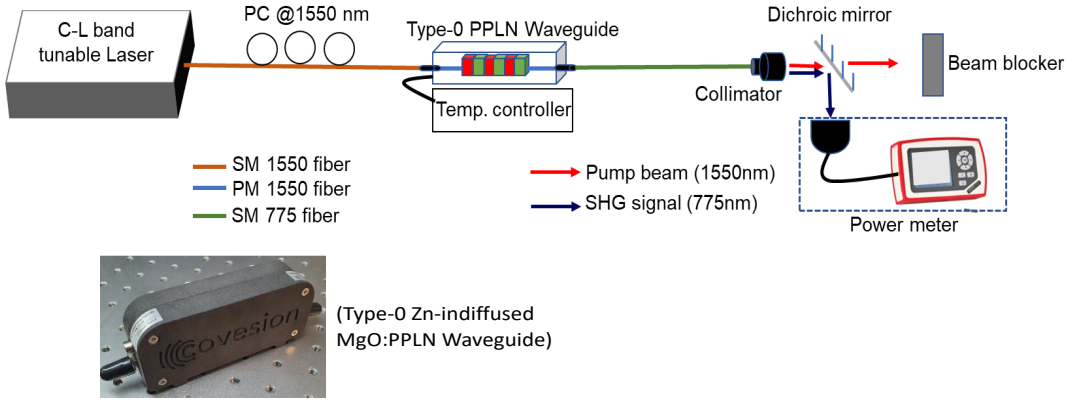

FIGURE 3.5: Schematic for efficient second harmonic generation (SHG) in Zn-indiffused MgO:PPLN ridge waveguide via input pump polarization optimization. SM 775 fiber: Single-mode fiber at 775 nm, SM 1550: Single-mode fiber at 1550 nm, PM 1550: Polarization-maintaining fiber at 1550 nm, PC @ 1550 nm: Polarization controller at 1550 nm.

pattern could be due to fabrication imperfections. We note that the maximum SHG power is $\sim$ 73.8 µW at 36.5℃, which corresponds to a normalized conversion efficiency of $\sim$ 40.4%/W ($\eta = \frac{P_{out}}{P_{in}^2} = \frac{0.0738\text{mW}}{13.5\text{mW}\times 13.5\text{mW}} \approx 40.4\%/\text{W}$). A slight detuning of waveguide temperature from the phase-matching temperature (36.5℃) results in a significant drop in SHG power. The FWHM bandwidth is $\sim$ 2.55℃, which indicates that to harness the maximum efficiency, we have to keep the waveguide within 36.5 $\pm$ 1.27℃.

We notice that though this waveguide is the same as the first waveguide, it has a different phase-matching temperature. This could be due to waveguide fabrication limitations because if there is a slight difference in the fabrication parameters or optical dicing, it will change the n_{eff} of phase-matching wavelengths slightly, which then requires a different temperature to phase-match the process for the same poling period of the waveguide, or if the poling period of the waveguide is slightly different for the same structure then also it would require a slightly different temperature for perfect phase-matching. For example, the solid blue line that fits the experimental data is a theoretical $\text{sinc}^2(\Delta kL/2)$, where Δk is obtained through simulation data

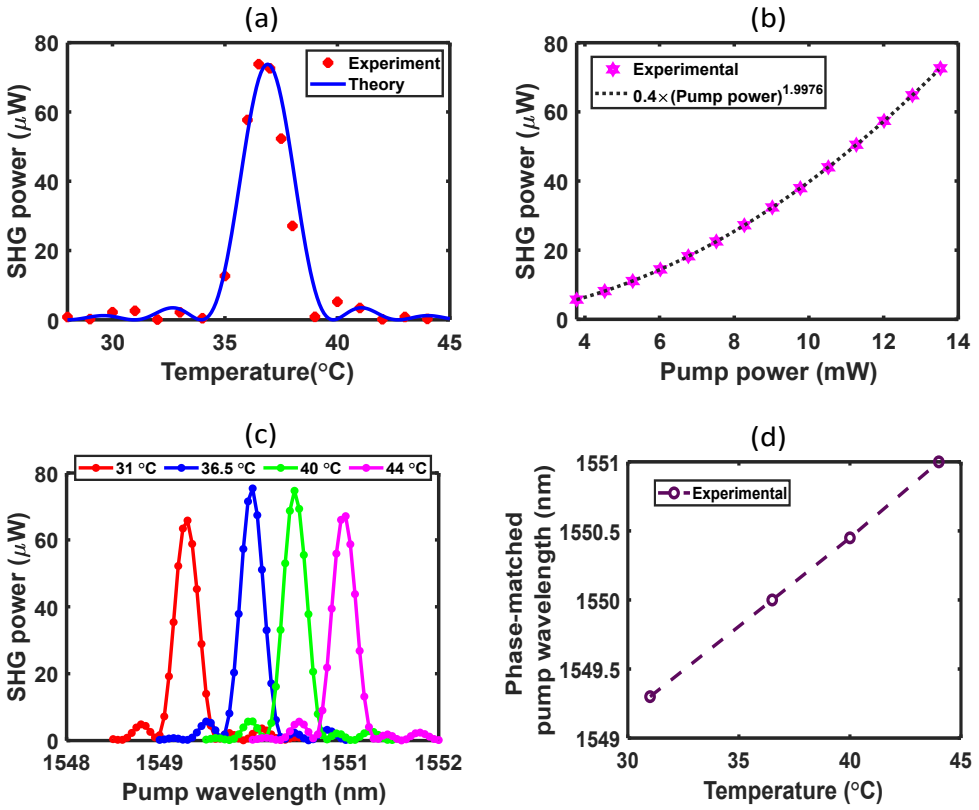

FIGURE 3.6: (a) Effect of waveguide temperature on SHG power at fixed pump wavelength ($\sim$ 1550-nm) and pump power ($\sim$ 13.5-mW). The red dots are the experimental points, and the solid blue line is the theoretical sinc^2. (b) Effect of pump power on SHG power at fixed pump wavelength ($\sim$ 1550-nm) and waveguide temperature ($\sim$ 36.5℃). (c) Effect of pump wavelength on SHG power at different waveguide temperatures (31℃, 36.5℃, 40℃, 44℃) for constant pump power. (d) The dependence of phase-matched pump wavelengths on waveguide temperature.

of the previous waveguide by considering the n_{eff} at 36.5℃ and a poling period of $\sim$ 18.34 µm (which is slightly different from the poling period of the previous waveguide). This shows that if there is a slight change in waveguide fabrication or poling, then it would be phase-matched at a different temperature.

Figure 3.6(b) shows the effect of input pump power on the SHG signal at fixed pump wavelength $\sim$ 1550-nm. We operate the waveguide at the phase-matching temperature (36.5℃) and gradually increase the input pump power. The SHG power increases with an increase in input power, as shown by the magenta-colored stars. We fit the experimental data and find that the SHG power has a quadratic dependence

on input pump power. Figure 3.6(c) shows the effect of pump wavelengths on SHG power at different waveguide temperatures. We fix the waveguide at four different waveguide temperatures i.e. 31℃, 36.5℃, 40℃, and 44℃, and scan the pump wavelength. It is clear that different pump wavelengths can be phase-matched at different temperatures, and they have linear dependence (slope $\sim$ 0.13 nm/℃), as can be seen from Fig. 3.6(d). Thus, if the input pump wavelength is slightly offset from the desired value, it can still be phase-matched by simply tuning the waveguide temperature.

3.4 Conclusion

We have characterized the Zn-indiffused MgO:PPLN ridge waveguide having a cross-section of 10 µm$\times$10 µm through numerical mode analysis and SHG. The waveguide supports multi-mode at 775 nm and single mode at 1550 nm. The fundamental modes are well confined and near-circular and have high mode overlap $\sim$ 70.9%. The SHG results suggest that one waveguide (Waveguide 1) that has a phase-matching temperature of $\sim$ 41℃ has a SHG conversion efficiency of $\sim$ 30%/W, and another waveguide (Waveguide 2) that has a phase-matching temperature of 36.5℃ has a SHG conversion efficiency of $\sim$ 40.4%/W. The waveguide temperature plays a crucial role in the phase-matching process; the maximum efficiency of the waveguide can be harnessed only at phase-matching temperature. A particular pump wavelength is only phase-matched at a particular temperature, so if there is a slight offset in the pump wavelength, it can still be phase-matched by tuning the temperature. The efficient SHG generation in these waveguides from off-the-shelf optics and standard telecom lasers suggests that these can be used in frequency doubled-lasers, tissue imaging, ultra-short pulse characterization, and quantum light sources.

Chapter 4

Broadband generation of spectrally correlated photon pairs at telecom wavelength via joint spectral intensity measurements[1]

In this chapter, we experimentally demonstrate the broadband generation of spectrally correlated photon pairs at telecom wavelength in a fiber-integrated type-0

[1]

Parts of this chapter have been published in the followings
a) **Vikash Kumar Yadav**, Vivek Venkataraman, and Joyee Ghosh, "Broadband telecom photon pairs from a fiber-integrated PPLN ridge waveguide", **Optics Letters** 47(19), 5132-5135 (2022).
b) **Vikash Kumar Yadav**, Vivek Venkataraman, and Joyee Ghosh, "An efficient fiber-integrated broadband source of telecom photon-pairs", **Frontiers in Optics + Laser Science 2022 (FiO+LS)**, Technical Digest Series (Optica Publishing Group, 2022), paper JTu5A.38.

phase-matched Zn-indiffused MgO:PPLN ridge waveguide (Waveguide 1, phase-matching temperature $\sim$ 41℃). The photon pair emission spectrum measured using a narrow-bandpass digital tunable bandpass filter (FWHM bandwidth $\sim$ 1.2 nm) spans the telecom S, C, and L bands. The emission spectrum is centered around 1550 nm and has a FWHM bandwidth of $\sim$ 46 nm. The JSI and CAR measurements suggest that the photon pairs have very strong spectral and temporal correlations. Such fiber-integrated sources of telecom photons can be used in WDM-based QKD, quantum sensing and metrology, and information processing.

4.1 Introduction

Spectrally and temporally correlated telecom photon pairs are useful in various quantum applications, such as fiber-based secure key distribution [121], cryptography [11], information processing [77], and quantum metrology [37]. The chromatic dispersion, which can degrade the performance of these quantum applications, can also be mitigated by using spectrally correlated photon pairs [38, 78, 122]. The telecom photon pairs can be generated through various techniques, but SPDC is the most effective practice in terms of experimental ease and resources. However, the experimental complexity increases as we go from the generation to the actual application. For example, state-of-the-art quantum communication protocols involve a very complex experimental setup [123, 124], and this experimental complexity can be reduced with a guided-wave approach since it seems to be promising in yielding compact, stable, and efficient photon-pair source [77, 37].

Here, we demonstrate a fiber-integrated broadband source of spectrally/temporally correlated photon pairs at telecom wavelengths. The source utilizes a type-0 SPDC process in a commercially available Zn-indiffused MgO:PPLN ridge waveguide to

generate these telecom photons and it is aligned towards our guided-wave approach. It offers high nonlinearity (due to the strong confinement of optical modes) and efficient photon collection into single-mode fibers [125, 59]. We measure the generated broadband through a narrow-band digital tunable filter and experimentally characterize the spectral and temporal correlation of photon pairs. By demultiplexing the output emission spectrum, the same source can be used to serve multiple users in parallel for various applications such as quantum metrology, quantum information processing, and quantum communication.

4.2 Telecom photon pair generation via type-0 SPDC

SPDC is a widely used process to down-convert a pump photon into two photons, known as signal and idler. The correlation of these generated photons is vital for many quantum applications, as mentioned earlier. Here, for the down-conversion process, we use a Zn-indiffused MgO:PPLN ridge waveguide (Waveguide 1, which has a phase-matching temperature of ~ 41℃), which we have characterized via SHG earlier in Chapter 3.

4.2.1 Experimental setup

Figure 4.1 shows the experimental setup for telecom photon pair generation and detection where Zn-indiffused MgO:PPLN waveguide (Covesion: WGP-1550-40_18.5µm) is phase-matched for type-0 SPDC process: V (775-nm, pump) $\rightarrow$ V (1550-nm, signal) + V (1550-nm, idler), V denotes vertical polarization.

We use a continuous wave (CW) tunable laser at 775 nm (Toptica Photonics AG: DL PRO 780 FD2 S) to pump the waveguide, where the input power is controlled via a

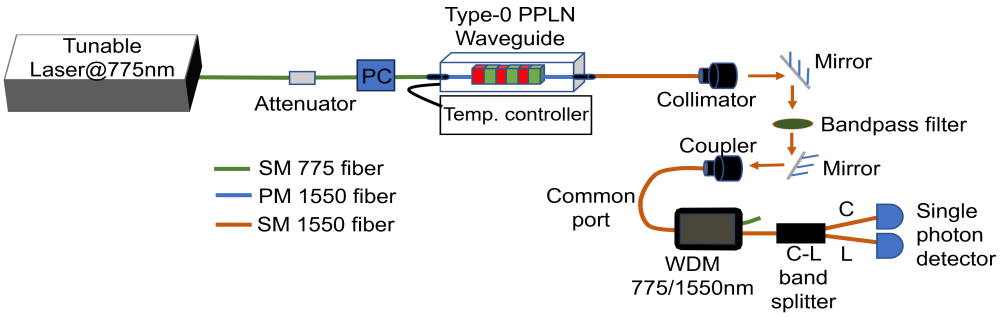

FIGURE 4.1: Experimental setup for telecom photon pair generation in Zn-indiffused MgO:PPLN ridge waveguide. PC: Fiber polarization controller, WDM: Wavelength-division-multiplexer. The waveguide has a phase-matching temperature of ~ 41℃.

manual variable optical attenuator (VOA) (OZ Optics: BB-700-11-780-5/125-S-50-3A3A-1-1-LL), and the polarization is controlled through a manual fiber polarization controller (PC) (Thorlabs). The output of the PPLN waveguide is passed through a bandpass filter (Thorlabs: FB1550-40), which has a FWHM bandwidth of ~ 40 nm at 1550 nm and insertion loss ≤ 1 dB, to suppress the residual pump and filter the telecom photons. Most of the pump is rejected in this process through this filter since it offers ~ 30 dB suppression at 775 nm. But to further ensure the complete filtering, a customized WDM for 775/1550 nm (which has a passband of 1550 ± 80 nm for the telecom port) (FONTCANADA: FWDM-7815-FA-Y) is used to separate the telecom photons from the residual pump. The WDM has an insertion loss of ~ 17 dB for the pump and ≤ 1 dB for telecom photons. Finally, the signal (short-wavelength) and idler (long-wavelength) photons are separated into two arms using a commercial C-L band splitter (C = 1500-1565 nm, L = 1565-1610 nm) (FONTCANADA: FWDM-5257-FA-R), and the photon count rate is measured with two single-photon avalanche photodetectors (SPAD) (Aurea Technology: SPD_OEM_NIR, detection efficiency 10%, dead time 5 µs, and dark counts < 1000 cps).

4.2.2 Result

We pump the waveguide with $\sim$ 40 µW power at $\sim$ 775 nm wavelength and measure the single photon count rate through the C- and L-arm of the C-L band splitter by varying the waveguide temperature. The dependence of the measured single photon count rate (raw) (in the C- and L-arm of the C-L band splitter) on waveguide temperature is shown in Fig.4.2. The dots and triangles represent the experimental data through the C and L-arm of the C-L band splitter, respectively. We note that the signal/idler photon generation rate is maximum at phase-matching temperature ($\sim$ 41℃), and it nearly follows a sinc^2 dependence on temperature. We note that the maximum photon count rate from C-arm and L-arm is not equal. The difference in the count rate is due to the fact that this C-L band splitter splits at 1565 nm, and the spectrum is degenerate and centered at 1550 nm, so maximum photons are going into the C-arm of the C-L band splitter, and fewer photons are going into the L-arm. Figure 4.3(a) shows the normalized count rate, where the dots and triangles are the experimental data of Fig. 4.2, and the solid blue line is the theoretically expected behavior. The experimental results are in agreement with the theoretical prediction. The slight asymmetry and larger sidelobes in our experimental data are a result of fabrication imperfections [119, 120].

Here, the theoretical curve is plotted using the photon generation rate (R) equation [126, 127]

$$R \approx A \int \omega_s \omega_i f(\omega_s) sinc^2(\frac{\Delta k L}{2}) d\omega_s \tag{4.1}$$

where A is a constant, and it depends on pump power, waveguide length, nonlinear coefficient, the spatial overlap of pump, signal, and idler modes, etc; $f(\omega_s)$ is the filter function (see Fig 4.3(b)), and Δk ($\Delta k = \frac{2\pi}{\lambda_p}(n_{eff})_p - \frac{2\pi}{\lambda_s}(n_{eff})_s - \frac{2\pi}{\lambda_i}(n_{eff})_i - \frac{2\pi}{\Lambda}$)

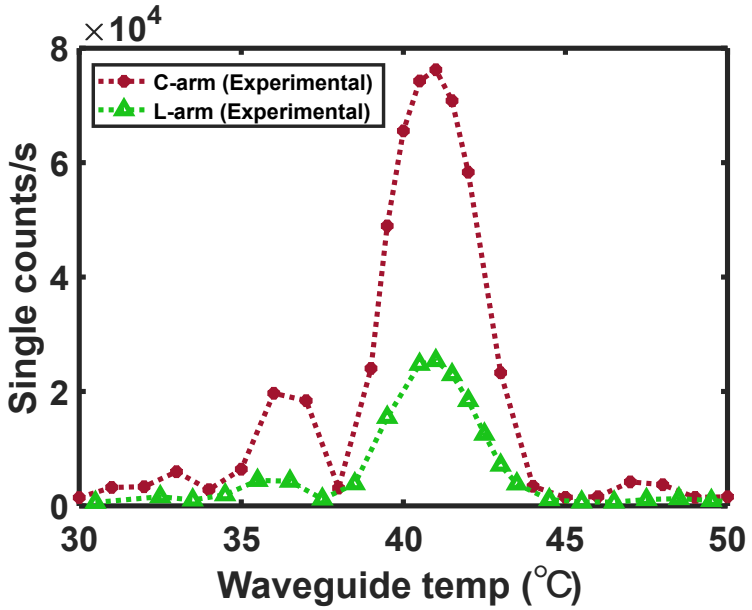

FIGURE 4.2: SPDC single-photon count rate dependence on waveguide temperature. The dots and triangles show the experimental result through the C-arm and L-arm of the C-L band splitter, respectively. The dotted lines connecting the data points are just a guide to the eye.

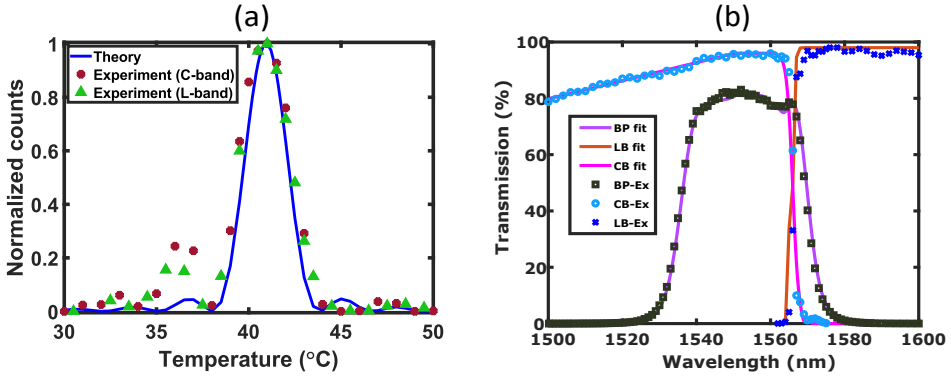

FIGURE 4.3: (a) Normalized single photon count rate with waveguide temperature. The solid line represents the theoretical result, and the dots and triangles show the experimental result of Fig. 4.2. (b) Transmission profile of the bandpass filter and C-L band splitter. BP-Ex: Experimentally observed bandpass filter transmission profile, LB-Ex: Experimentally observed L-band (arm) transmission profile, CB-Ex: Experimentally observed C-band (arm) transmission profile, BP fit: Bandpass filter transmission fitting function, LB fit: L-band (arm) transmission fitting function, CB fit: C-band (arm) transmission fitting function.

is the phase-mismatch in SPDC process. The n_{eff} at the pump, signal, and idler wavelengths are calculated through the COMSOL simulation of this waveguide.

For the C-band or C-arm photon generation rate, Eq. 4.1 can be considered as

$$R \approx A \int \frac{2\pi c}{\lambda_s}\frac{2\pi c}{\lambda_i} f(\lambda_s) sinc^2(\frac{\Delta k L}{2})\frac{2\pi c}{\lambda_s^2} d\lambda_s \tag{4.2}$$

where $\lambda_{s,i}$ are the signal and idler wavelengths respectively such that $\lambda_i = \frac{1}{\frac{1}{\lambda_p}-\frac{1}{\lambda_s}}$. $f(\lambda_s) = B(\lambda_s) \times C(\lambda_s)$, where $B(\lambda_s)$ is the bandpass filter (which is used for pump rejection) transmission function, and $C(\lambda_s)$ is the C-arm transmission function of the C-L band splitter.

$$B(\lambda_s) = \sum_{i=1,2...6} a_i e^{-\frac{(\lambda_s - b_i)^2}{c_i^2}} \tag{4.3}$$

where $a_{1,..6}$, $b_{1,..6}$, and $c_{1,..6}$ are constants such that $a_1 = 0.8141$, $a_2 = 0.128$, $a_3 = 0.1269$, $a_4 = 0.4823$, $a_5 = 0.4088$, $a_6 = 0.03364$, $b_1 = 1553$, $b_2 = 1545$, $b_3 = 1560$, $b_4 = 1567$, $b_5 = 1539$, $b_6 = 1562$, $c_1 = 13.39$, $c_2 = 4.106$, $c_3 = 3.622$, $c_4 = 4.271$, $c_5 = 4.856$, and $c_6 = 1.514$.

$$C(\lambda_s) = \begin{cases} 0.96 \times \frac{(0.0485\lambda_s - 60.739)}{14.45} & \text{for } \lambda_s = 1500 - 1550 \text{ nm} \\ 0.96 \times (lim_{t\to 0.8} \frac{1}{1+e^{\frac{(\lambda_s - 1566)}{t}}}) & \text{for } \lambda_s = 1550 - 1575 \text{ nm} \end{cases} \tag{4.4}$$

where the first term $0.96 \times \frac{(0.0485\lambda_s - 60.739)}{14.45}$ is used for the wavelength range 1500 nm - 1550 nm, and the second term $0.96 \times (lim_{t\to 0.8} \frac{1}{1+e^{\frac{(\lambda_s - 1566)}{t}}})$ is used for the wavelength range 1550 nm - 1575 nm. The multiplication factor of 0.96 is used to make the maximum value of the function equal to the experimentally observed value of the C-arm transmission. The C-arm photon generation at different waveguide temperatures is calculated using Eq. 4.2 by integrating from 1520 nm - 1575 nm, and then R values corresponding to different temperatures are plotted in Fig. 4.3(a).

For the L-band or L-arm photon generation rate, Eq. 4.1 can be considered as

$$R \approx A \int \frac{2\pi c}{\lambda_i} \frac{2\pi c}{\lambda_s} f(\lambda_i) sinc^2(\frac{\Delta k L}{2}) \frac{2\pi c}{\lambda_i^2} d\lambda_i \tag{4.5}$$

where $\lambda_{s,i}$ are the signal and idler wavelengths respectively such that $\lambda_s = \frac{1}{\frac{1}{\lambda_p} - \frac{1}{\lambda_i}}$. $f(\lambda_i) = B(\lambda_i) \times L(\lambda_i)$, where $B(\lambda_i)$ is the bandpass filter (which is used for pump rejection) transmission function, and $L(\lambda_i)$ is the L-arm transmission function of the C-L band splitter.

$$B(\lambda_i) = \sum_{j=1,2...6} a_j e^{-\frac{(\lambda_i - b_j)^2}{c_j^2}} \tag{4.6}$$

where $a_{1,..6}$, $b_{1,..6}$, and $c_{1,..6}$ are constants as described above.

$$L(\lambda_i) = \lim_{t \to 0.3} \frac{0.98}{1 + e^{\frac{-(\lambda_i - 1566)}{t}}} \tag{4.7}$$

The L-arm photon generation at different waveguide temperatures is calculated using Eq. 4.5 by integrating from 1562 nm - 1585 nm, and then R values corresponding to different temperatures are plotted in Fig. 4.3(a). The theoretical curve for the C-arm and L-arm photon rate is approximately the same, so here, only one theoretical curve is shown in Fig. 4.3(a)).

4.3 Bandwidth measurement of the photon-pair emission spectrum

4.3.1 Experimental setup

To measure the emission spectrum bandwidth (see Fig. 4.4), we use a CW laser at 775 nm to pump the Zn-indiffused MgO:PPLN ridge waveguide after controlling its input power and polarization. The PPLN waveguide is fixed at phase-matching temperature $\sim$ 41℃, and its output is passed through a WDM whose common port is connected to the waveguide and 1550-nm port is connected to a digital tunable narrow-bandpass filter (FWHM bandwidth $\sim$ 1.2 nm)(OZ Optics: TF-100-3A3A-1520/1570-9/125-S-60-1.2 or TF-100-3A3A-1570/1620-9/125-S-60-1.2). The 1550-nm port of WDM only allows a large telecom wavelength band (1550 $\pm$ 80 nm) to pass through with very low loss (see Appendix A), and the residual pump is transmitted to the 775-nm port. The output of the digital tunable filter is connected to a single photon detector, SPAD, which has a detection efficiency of 10%, dead time of 5 µs, and dark counts $<$ 1000 cps.

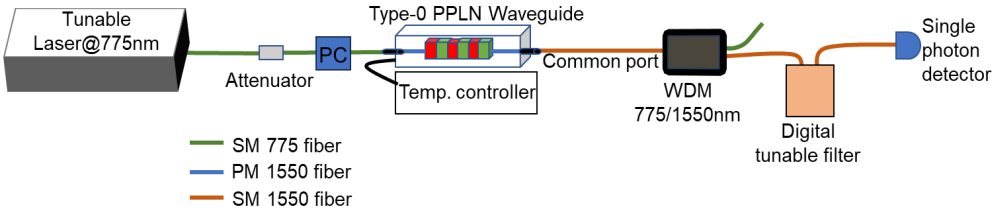

FIGURE 4.4: Experimental setup for photon pair emission spectrum measurement. PC: Polarization controller, WDM: Wavelength-division-multiplexer.

4.3.2 Result

We first pump the waveguide at $\sim$ 25 µW and then tune the wavelength of the digital tunable filter from 1520 nm to 1620 nm in a 2 nm step and measure the corresponding photon counts at each wavelength. We employ two tunable filters: the C-band filter, which can be tuned from 1520 nm to 1570 nm, and the L-band filter, which can be tuned from 1570 nm to 1620 nm. The detected raw single photon (signal/idler) counts at different tunable filter wavelengths are shown in Fig. 4.5(a). The blue line is just connecting the data points and does not signify extra information. Since the digital tunable filter has a wavelength-dependent loss (see inset of Fig. 4.5(b)), we weight the single counts with the corresponding loss of digital tunable filter and WDM (the details of insertion loss of digital tunable filter and WDM can be found in the Appendix A section) at each wavelength through the insertion loss ($I.L.$) formula $I.L. = 10log_{10}(P_{in}/P_{out})$ dB. The single photon counts at each wavelength before the digital tunable filter (DTF) are computed using the formula

$$\text{Photon counts before DTF} = (\text{Detected photon counts}) \times 10^{\frac{I.L.}{10}} \tag{4.8}$$

where the absolute value of insertion loss ($I.L.$ of DTF) is considered for each wavelength. Then, the photon counts before WDM (i.e. waveguide-generated photon counts) are computed as

$$\text{Generated photon counts} = (\text{Photon counts before DTF}) \times 10^{\frac{I.L.}{10}} \tag{4.9}$$

where now $I.L.$ of WDM is taken into account.

These generated or weighted photon counts at different tunable filter wavelengths

are shown in Fig. 4.5(b). Figure 4.5(c) shows the normalized experimental and theoretical single photon count rate at different wavelengths. The red stars correspond to the experimental values, and the solid blue line is the theoretically expected result. The experimental values are normalized using the formula

$$\frac{\text{Generated photon counts - Min. of generated photon counts}}{\text{Max. of generated photon counts - Min. of generated photon counts}}$$

The theoretical curve is plotted using $sinc^2(\frac{\Delta kL}{2})$, where Δk is calculated from the numerical simulation of the waveguide in COMSOL. The experimental results are in good agreement with the theory, and the emission spectrum bandwidth is $\sim$ 46 nm (centered at 1550 nm). The source generates the photon pairs in telecom S-, C-, and L-bands. Figure 4.5(d) shows the simulated signal/idler emission spectrum at different waveguide temperatures and indicates that the generated photon pairs have degenerate emission spectra below the phase-matching temperature and non-degenerate spectra (non-overlapping discrete bands) above phase-matching temperature. The shape and central wavelength of the signal/idler spectrum can be tuned over an extensive range by precisely controlling the waveguide temperature while keeping the pump wavelength constant.

4.4 Photon pair correlation characterization

4.4.1 Experimental setup

The experimental setup to measure the spectral and temporal correlation of photon pairs is shown in Fig. 4.6. The waveguide is pumped at 775 nm (using CW tunable laser) by setting it at phase-matching temperature for telecom photon pair generation, similar to what we did earlier in Fig. 4.4. The residual pump is rejected via a long pass filter (which transmits wavelengths $\geq$ 1518-nm)(OZ Optics:

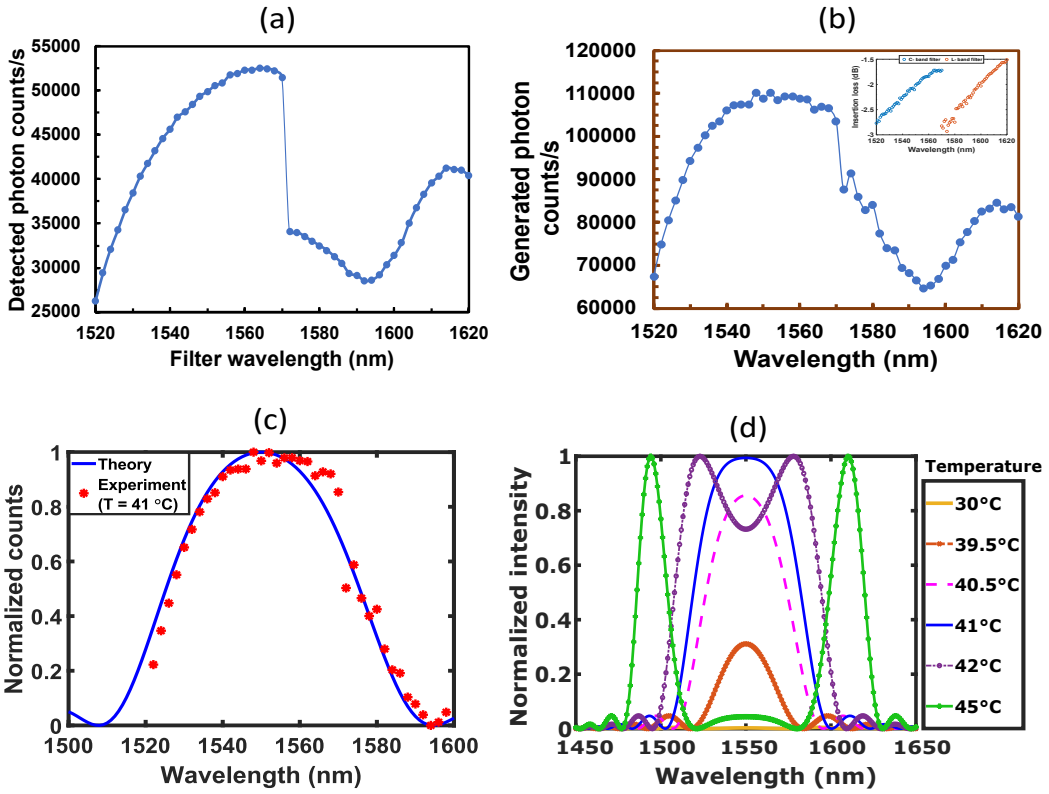

FIGURE 4.5: (a) Experimental raw (detected) single photon (signal/idler) counts versus tunable filter wavelength at phase-matching temperature (41°C). (b) Experimental weighted (generated) single photon counts considering the loss of digital tunable filter and WDM. The inset shows the insertion of the digital tunable filters (C-band = 1520 nm - 1570 nm, L-band = 1570 nm - 1620 nm; for details, see Appendix A). (c) Normalized single photon counts (experimental and theoretical) versus tunable filter wavelength. The red stars represent the experimental value, and the solid blue line is the theoretical $\text{sinc}^2(\Delta kL/2)$. (d) Numerically simulated telecom photon pair emission spectrum at different waveguide temperatures for a constant pump wavelength of 775 nm.

FF-21-1518:1650-9/125-S-50-3A3A-1-1-LP/REJ775) and WDM. The whole broadband of telecom photons is first splitted into two halves (C-arm and L-arm) at 1550 nm using a commercially available C-L band splitter (C-band/arm: 1500 nm - 1550 nm, L-band/arm: 1550 nm - 1620 nm) (Lightel Technologies USA: Model number 500-48947-02-1), and then a pair of digital tunable filter (DTF) is used in the C- and L-arm to select the desired signal and idler photon. Finally, these selected signal and idler photons are detected using a pair of single-photon detectors (detection efficiency 10%, dead time 5 µs, and dark counts $<$ 1000 cps), and a coincidence

between the two photons is checked in a coincidence counter (PicoQuant: PicoHarp 300).

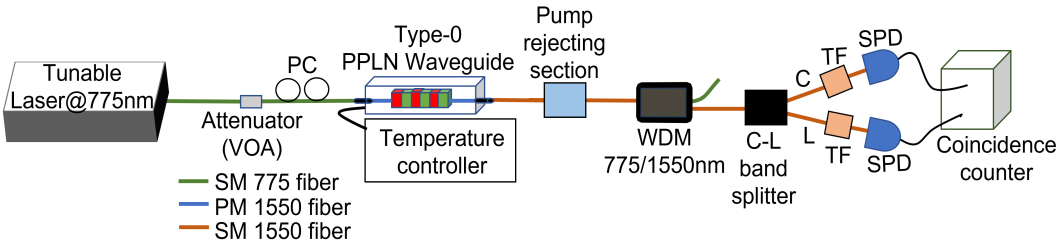

FIGURE 4.6: Experimental setup for photon pair spectral and temporal correlation measurement. PC: Polarization controller, SM: Single-mode, PM: Polarization maintaining, WDM: Wavelength-division multiplexer, TF: Digital tunable filter, SPD: Single-photon detector. The pump rejecting section is implemented using an in-line fiber-based long-pass filter (transmission wavelengths > 1518 nm).

4.4.2 Spectral correlation measurement

As discussed earlier in Chapter 2, JSI measurement unveils the spectral correlations between the photon pairs. To experimentally measure the JSI (see Fig. 4.7), we pump the waveguide with ~ 24.5 µW power at 775 nm and record the coincidence counts between the generated signal and idler wavelength pair (λ_s, λ_i) by stepping through the entire signal and idler wavelength range (1520 nm - 1580 nm), in discrete steps of 1 nm. First, for the signal wavelength 1520 nm, we fix the C-arm filter at 1520 nm and scan the whole idler wavelength from 1520 nm to 1580 nm by scanning the L-arm filter. Then, we increase the signal wavelength to 1521 nm by tuning the C-arm filter to 1521 nm and again scan the L-arm filter for idler wavelengths from 1520 nm to 1580 nm. We repeat this process till the signal wavelength 1550 nm. Since the C-arm has $\sim 0\%$ transmission for wavelength > 1550 nm and similarly L-arm has $\sim 0\%$ transmission for wavelength < 1550 nm (see Appendix A), we now fix the L-arm filter at 1551 nm for signal wavelength 1551 nm and scan the C-arm filter from 1520 nm - 1580 nm for idler wavelengths. We then increase the L-arm filter

wavelength by 1 nm and again scan the C-arm filter. We repeat this measurement till we reach the signal wavelength of 1580 nm. Here, the reported coincidence counts are measured only once and are not the average value. The measurement is performed only once due to the challenges associated with a lengthy measurement.

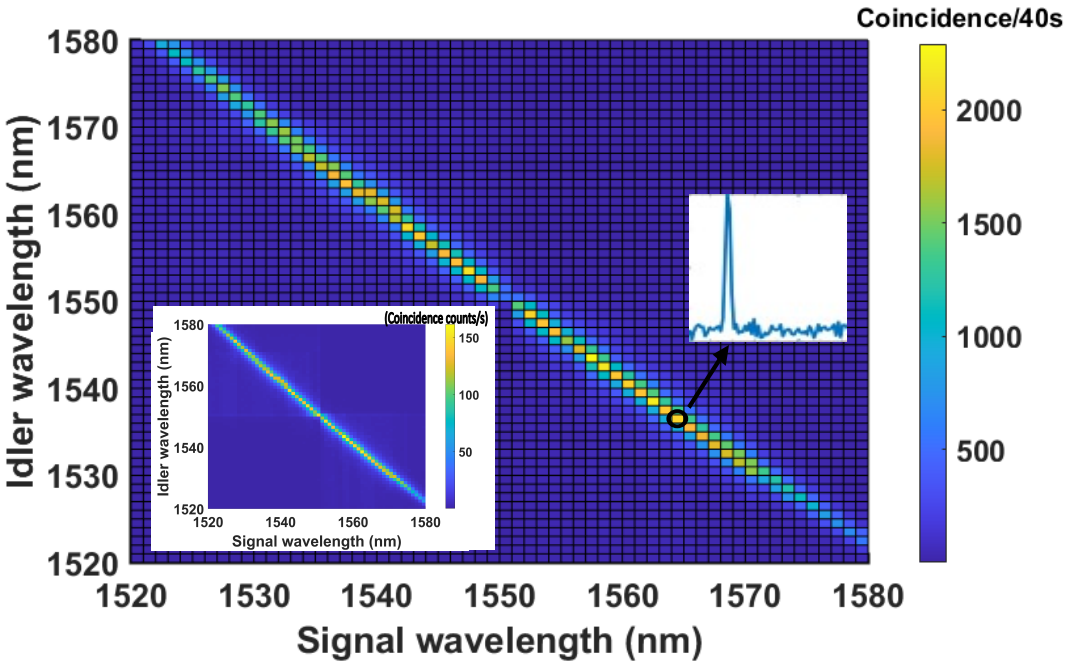

FIGURE 4.7: The joint spectral intensity (JSI) in a type-0 phase-matched Zn-indiffused MgO:PPLN ridge waveguide at phase-matching temperature. The coincidence counts are the raw measured counts without any background subtraction or weight. Inset shows the weighted coincidence counts, which include the losses of the digital tunable filter and C-L band splitter.

Alternatively, this can also be done with a 50:50 beam splitter instead of a C-L band splitter. In that case, we have to consider one port of the beam splitter as the signal arm and the other port as the idler arm, and we just have to fix the signal arm filter at one particular signal wavelength and scan the whole idler arm, by repeating this measurement for the whole signal wavelengths we can get the JSI spectrum. The only disadvantage is that the coincidence rate will be lower in this case because when both signal and idler pass through the same port of the beam splitter, they result in no coincidence. As it is clear from Fig. 4.7, the JSI spectrum is negatively inclined

($-45°$), which indicates a strong spectral correlation between the signal and idler photons. A signal photon at a particular wavelength is only correlated with one idler photon (a pair that satisfies the energy conservation condition). These correlated photons are essential for multi-user QKD and metrology to eliminate cross-talk and measurement errors [38, 46, 37]. The coincidence rate shown in Fig. 4.7 is the raw coincidence rate in 40-s of measurement time, and every point in the graph is obtained through the coincidence counter. The weighted coincidence rate is shown in the inset of Fig. 4.7, which includes the effect of digital tunable filter loss and C-L band splitter loss in both arms. Here, we have shown the formula/method used to find the weighted coincidence counts by considering three cases.

Case-1: For example, the raw coincidence count for the case when the signal wavelength is 1520 nm, and the idler is 1525 nm is 5 per 40-s. So, in this case, both photons are going through the C-arm of the C-L band splitter. But we assume that some photons of 1525 nm are also passing through the L-arm (that is why we are getting 5 coincidences by neglecting the accidental coincidence scenario), and they experience no loss by the L-arm of C-L band splitter (i.e. $\eta_L = 1$) except the loss of DTF (i.e. $\eta_{FL} = 0.55$). Photons of wavelength 1520 nm face loss due to C-arm transmission ($\eta_C = 0.94$) of C-L band splitter and DTF (i.e. $\eta_{FC} = 0.53$). Thus the expected or weighted coincidence counts will be $\frac{5}{\eta_C \times \eta_{FC} \times \eta_L \times \eta_{FL}} \sim 18$ per 40-s.

Case-2: For example, the raw coincidence count for the case when the signal wavelength is 1520 nm, and the idler is 1565 nm is 36 per 40-s. So, in this case, both photons are going through the different arms of the C-L band splitter. Photons of 1565 nm are passing through the L-arm, and they experience some loss by the L-arm of the C-L band splitter (i.e. $\eta_L = 0.98$) and DTF (i.e. $\eta_{FL} = 0.67$). Photons of wavelength 1520 nm face loss due to C-arm transmission ($\eta_C = 0.94$) of C-L band

splitter and DTF (i.e. $\eta_{FC} = 0.53$). Thus the expected or weighted coincidence counts will be $\frac{36}{\eta_C \times \eta_{FC} \times \eta_L \times \eta_{FL}} \sim 110$ per 40-s or ~ 3/s.

Case-3: For example, the raw coincidence count for the case when the signal wavelength is 1550 nm, and the idler is 1550 nm is 533 per 40-s. So, in this case, we assume both photons are going through different arms of the C-L band splitter (that is why we are getting 533 coincidences), and the 1550 nm photon of the L-arm will experience high loss by the L-arm of C-L band splitter (i.e. $\eta_L = 0.47$, this is the average value in wavelength range 1550±0.6 nm because the efficiency rapidly changes around 1550 nm, see the loss profile of C-L band splitter in Appendix A) and due to DTF (i.e. $\eta_{FL} = 0.63$). Photons of wavelength 1550 nm in the C-arm will face loss due to C-arm transmission ($\eta_C = 0.48$, this is the average value in wavelength range 1550±0.6 nm because the efficiency rapidly changes around 1550 nm, see the loss profile of C-L band splitter in Appendix A) of C-L band splitter and DTF (i.e. $\eta_{FC} = 0.63$). Thus the expected or weighted coincidence counts will be $\frac{533}{\eta_C \times \eta_{FC} \times \eta_L \times \eta_{FL}} \sim 5953$ per 40-s or ~ 149/s.

4.4.3 Temporal correlation measurement

As described earlier in Chapter 1, the temporal correlation of photon pairs can be measured by CAR. The CAR has to be high for a high-quality photon pair source because this ensures that the source mainly generates highly temporally correlated photon pairs with very few accidental counts. For this measurement, we fix the tunable filter of the C- and L-arm at three different wavelength pairs in Fig. 4.6 and check the effect of pump power on coincidence count rate and CAR. Figure 4.8(a) and (b) show detected or raw coincidence counts as a function of pump power and the weighted coincidence counts, respectively. The coincidence counts are weighted

by considering the losses of the C-L band splitter and digital tunable filter using the same method as described earlier in the "Spectral correlation measurement" section. For the wavelength combination 1546 nm - 1554 nm, the efficiencies of the C-arm and L-arm of the C-L band splitter are $\eta_C = 0.93$ and $\eta_L = 0.975$, respectively, whereas for the digital tunable filter (DTF) of C- and L-arm are $\eta_{FC} = 0.62$ and $\eta_{FL} = 0.64$, respectively. The weighted coincidence counts are calculated by the formula $\frac{\text{detected coincidence counts}}{\eta_C \times \eta_{FC} \times \eta_L \times \eta_{FL}}$ i.e. $\frac{\text{detected coincidence counts}}{0.93 \times 0.62 \times 0.975 \times 0.64}$. Similarly, for the wavelength combination 1543 nm - 1557 nm, the coincidences are estimated by considering $\eta_C = 0.932$, $\eta_{FC} = 0.6$, $\eta_L = 0.975$, and $\eta_{FL} = 0.65$; for the wavelength combination 1540 nm - 1560 nm, the coincidences are estimated by considering $\eta_C = 0.935$, $\eta_{FC} = 0.59$, $\eta_L = 0.975$, and $\eta_{FL} = 0.65$. The saturation in coincidence counts at high pump power in Fig. 4.8(a) is due to the detector's finite dead time. Figure 4.8(c) shows the variation of CAR with pump power. Here, the coincidence due to dark counts (approximately 1) is first subtracted from the true coincidences and accidental counts before calculating the CAR.

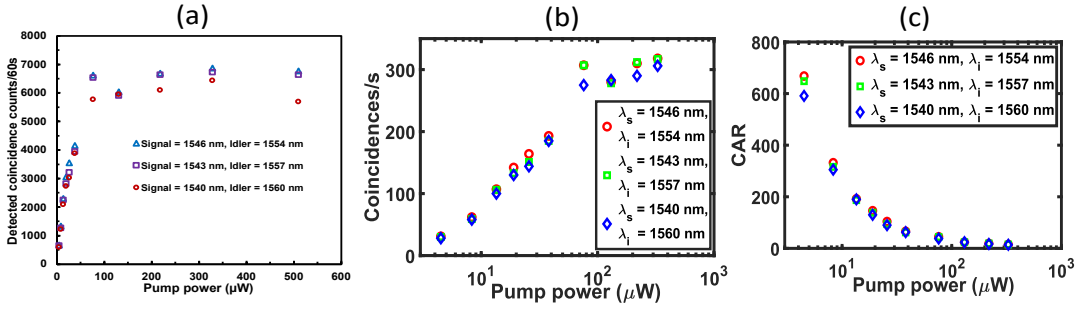

FIGURE 4.8: (a) Raw/detected coincidence count versus pump power for three different signal/idler channels. (b) Weighted coincidence counts/s (by considering the losses of C-L band splitter and digital tunable filer) versus pump power (c) Coincidence-to-accidental ratio (CAR) as a function of pump power for three different signal/idler channels.

We observe that the coincidence rate increases with an increase in pump power, but the CAR value reduces drastically, indicating a trade-off between the two parameters. This trade-off can be understood by the fact that an increase in pump

power increases the accidental counts along with the true coincidences since at high pump power, more pump photons can leak through the optical components, and the probability of multi-photon generation is also high, which results in false coincidences. Here, we measure a CAR value as high as ~ 668, indicating the high purity of our source. We also observed a CAR > 1300 when complete C- and L-bands were passed into the detectors, i.e., without tunable filters. This outlines that the fiber-integrated source has high temporal correlations between generated photon pairs, and the source has an internal spectral brightness of $\sim 2.5\times10^7$ pairs/s/mW/nm (estimated after factoring out all external losses and detector efficiencies as shown below, see Chapter 1 for more details).

Spectral brightness:

When we pump the waveguide at 25.5 µW and filter the generated telecom photons at 1550 nm via a digital tunable filter in both C- and L-arm:

Detected signal counts (N_s) at 1550 nm (from C-arm) = 13523 counts/s (cps).

$$N_{pair} = \frac{13523}{\eta_1 \times \eta_2^2 \times \eta_3 \times \eta_4 \times \eta_5 \times \eta_6^3}$$

where $\eta_1 = 0.73$, $\eta_2 = 0.93$, $\eta_3 = 0.48$, $\eta_4 = 0.63$, $\eta_5 = 0.1$, and $\eta_6 = 0.97$ are the efficiencies of WDM, long-pass filter, C-arm/band of C-L band splitter, digital tunable filter, single-photon detector, and fiber-mating sleeves/connector, respectively. We have used 2 long-pass filters and 3 fiber mating sleeves in the experiment, which is why we have η_2^2 and η_6^3 terms in the above expression.

$$N_{pair} = \frac{13523}{0.73\times0.93^2\times0.48\times0.63\times0.1\times0.97^3} \sim 776068 \text{ cps}$$

$$\text{Spectral brightness} = \frac{N_{\text{pair}}}{\text{pump power}\times\text{spectral bandwidth}} = \frac{776068}{25.5\mu\text{W}\times1.2\text{nm}}$$

Spectral brightness $\sim 2.5\times10^7$ pairs/s/mW/nm

4.5 Conclusion

In summary, we demonstrated a fiber-integrated broadband source of spectrally and temporally correlated photon pairs at telecom wavelengths based on Zn-indiffused MgO:PPLN ridge waveguide. The photon pair emission spectrum spans the telecom S-, C-, and L-bands, and it is centered around 1550 nm, having an FWHM bandwidth of $\sim$ 46 nm. The shape of the photon pair emission spectrum can be controlled by varying the temperature of the waveguide. Our proposed source has an estimated spectral brightness of 2.5×10^7 pairs/s/mW/nm, a negatively inclined JSI profile, and a high CAR value (> 650)(the large spectral and temporal correlations indicate its high quality). This source can be used in quantum metrology, WDM-based multi-user QKD, and information processing applications over existing fiber-optic networks.

Chapter 5

Fully fiber-integrated high brightness source of broadband polarization-entanglement at telecom wavelength[1]

In this chapter, we demonstrate an efficient all-fiber-coupled source of broadband polarization entanglement. We use a type-0 phase-matched Zn-indiffused MgO:PPLN ridge waveguide (Waveguide 2, which has a phase-matching temperature of 36.5℃)

[1]

Parts of this chapter have been published in the followings
a) **Vikash Kumar Yadav**, Vivek Venkataraman, and Joyee Ghosh, "High brightness fiber-coupled source of polarization-entangled photon-pairs spanning the telecom C- and L-bands", **Optics** & **Laser Technology**, 175, 110774 (2024).
b) **Vikash Kumar Yadav**, Vivek Venkataraman, and Joyee Ghosh, "An Efficient Source of Polarization-Entangled Photon-Pairs at Telecom Wavelength," in **Frontiers in Optics + Laser Science 2023 (FiO+LS)**, Technical Digest Series (Optica Publishing Group, 2023), paper JTu5A.19.
c) **Filed Indian Patent: Application number - 202311046589**.

in a fiber-based Sagnac loop to generate polarization-entangled photon pairs at telecom wavelength (spanning the C- and L-bands). We first measure the spectral width and temporal correlation of photon pairs generated in the Sagnac loop and then characterize the broadband entanglement by measuring the entanglement witness parameters such as interference visibility, CHSH inequality, fidelity, etc. Our source generates broadband (FWHM $\sim$ 52 nm) polarization entanglement with $>$ 89% fidelity and violates the CHSH inequality by $\sim$ 29 standard deviations ($S = 2.49 \pm 0.017$). The proposed source can be directly used in a WDM-based QKD network by demultiplexing the spectral width and in long-distance optical-fiber-based quantum communication.

5.1 Introduction

The quantum entanglement prepared using polarization degree of freedom of photon at telecom wavelength is favorable for ground-to-ground quantum communication, QKD [3, 128], quantum computing [11, 40, 129], quantum teleportation [21], etc. The existing optical fiber network has been used to send the polarization-entangled photons to vast distances ($>$ 190 km) [4] and in wavelength-multiplexed quantum key distribution (QKD) [46, 130] which demonstrates the feasibility of fiber-based quantum communication. Several methods based on SPDC and/or SFWM in the Sagnac loop configuration are reported in the literature for polarization-entangled photon pair generation at telecom wavelength. These methods include a silicon chip [23], polarization-maintaining dispersion-shifted fiber (PM-DSF) [131], and DSF at room temperature [132] in the Sagnac loop; a single fiber-pigtailed PPLN based on the cascaded process (SHG+SPDC) [133], and two fiber-pigtailed PPLN (each with dual poling periods) based on the cascaded process [134] in a Sagnac loop; a BBO

[135], PPKTP [136, 137], PPLN (fiber-pigtailed [37], free-space [138]), and two fiber-pigtailed PPLN (where SHG of one acts as the pump for SPDC in the other [139]) in the Sagnac loop. However, most of these methods are not very efficient and have experimental complexity. For example, the PM-DSF scheme requires cooling the fiber with liquid nitrogen in order to reduce Raman noise and eliminate polarization mode dispersion. In the cascaded process, the pump wavelength/frequency used is close to the generated signal/idler photon wavelength/frequency and thus makes its rejection difficult, and it also limits the practically achievable spectral brightness. The two nonlinear waveguides in one Sagnac loop scheme are more complicated and often require the same properties of both waveguides e.g. poling period, spectral bandwidth, brightness, etc, which is difficult to achieve in practice. Thus, most of these methods require many intensive technological resources and/or active stabilization for high-brightness generation, but a large-scale WDM-based QKD fiber network requires a simple fiber-integrated source that provides flexibility, compactness, and ease of deployment over the existing optical telecommunication infrastructure.

Here, we demonstrate a high-brightness fiber-integrated broadband source of polarization-entangled photons utilizing off-the-shelf telecom components and a type-0 phase-matched Zn-indiffused MgO-doped PPLN ridge waveguide in Sagnac loop configuration. We demonstrate the generation of broadband polarization-entangled photon pairs around the telecommunication wavelength of 1550 nm (spanning the C- and L-bands) and characterize the entanglement through various parameters such as two-photon interference/entanglement invariance, CHSH-Bell's inequality (S-parameter), and quantum state fidelity. The proposed source does not require any active stabilization system or compensation to operate, and it can be used in quantum cryptography [129], WDM-based quantum networks for secret key distribution [46, 130, 140], and quantum communication [3, 4].

5.2 Characterization of the broadband source in Sagnac loop

Here, we first characterize and measure the spectral bandwidth and photon pairs' temporal correlations, which are generated from a Zn-indiffused MgO:PPLN ridge waveguide (Waveguide 2, phase-matching temperature 36.5℃) in the Sagnac loop. Figure 5.1 shows the experimental setup for photon pair emission spectrum measurement and temporal correlation characterization where the PPLN waveguide (Waveguide 2) is type-0 phase-matched for degenerate down-conversion i.e. 775 nm (pump, V-pol) → 1550 nm (signal, V-pol) + 1550 nm (idler, V-pol), and has a phase-matching temperature of 36.5℃ (discussed earlier in Chapter 3). We pump the waveguide in the Sagnac loop configuration via a fiber polarization beam splitter (FPBS)(Thorlabs: PBC1550SM-APC) and CW tunable laser at 775 nm (Toptica Photonics AG: DL PRO 780 FD2 S), and the generated telecom photons are separated from the pump via WDM (FONTCANADA: FWDM-7815-FA-Y) and an in-line long pass filter (OZ Optics: FF-21-1518:1650-9/125-S-50-3A3A-1-1-LP/REJ775). The telecom photons are detected in two different scenarios to find the temporal correlation and to measure the emission spectrum.

5.2.1 Photon pair emission spectrum measurement

To measure the bandwidth of the photon pair emission spectrum, we connect a digital tunable filter (FWHM $\sim$ 1.2 nm)(OZ Optics: TF-100-3A3A-1520/1570(1570/1620)-9/125-S-60-1.2) and a single photon detector at the end of the long pass filter, as shown in Fig. 5.1. We operate the waveguide at a phase-matching temperature of 36.5℃ and pump with $\sim$ 4.5 µW power, and then tune the wavelength of the digital

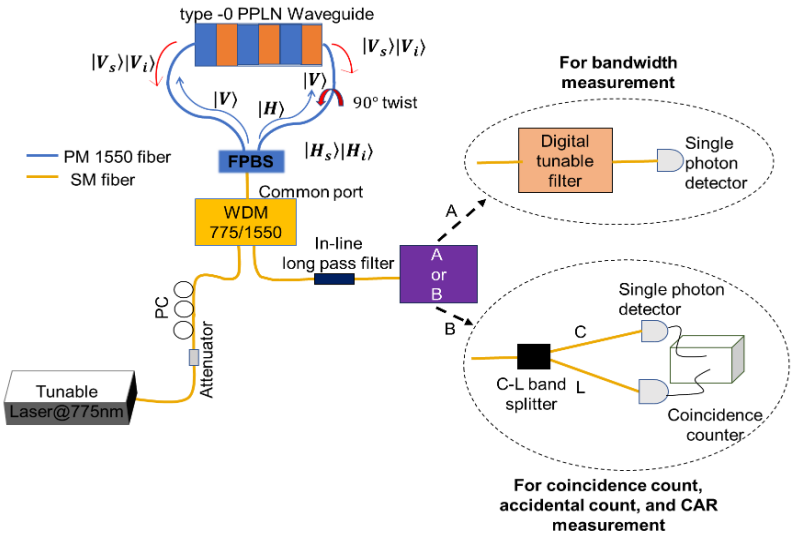

FIGURE 5.1: Experimental setup for photon pair emission spectrum measurement and temporal correlation characterization in Sagnac loop. PC: Polarization controller, WDM: Wavelength-division-multiplexer, FPBS: Fiber-polarization beam splitter.

tunable filter and measure the single photon rate through the APD detector (Aurea Technology SPD_OEM_NIR, detection efficiency 10%, dead time 5 µs, and dark counts $<$ 1000 cps). The detected raw single photon (signal/idler) count rate with tunable filter wavelength is shown in Fig. 5.2(a). The line is just connecting the data points and does not signify extra information. As we mentioned in the last chapter (Chapter 4), the digital tunable filter has a wavelength-dependent loss, so to find the generated photon count rate, we weigh the detected single counts with the corresponding loss of digital tunable filter (DTF) and WDM (see Appendix A for insertion loss details) at each wavelength through the insertion loss ($I.L.$) formula $I.L. = 10log_{10}(P_{in}/P_{out})$ dB. The single photon counts at each wavelength before the digital tunable filter (DTF) are estimated using the formula

$$\text{Photon counts before DTF} = (\text{Detected photon counts}) \times 10^{\frac{I.L.}{10}} \tag{5.1}$$

where the absolute value of insertion loss ($I.L.$ of DTF) is considered for each wavelength. Then, the photon counts before WDM (i.e. waveguide-generated photon counts) are computed as

$$\text{Generated photon counts} = (\text{Photon counts before DTF}) \times 10^{\frac{I.L.}{10}} \tag{5.2}$$

where now $I.L.$ of WDM is taken into account.

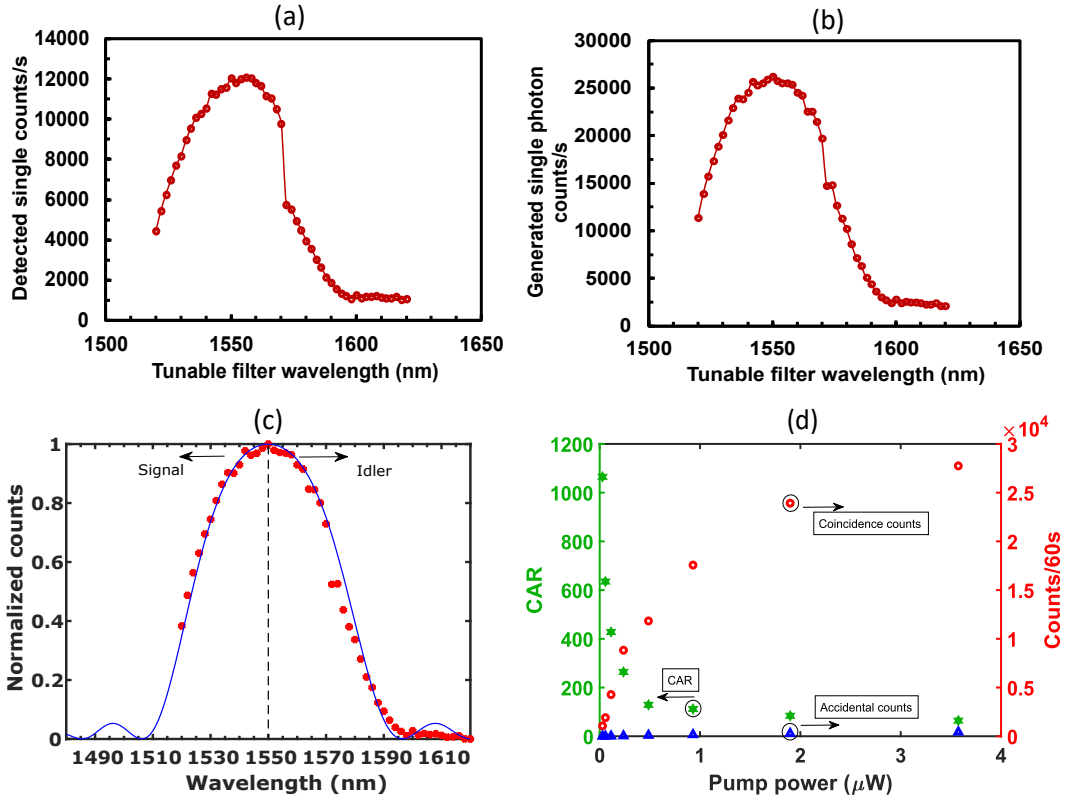

FIGURE 5.2: (a) Experimentally detected telecom single photon (signal/idler) counts at phase-matching temperature (36.5℃). (b) Experimental weighted (generated) single photon counts (obtained by considering the loss of digital tunable filter and WDM at different wavelengths). (c) Normalized single photon counts versus tunable filter wavelength. The red dots represent the experimental value, and the solid blue line is the theoretical $\text{sinc}^2(\Delta kL/2)$. (d) Effect of pump power on the coincidence-to-accidental ratio (CAR) (green), coincidence counts (red), and accidental counts (blue) when the waveguide is operated at phase-matching temperature in the Sagnac loop configuration.

The generated or weighted photon counts at different tunable filter wavelengths

are shown in Fig. 5.2(b). Figure 5.2(c) shows the normalized experimental and theoretical single photon counts at different wavelengths. The red dots correspond to the experimental values, and the solid blue line is the theoretically $sinc^2(\frac{\Delta kL}{2})$ result where Δk is calculated from the numerical simulation of the waveguide in COMSOL Multiphysics. The experimental values are normalized by the formula

$$\frac{\text{Generated single photon counts - Min. of generated single photon counts}}{\text{Max. of generated single photon counts - Min. of generated single photon counts}}$$

The experimentally measured counts fit well to the theoretical sinc^2 curve, and the spectrum has a FWHM bandwidth of $\sim$ 52 nm.

5.2.2 Photon pair temporal correlation characterization

The experimental setup to measure the temporal correlation between the generated photon pairs is shown in Fig. 5.1 where we connect a C-L band splitter (C $\sim$ 1520-1550 nm, L $\sim$ 1550-1580 nm) (Lightel Technologies USA: Model number 500-48947-02-1) and a pair of single photon detectors (Aurea Technology SPD_OEM_NIR), each with a detection efficiency of 10%, dead time of 5 µs, and dark counts $<$ 1000 cps, and a coincidence counter (PicoQuant: PicoHarp 300) (time-bin-width = 512 ps) just after the in-line long pass filter. We increase the pump power and measure the coincidence and accidental count rate between the C- and L-arm of the C-L band splitter. We find a maximum CAR of $\sim$ 1065 (see Fig. 5.2(d)), which indicates a high temporal correlation between photon pairs. It is estimated using the formula described in Chapter 1. It is evident from Fig. 5.2(d) that an increase in pump power leads to a high coincidence count rate and an accompanying rise in accidental counts as well due to multi-photon generation (which also affects the entanglement [141, 142]). For a waveguide input power of $\sim$ 3.6 µW, the coincidence and accidental

count rates are $\sim 2.7\times10^4$ counts/60s and 432 counts/60s, respectively, which results in a CAR value of 64.

The internal/generated spectral brightness of our source is $\sim 2\times10^8$ pairs/s/mW/nm (in Sagnac configuration), which is measured by employing a filter of ~ 1.2 nm bandwidth in both C- and L-arm (see Fig. 5.1) at 1547 nm and 1553 nm, respectively, and pumping the waveguide at ~ 3.98 µW power. To calculate the spectral brightness, we consider all the losses in the system from the point of generation of the photon pair to the detection and use similar methods as described earlier in Chapter 4. The total loss in our experimental setup breaks down as ~ 1.55 dB from waveguide to fiber coupling on each side, ~ 1.2 dB from Sagnac loop FPBS, ~ 1.4 dB from WDM, ~ 0.4 dB from long pass filter, ~ 0.5 dB from C-L band splitter (except at 1550 nm), ~ 2 dB from the filter, ~ 10 dB from the detector, and ~ 0.5 dB from the fiber-mating sleeves.

Spectral brightness:

Detected signal counts (N_s) at 1547 nm (from C-arm) = 12393 counts/s (cps).

$$N_{pair} = \frac{12393}{\eta_1^2\times\eta_2\times\eta_3\times\eta_4\times\eta_5\times\eta_6\times\eta_7\times\eta_8^5}$$

where $\eta_1 = 0.7$, $\eta_2 = 0.78$, $\eta_3 = 0.73$, $\eta_4 = 0.93$, $\eta_5 = 0.922$, $\eta_6 = 0.62$, $\eta_7 = 0.1$, and $\eta_8 = 0.97$ are the efficiencies of waveguide to fiber coupling on each side, Sagnac loop FPBS, WDM, long-pass filter, C-arm/band of C-L band splitter, digital tunable filter at 1547 nm, single-photon detector, and fiber-mating sleeve/connector, respectively. We have used 5 fiber mating sleeves in the experiment, and photons are generated from both sides of PPLN, which is why we have η_1^2 and η_8^5 terms in the above expression.

$$N_{pair} = \frac{12393}{0.7^2\times0.78\times0.73\times0.93\times0.922\times0.62\times0.1\times0.97^5} \sim 972968 \text{ cps}$$

$$\text{Spectral brightness} = \frac{N_{\text{pair}}}{\text{pump power}\times\text{spectral bandwidth}} = \frac{972968}{3.98\mu\text{W}\times 1.2\text{nm}}$$

Spectral brightness $\sim 2\times10^8$ pairs/s/mW/nm

5.3 Generation and characterization of broadband polarization entanglement

The experimental setup for broadband polarization-entangled photon-pair generation and detection is shown in Fig. 5.3. A CW tunable laser at 775 nm is used to bi-directionally pump a 4-cm long Zn-indiffused MgO:PPLN ridge waveguide (Waveguide 2, phase-matching temperature 36.5℃) placed in the Sagnac configuration (similar to what is shown in Fig. 5.1). The waveguide input pump power is controlled via an inline VOA (Thorlabs: VOA780-APC), and the polarization is through a fiber PC. The horizontal polarization (H-pol) arm of the input fiber-polarization beam splitter (FPBS, Thorlabs) is automatically rotated to vertical polarization (V-pol) via a 90° fiber twist before the waveguide facet. The 90° twist to change the polarization state of the light propagating through the fiber is given by the FPBS itself (no additional component is used) because when the two orthogonal polarization exits the PBS, both are coupled into two PM fibers along the slow axis and the fibers are terminated such that their key slot is along the slow axis. The two connectors are then connected to the waveguide in the same plane. This results as if a 90° twist is given in the H polarization arm of the FPBS. The input FPBS primarily works at the telecom wavelength but also has an acceptable performance at the pump wavelength except a very high insertion loss at pump. The two counter-propagating input pump waves are always V-pol within the waveguide and thus generate V-pol signal and idler photons. The signal and idler generated in the anti-clockwise direction remain V-pol, whereas those generated in the clockwise

direction are rotated to H-pol due to the same 90° fiber twist before recombining at the FPBS, resulting in a symmetric polarization-entangled state due to loss of "which-path" information. The input pump power is kept low enough so that the probability of signal/idler photons being simultaneously generated in both clockwise and anti-clockwise directions is negligible. The probability amplitude of the $|H_s\rangle |H_i\rangle$ and $|V_s\rangle |V_i\rangle$ contribution is equalized by precisely controlling the input pump polarization which results in the maximum entangled Bell-state generation $|\Phi^+\rangle = \frac{1}{\sqrt{2}}(|H_s\rangle |H_i\rangle + |V_s\rangle |V_i\rangle)$.

The residual pump in the output 1550-nm port of the WDM is rejected using an inline long-pass filter (LPF) with a cut-off wavelength of 1518 nm and insertion loss of < 1 dB. The signal (shorter-wavelength) and idler (longer-wavelength) photons of the generated broadband spectrum are separated into the C- ($\sim$ 1520-1550 nm) and L- ($\sim$ 1550-1580 nm) arms, respectively, of a telecom C-L band splitter. Finally, we characterize the quantum entanglement between signal and idler photons by projecting them into different polarization bases with the help of a fiber-coupled polarization analyzer unit in each arm (a combination of a quarter-wave plate (QWP), a half-wave plate (HWP), and an FPBS (OZ Optics: FOBS-12N-111-9/125-SPP-1550-PBS-60-3A3A3A-1-1)). Signal and idler photons are detected through two single-photon avalanche photodetectors (SPAD) (Aurea Technology, detection efficiency 10%, dead time 5 µs, and dark counts < 1000 cps) and the coincidence events between the two detectors are recorded in a time-tagger unit (PicoQuant: PicoHarp 300) with a time-bin-width of 512 ps.

Zero degree angle calibration of waveplates:

The single-mode fibers do not preserve the polarization of the signal and idler photons when they propagate from the source to the detector, so it is necessary to first calibrate the 0° angle of all the waveplates before proceeding to the entanglement

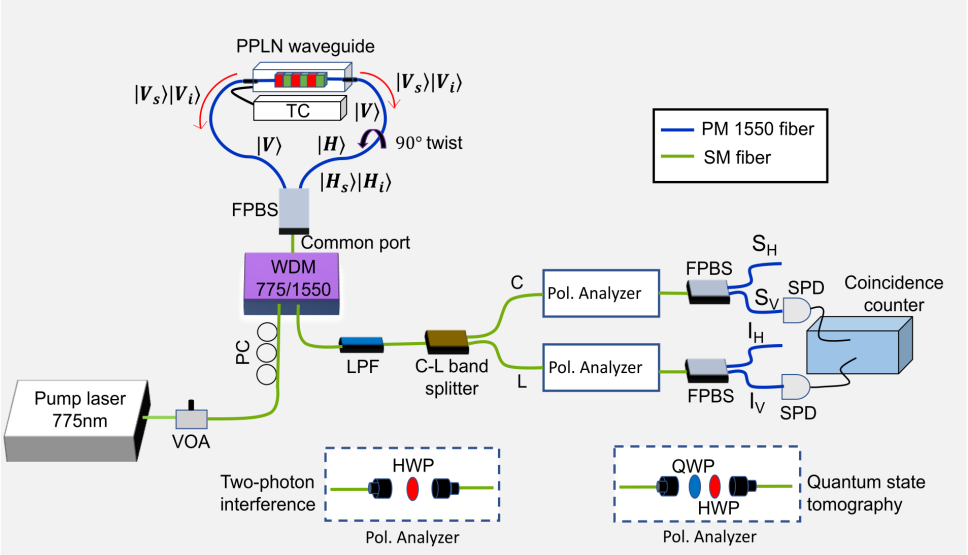

FIGURE 5.3: Experimental setup for broadband polarization-entangled photon pair generation and detection at telecom wavelength. VOA: Variable optical attenuator, PC: Polarization controller, WDM: Wavelength division multiplexer, FPBS: Fiber polarization beam splitter, TC: Temperature controller, LPF: Long-pass filter, Pol. Analyzer: Polarization analyzer, SPD: Single photon detector, $S_H/|H_s\rangle$: Signal with horizontal polarization, $S_V/|V_s\rangle$: Signal with vertical polarization, $I_H/|H_i\rangle$: Idler with horizontal polarization, $I_V/|V_i\rangle$: Idler with vertical polarization. The blue and green lines show the polarization maintaining and single mode fiber, respectively.

generation and measurement. Two methods can be used for the angle calibration, which are discussed below.

Method 1: We disconnect the pump laser (775 nm), FPBS from PPLN waveguide, single photon detector, and coincidence counter from the experimental setup and connect a telecom laser (EXFO: T100S-HP-CL) and power meter (Thorlabs) as shown in Fig. 5.4. We first use a polarimeter (Thorlabs: PAX1000IR2/M, F240APC-C) at point 'A' and optimize the polarization of the telecom laser through a polarization controller to make it vertically polarized (V-pol), then we disconnect the polarimeter by taking care that we do not disturb the single mode fiber much. We then connect this V-pol classical light to the FPBS port as shown in Fig. 5.4 and observe the power via a power meter through the output FPBS ports by varying the waveplate angles.

To find the 0° angle of HWPs, we put a HWP in both C- and L-arm and try to find the sinusoidal pattern in power through the FPBS port 1 and port 2 by varying the HWP angles. To maximize the visibility of this classical fringe pattern, we can control the polarization of the C- and L-arms before the 'Pol. Analyzer' unit by employing a set of polarization controllers (PC). With this process and optimization of PC, we find the best possible fringes as shown in Fig. 5.4 (top two images), and from that, we can find the 0° angle of HWP. For example, here in C-arm HWP, 65° acts as 0°, and in L-arm HWP, 30° acts as 0°.

Then, to find the 0° angle of QWPs, we first put the HWPs at 0° (i.e. 65° and 30°) in both C- and L-arm and then put the QWP such that QWPs precede HWPs. We vary the QWP angle and find the sinusoidal pattern in power through the FPBS port 1 and port 2 as shown in Fig. 5.4 (bottom two images). From this fringe pattern, we can find the 0° angle of QWPs; for example, here in C-arm QWP 43° acts as 0°, and in L-arm QWP 21° acts as 0°.

Thus, through this method, we can optimize the detection side of the experimental setup and can also find the 0° of the waveplates. If our SM fiber of the classical telecom source got disturbed while connecting to the PM fiber of the FPBS at point 'A' (i.e. the input to FPBS is not V-pol), then we might notice some offset in the 0° angles during the entanglement measurement even after calibrating through the telecom laser source. This offset can be accounted for during the quantum two-photon interference measurement.

Method 2: We use the experimental setup of Fig. 5.3 with only HWP in the 'Pol. Analyzer' unit and optimize the input pump polarization for entanglement generation such that we do not see much variation in the single counts with the rotation of HWP angles. We then observe the two-photon interference pattern (see next section for details) between the C- and L-arm FPBS port 2. The fringe visibility

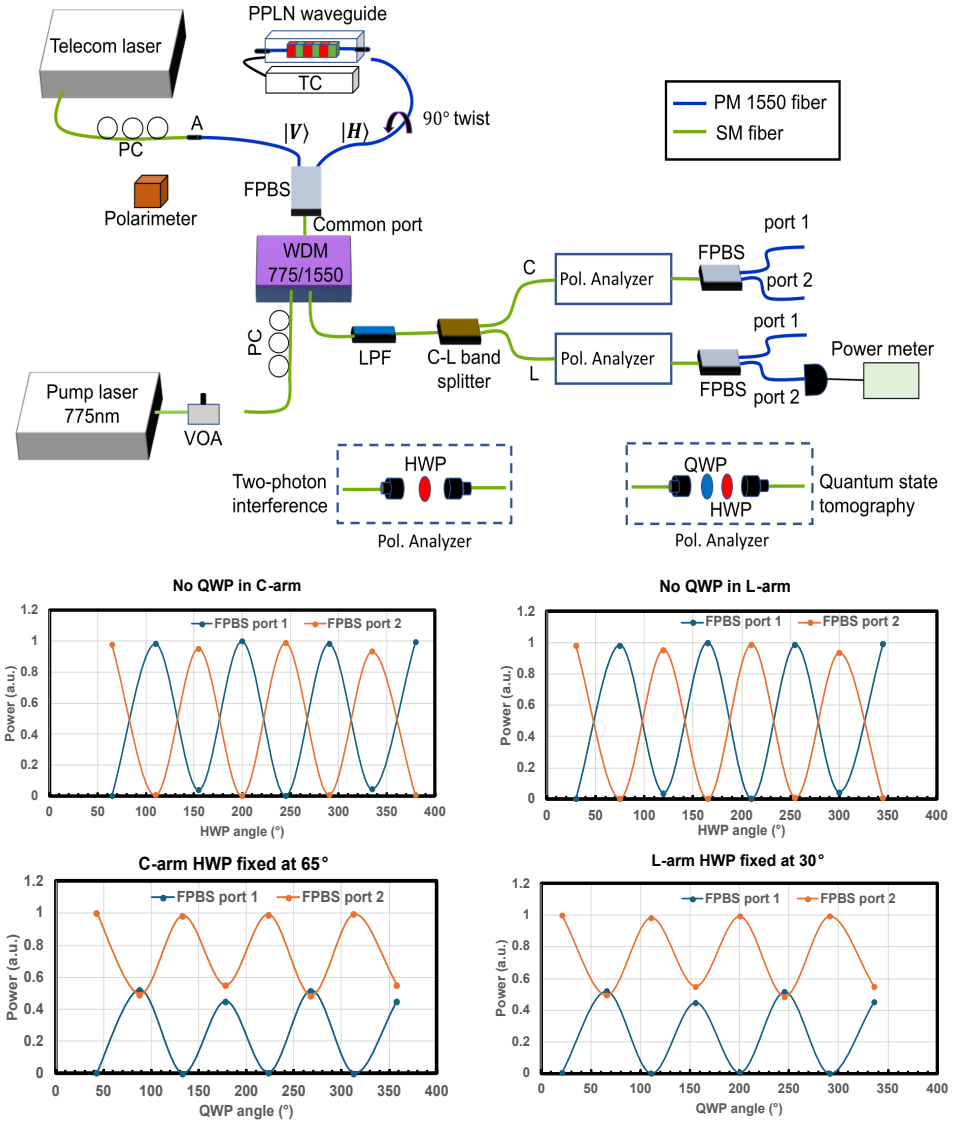

FIGURE 5.4: Experimental setup for the 0° angle calibration of HWPs and QWPs before entanglement generation characterization.

can be enhanced by controlling the polarization of the C- and L-arm before the 'Pol. Analyzer' unit (by employing a set of PC in the C- and L-arm). By observing the two-photon interference fringes, we can find the 0° degree of HWP. For example, we measure the two-photon interference spectra shown in Fig. 5.5, which indicates that in C-arm HWP 65° acts as 0°, and in L-arm HWP 30° acts as 0°.

Then, to calibrate the 0° angle of QWP, we use a combination of waveplates such that QWPs precede HWPs (which are now positioned at 0° i.e. at 65° and 30°) in both

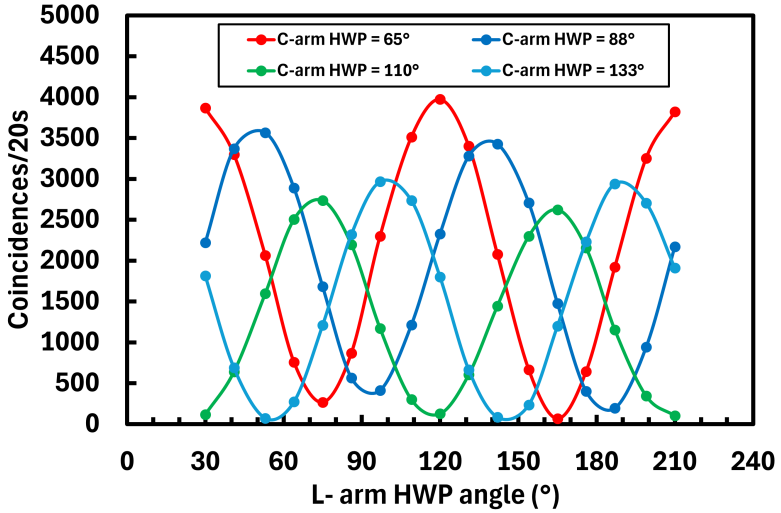

FIGURE 5.5: Two-photon interference fringes with C-arm FPBS port 2 and L-arm FPBS port 2.

C- and L-arms and vary the QWP angles to achieve the same maximum coincidence rate of two-photon interference and similar sinusoidal behavior except that now the minimum coincidences are only approximately the half of the maximum coincidence value. It is noticed that if we can first get the two-photon interference with good visibility, then we can easily calibrate the 0° of the QWP without adjusting the polarization of the C- and L-arms before the 'Pol. Analyzer' unit.

5.3.1 Two-photon interference and polarization correlations

For this measurement, we only use a HWP and FPBS, see Fig. 5.3, where the 'Pol. Analyzer' unit consists only of a HWP between a collimator and coupler in free space. The coupling efficiency of Pol. Analyzer unit is $\sim$ 85% in both arms, and the insertion loss of the output FPBS is $<$ 0.5 dB at 1550 nm. The signal (C-arm) photon is projected onto one of the four horizontal (H), vertical (V), diagonal (D), or anti-diagonal (A) polarization via a HWP followed by a FPBS, and then the

coincidences are measured for different HWP angles (placed before the FPBS) in the idler (L-arm) arm.

We first attenuate the waveguide input pump power to $\sim$ 1-µW through a VOA to avoid the multi-photon generation and then use a fiber PC to adjust the pump polarization for maximally entangled Bell-state ($|\Phi^+\rangle$) generation. The generated polarization-entangled broadband spectrum (shown in Fig. 5.2(a)) is split into two halves about 1550-nm using the C-L band splitter, such that all the signal photon travels in C-arm and all idler photon travels in the L-arm. $S_{H,V}$ and $I_{H,V}$ represent the signal and idler photon counts at the two output ports of their respective FPBS. The observed two-photon interference (between the signal and idler photons) in terms of coincidence counts is shown in Fig. 5.6 (after taking care of the 0° offset of C-and L-arm HWPs) where the dots correspond to the experimental coincidences, and the solid line is the sinusoidal fit. We note that when signal and idler photons are projected on the linear (H, V, D, and A) basis, the maximum coincidence occurs when both photons have the same polarization. For example, when the signal photon is projected onto V-pol, the maximum coincidences occur corresponding to the case when the idler is also V-pol, and if the signal is projected onto D-polarization, maximum coincidences occur when the idler is also in D-polarization, and this is consistent with the $|\Phi^+\rangle$ Bell state. The raw fringe visibilities in the H-V (0°, 45°) and D-A (22.5°, 67.5°) basis are 88.9%, 93.9% and 86.6%, 98.7%, respectively.

We further check the two-photon interference between four different polarization combinations (S_H and I_H; S_V and I_V; S_H and I_V; S_V and I_H) of the signal and idler photons using a single pair of SPADs. The observed coincidences for two fixed angles (0° and 45°) of signal (C-arm) arm HWP are shown in Fig 5.7(a) and 5.7(b), respectively. The co-polarized (symmetric) mode (S_H and I_H, S_V and I_V), as well as the orthogonal (anti-symmetric) polarization mode (S_H and I_V, S_V and I_H), are

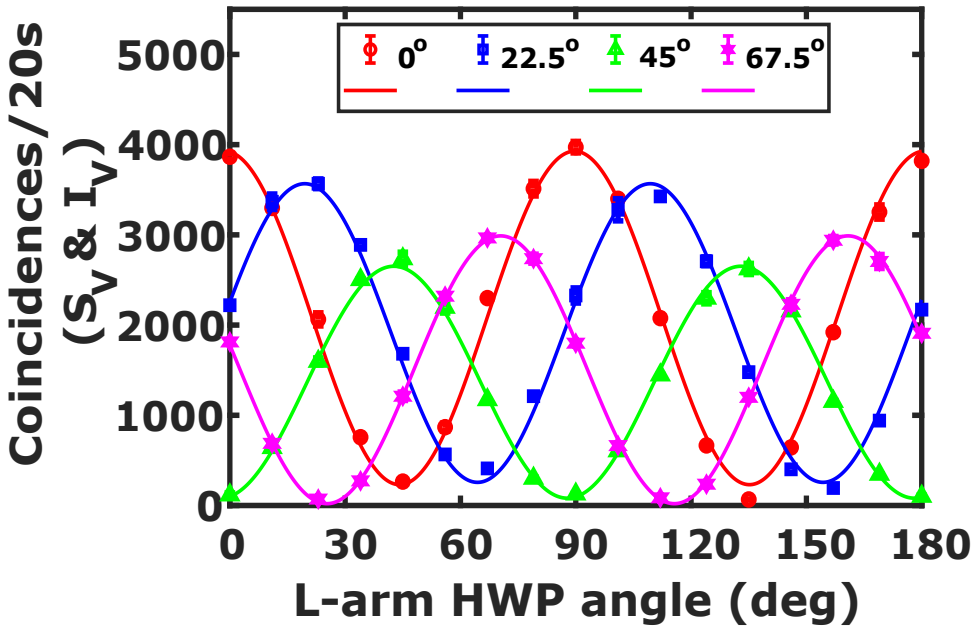

FIGURE 5.6: Two-photon interference when signal and idler photons are projected onto the H-V and D-A polarization basis.

always in phase. The sinusoidal fringes of the symmetric polarization modes are out of phase from the sinusoidal fringes of the anti-symmetric polarization modes, and the rotation of the polarization analysis basis (via C-arm HWP) shifts the sinusoidal fringes but preserves the phase difference among the individual fringes. This further confirms the generation of polarization-entangled photon pairs [37].

The visibility of red, blue, green, and magenta sinusoidal fringes in Fig. 5.7(a) are 97.1%, 88.9%, 98.8%, and 90.1% respectively, whereas in Fig. 5.7(b) are 93.2%, 94.1%, 92.9%, and 90.1%, respectively. The unequal coincidence rate in different polarization bases (in two-photon interference) is mainly due to slightly imperfect input pump polarization, which gives a bit unequal generation of $|H_s\rangle |H_i\rangle$ and $|V_s\rangle |V_i\rangle$ contribution, ultimately limiting the maximum entangled Bell state generation. Another reason is the asymmetric response of the HWPs and FPBS, which are used to characterize two-photon interference. This difference in the amplitudes

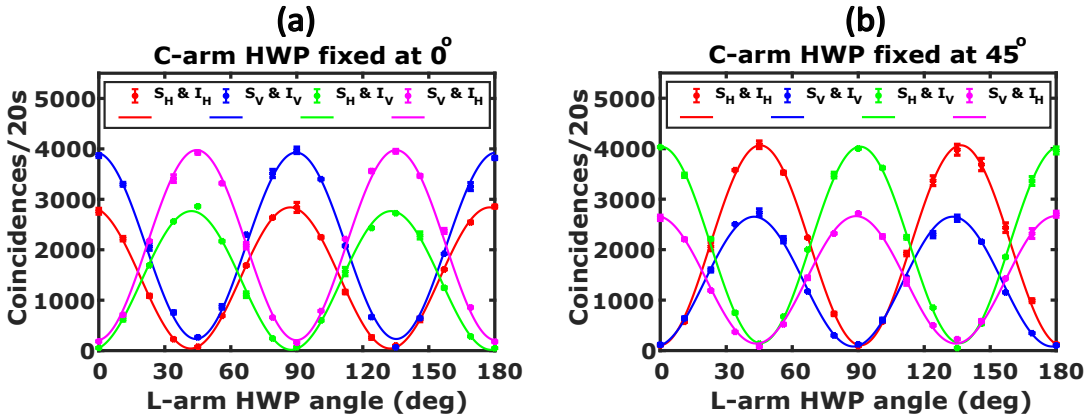

FIGURE 5.7: Two-photon interference corresponding to the four possible combinations of signal and idler polarization. The HWP angle in the signal (C-arm) arm is fixed at (a) 0° (b) 45°, and the HWP angle of the idler (L-arm) arm is varied.

of the coincidence counts (in different polarization bases) can be minimized by using symmetrical optics and by precisely controlling the input pump polarization.

5.3.2 Violation of CHSH-Bell's inequality

To analyze the violation of CHSH-Bell's inequality, we utilize the interference fringe pattern of Fig. 5.6, where we use a pair of HWP and FPBS to project the photon in linear polarization basis. The maximum violation is observed at HWP angles $\theta_a = 0°$, $\theta_a^{'} = 22.5°$, $\theta_b = 11.25°$, and $\theta_b^{'} = 33.75°$ (see Chapter 1 for details). We calculate the correlation coefficients and, hence, the S-parameter through the formula given in Chapter 1 and obtained the CHSH-Bell parameter S = 2.49 ± 0.017 [143, 144] (from our raw coincidence data). The explanation of the S-parameter calculation from two-photon interference measurement is given below in Fig. 5.8, where we use the coincidence data of Fig. 5.6.

This shows that the generated state violates the CHSH inequality by ∼ 29 standard deviations. Thus, it is evident that the broadband SPDC spectrum consists mainly

Data of two photon interference

L-arm HWP	C-arm HWP at 0°			C-arm HWP at 23°			C-arm HWP at 45°			C-arm HWP at 68°		
angle (°)	Coincidence counts		Average	Coincidence counts		Average	Coincidence counts		Average	Coincidence counts		Average
0	3892	3839	3865.5	2218	2221	2219.5	99	133	116	1795	1831	1813
11	3324	3272	3298	3428	3306	3367	623	658	640.5	685	692	688.5
23	2114	2011	2062.5	3527	3604	3565.5	1569	1624	1596.5	74	68	71
34	778	735	756.5	2861	2916	2888.5	2508	2498	2503	273	272	272.5
45	277	253	265	1701	1663	1682	2682	2786	2734	1177	1244	1210.5
56	836	900	868	579	552	565.5	2240	2151	2195.5	2318	2321	2319.5
67	2307	2291	2299	423	399	411	1170	1173	1171.5	2969	2962	2965.5
79	3454	3569	3511.5	1226	1198	1212	310	291	300.5	2771	2700	2735.5
90	4017	3927	3972	2387	2268	2327.5	120	132	126	1791	1807	1799

$$E(0,11.25) = \frac{(3298 + 2196 - 641 - 868)}{(3298 + 2196 + 641 + 868)} = 0.5690 \qquad E(0,33.75) = \frac{(757 + 301 - 2503 - 3512)}{(757 + 301 + 2503 + 3512)} = -0.7008$$

$$E(22.5,11.25) = \frac{(3367 + 2320 - 689 - 566)}{(3367 + 2320 + 689 + 566)} = 0.6384 \qquad E(22.5,33.75) = \frac{(2889 + 2736 - 273 - 1212)}{(2889 + 2736 + 273 + 1212)} = 0.5823$$

$$S = 0.5690 - (-0.7008) + 0.6384 + 0.5823 = 2.4905$$

Total number of involved photon pairs N_p = Coincidence counts when both the C and L- arms HWP were at 0° + (Total coincidence without the polarizers) Coincidence counts when both the C and L-arm HWP were at 45°

$$N_p = 3866+2734 = 6600$$

$$\text{Standard deviation in S} = \sqrt{\frac{2}{N_p}} = \sqrt{\frac{2}{6600}} = 0.017$$

$$\mathbf{S = 2.49 \pm 0.017}$$

FIGURE 5.8: Calculation of S-parameter from two-photon interference fringe measurement.

of polarization-entangled photon pairs, and the above results highlight the quality of the source.

5.3.3 Quantum state tomography

To further check the generated Bell state, we perform quantum state tomography (QST) by projecting photons in different polarization bases (as discussed in Chapter 1) and calculate the state fidelity. We repeat each measurement twice and then take the average value of coincidence counts in the calculation of the density matrix (see TABLE 5.1). The real and imaginary parts of the reconstructed density matrix are shown in Fig. 5.9. From the experimental data, we find that $|\Phi^+\rangle = \frac{1}{\sqrt{2}}(|H_s\rangle\,|H_i\rangle + |V_s\rangle\,|V_i\rangle)$ Bell-state is generated with a raw fidelity of $\sim 89.4\%$ (without background subtraction) and raw concurrence ~ 0.83.

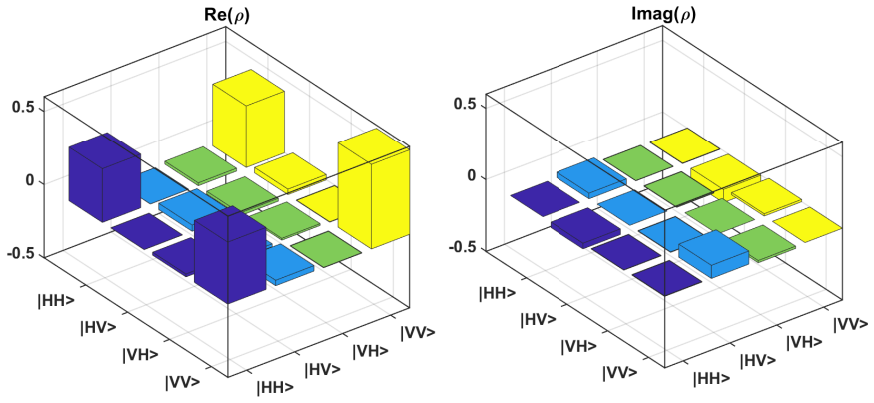

FIGURE 5.9: The reconstructed density matrix of the broadband polarization entangled state. The source generates a $|\Phi^+\rangle = \frac{1}{\sqrt{2}}(|H_s\rangle|H_i\rangle + |V_s\rangle|V_i\rangle)$ Bell state with $\sim 89.4\%$ raw fidelity. Various colors in the density matrix are intended for presentation purposes only and do not reflect any information.

TABLE 5.1: Quantum state tomography (QST) measurement [73]. CD/20s denotes the measured average coincidence counts per 20-s. The density matrix is reconstructed using the coincidence data through MATLAB code and/or an online open tomography interface (which uses Python code), which are available at https://research.physics.illinois.edu/QI/Photonics/tomography/.

	Signal path (C-arm)		Idler path (L-arm)		
S.N.	QWP angle	HWP angle	QWP angle	HWP angle	CD/20s
1	0° (i.e. 43°)	45° (i.e. 110°)	0° (i.e. 21°)	45° (i.e. 75°)	2379
2	0° (i.e. 43°)	45° (i.e. 110°)	0° (i.e. 21°)	0° (i.e. 30°)	271
3	0° (i.e. 43°)	0° (i.e. 65°)	0° (i.e. 21°)	0° (i.e. 30°)	3527
4	0° (i.e. 43°)	0° (i.e. 65°)	0° (i.e. 21°)	45° (i.e. 75°)	69
5	0° (i.e. 43°)	22.5° (i.e. 87.5°)	0° (i.e. 21°)	45° (i.e. 75°)	1105
6	0° (i.e. 43°)	22.5° (i.e. 87.5°)	0° (i.e. 21°)	0° (i.e. 30°)	2635
7	45° (i.e. 88°)	22.5° (i.e. 87.5°)	0° (i.e. 21°)	0° (i.e. 30°)	2198
8	45° (i.e. 88°)	22.5° (i.e. 87.5°)	0° (i.e. 21°)	45° (i.e. 75°)	1375
9	45° (i.e. 88°)	22.5° (i.e. 87.5°)	0° (i.e. 21°)	22.5° (i.e. 52.5°)	1757
10	45° (i.e. 88°)	22.5° (i.e. 87.5°)	45° (i.e. 66°)	22.5° (i.e. 52.5°)	3286
11	0° (i.e. 43°)	22.5° (i.e. 87.5°)	45° (i.e. 66°)	22.5° (i.e. 52.5°)	1819
12	0° (i.e. 43°)	45° (i.e. 110°)	45° (i.e. 66°)	22.5° (i.e. 52.5°)	1283
13	0° (i.e. 43°)	0° (i.e. 65°)	45° (i.e. 66°)	22.5° (i.e. 52.5°)	1812
14	0° (i.e. 43°)	0° (i.e. 65°)	90° (i.e. 111°)	22.5° (i.e. 52.5°)	2177
15	0° (i.e. 43°)	45° (i.e. 110°)	90° (i.e. 111°)	22.5° (i.e. 52.5°)	1592
16	0° (i.e. 43°)	22.5° (i.e. 87.5°)	90° (i.e. 111°)	22.5° (i.e. 52.5°)	3714

TABLE 5.2: Comparison of our source with the relevant state-of-the-art polarization entangled photon-pair sources which employ the Sagnac loop configuration to generate $|\Phi^+\rangle$ Bell state. Q.E. = Quantum efficiency, CDW = Coincidence detection window, NR = Not reported, p = pump wavelength, s = signal wavelength, i = idler wavelength, APD = Avalanche photodetector, SNSPD = Superconducting nanowire single-photon detector.

Source	Spectral bandwidth	Entanglement shown in	Fidelity	S-parameter	Detectors used (Q.E., CDW)
Ref. [131]	NR	Single channel p = 1552.52 nm s = 1555.75 nm i = 1549.32 nm	85%	NR	APD (22.6%, NR)
Ref. [37]	40 nm	Single channel p = 780 nm s = 1574 nm i = 1546 nm	NR	2.5 ± 0.02	APD (20%, 81ps)
Ref. [138]	NR	Single channel p = 780 nm s = 1541 nm i = 1580 nm	96.3%	NR	SNSPD (NR)
Ref. [133]	60 nm	Single channel p = 1553 nm s = NR, i = NR	98.1%	2.76 ± 0.03	SNSPD (80%, 500 ps)
Ref. [139]	58 nm	*Single channel p = 1560 nm s ∼ 1555.2 nm i ∼ 1564.8 nm	95%	NR	SNSPD (74%, 120 ps)
Ref. [132]	3.2 nm	Single channel p = 1550.1 nm s ∼ 1552.25 nm i ∼ 1547.72 nm	NR	2.50 ± 0.12	APD (20%, 0.4 ns)
Ref. [23]	NR	Single channel p = 1550.18 nm s ∼ 1557.36 nm i ∼ 1542.94 nm	93.4%	2.66 ± 0.10	APD (20%, NR)
This work	52 nm	Broadband p = 775 nm s ∼ 1520-1550 nm i ∼ 1550-1580 nm	89.4%	2.49 ± 0.017	APD (10%, 512 ps)
		Single channel p = 774.894 nm s = 1549.318 nm i = 1550.117 nm	96.5%	2.55 ± 0.024	APD (20%, 512 ps)

Note: *Channel bandwidth is 8 nm (i.e. s ∼ 1548.2-1556.2 nm, i ∼ 1560.8-1568.8 nm).

After the subtraction of background counts ($\sim$ 10, which were measured when no phase-matching condition was satisfied, i.e., at T = 28℃), the fidelity and concurrence increase to 89.84% and 0.83, respectively. If we consider the minimum coincidences of two-photon interference fringes as background counts (in our case, it is $\sim$ 67 in red fringes, see Fig. 5.5), then after background count subtraction, the fidelity and concurrence increase to 92.29% and 0.88, respectively. The high value of fidelity and concurrence obtained using standard room temperature APDs without any filtering/channelization indicates the generation of broadband polarization-entanglement. We also checked the quantum entanglement in one channel pair by inserting a digital tunable filter (FHWM $\sim$ 1-nm) at wavelength 1547-nm and 1553-nm in the C-and L-arm, respectively. We observed a raw fidelity of $\sim$ 84.4% and raw concurrence $\sim$ 0.82. The low value of fidelity and concurrence could be due to the high insertion loss of the digital tunable filter and imperfect optimization of the experimental setup. We note that the fidelity increases to $\sim$ 96.5% when we filter out a single DWDM channel pair (ITU-34 & ITU-35) for entanglement characterization with slightly more efficient APDs (20%, ID Qube NIR, ID Quantique) and well optimized experimental setup, which is comparable to the state-of-the-art (see TABLE 5.2).

5.4 Conclusion

In conclusion, we demonstrate a fiber-coupled broadband source of polarization-entangled photon pairs based on type-0 SPDC in a Zn-indiffused MgO:PPLN ridge waveguide in the Sagnac loop. The generated spectrum is centered at 1550 nm with FWHM bandwidth $\sim$ 52 nm, and it spans the telecom C- and L-bands. The estimated spectral brightness of our source is $\sim 2\times10^{8}$ pairs/s/mW/nm, and it has

a high temporal correlation (CAR $>$ 1000) among the photon pairs. We analyze the entanglement by splitting the output spectrum into two halves (signal in one half and idler in the other half) at 1550 nm. The interference fringe visibility in the H-V basis is $>$ 88.9% and in the D-A basis is $>$ 86.6%. The observed S-parameter (2.49 ± 0.017) shows the violation of CHSH-Bell's inequality by 29 standard deviations, and the generated $|\Phi^+\rangle$ Bell state has a raw fidelity of $\sim$ 89.4% and concurrence $\sim$ 0.83. Our results indicate that the source mainly generates polarization-entangled photon pairs over the entire broadband spectrum. This simple fiber-integrated broadband source can be directly used in a WDM-based QKD, optical fiber-based long-distance quantum communication, and in the study of fundamental aspects of quantum optics where entangled photons are required.

Chapter 6

Multi-user telecom source of tunable polarization-entanglement for long-distance (∼ 100 km) WDM-based quantum communication network[1]

In this chapter, we demonstrate an efficient and easily deployable fully fiber-integrated multi-user source of polarization-entangled photon pairs in the low-loss telecom

[1]

Parts of this chapter have been published in the followings
a) **Vikash Kumar Yadav**, Vivek Venkataraman, and Joyee Ghosh, "Telecom source of tunable polarization-entanglement distribution up to 100-km for multi-user QKD over metro-area fiber-optic networks", **APL Quantum** 2 (1), (2025).
b) **Vikash Kumar Yadav**, Vivek Venkataraman, and Joyee Ghosh, "Entanglement distribution over 100 km via a fully fiber-integrated telecom quantum source," (**Abstract accepted for oral presentation in APS March Meeting 2025**).
c) **Granted Indian Patent: Application number - 202411033430, Patent number - 560305**.

C-band. The source is based on type-0 SPDC in a fiber-coupled Zn-indiffused MgO:PPLN ridge waveguide (Waveguide 2) in the Sagnac configuration, and it can be easily tuned to generate the $|\Phi^+\rangle$ or $|\Phi^-\rangle$ Bell state in 14 channel pairs of the standard ITU-DWDM grid (100 GHz channel spacing) around 1550 nm with raw fidelity $\geq 89\%$ (maximum value $\geq 94\%$) and raw concurrence ≥ 0.8 (max value ~ 0.88). The observed S-parameter is $> 2.56 \pm 0.04$ in all 14-channel pairs for both Bell states. We show the source's suitability for long-distance entanglement transmission by successfully transferring the entangled photons up to 100 km via single-mode fiber spools and study the impact of polarization mode dispersion (PMD) on entanglement distribution. Our highly flexible source generates 14 independent polarization entangled Bell states, which can be used by 14 user pairs simultaneously for quantum communication or key distribution. The proposed source can support up to 40 user pairs for simultaneous communication, and it can be easily deployed into the current metropolitan-scale fiber-optic telecom network to form a complete quantum communication network.

6.1 Introduction

A multi-user polarization-entangled photon pair source is the key to a realistic quantum communication network, which enables widespread connectivity for multi-user communication and secret key distribution [46, 47, 51]. Despite the advancement in quantum light sources based on SPDC [37, 35, 63] and SFWM [145, 146], the development of large-scale fully-connected quantum networks has remained elusive, because of the applicability of such sources mostly being limited to a single pair of communicating parties/users. In this regard, a multi-channel WDM source of

polarization-entangled photons could be a promising candidate for the establishment of a large metropolitan-scale quantum communication network. The advancement in quantum technologies, such as QKD between remote users [4, 43, 147] and long-distance entanglement transmission [4, 148, 149, 150], has already shown the potential for the practical realization of metro-area and/or long-haul networks and quantum internet. Different sources of multi-user communication have been proposed in the last two decades, for example, the source proposed by Ref. [51] potentially supports 44 channel pairs but entanglement was characterized in only 6 channel pairs, Ref. [130] has shown polarization entanglement in 4 channel pairs, Ref. [151] has shown hyper-entanglement in 5 channel pairs, and Ref. [46, 47] have shown the entanglement in 6 and 8 channel pairs, respectively. The above sources utilize a periodically poled lithium niobate (PPLN) crystal/waveguide and generate a $|\Phi^+\rangle$ Bell state at telecom wavelength. Ref. [51] used a 1-mm long PPLN in the Sagnac loop in a free space setup, Ref. [130] used two 30-mm long PPLN crystals arranged in a Mach-Zehnder interferometer in a free space setup, Ref. [151] used a 38-mm long PPLN in Sagnac loop in a fiber-integrated setup, and Ref. [46, 47] used a 40-mm and 50-mm long PPLN crystal in Sagnac loop in free space, respectively. Recently, more than 15 ITU channel pairs have been exploited to create a complete quantum network [48, 49]. The above-mentioned sources are either limited to a few users and/or are not compact/fiber-integrated and difficult to deploy outside the laboratory and/or have not completely characterized entanglement in all channel pairs, which is important for their applicability in long-distance (metropolitan-scale) networks. The scalability of a WDM-based quantum communication network requires an easily deployable, compact, efficient, and stable broadband/multi-channel source of polarization-entangled photons with high spectral brightness and strong spectral correlations (negligible cross-talk between corresponding channel pairs).

Here, we demonstrate and characterize a fully fiber-integrated multi-channel source of polarization-entangled photons in the low-loss telecom C-band based on a 40-mm long Zn-indiffused MgO:PPLN ridge waveguide. We employ the waveguide in Sagnac configuration to generate broadband tunable polarization-entanglement around 1550 nm and demultiplex the spectrum using a standard arrayed waveguide grating (AWG) into the DWDM ITU grid with 100-GHz channel spacing. The source can generate either $|\Phi^+\rangle$ or $|\Phi^-\rangle$ Bell state, and it can be easily tuned from one to another with the help of a fiber polarization controller. We characterize various entanglement witness parameters such as two-photon interference, violation of CHSH-Bell's inequality, concurrence, and quantum state fidelity in 14 ITU wavelength channel pairs. We also check the source's suitability for long-distance entanglement transmission and study the effect of PMD on entanglement distribution. We show the generation of 14 independent bipartite polarization-entangled Bell states in a fully fiber-integrated source and report the best performance metrics to date with standard room temperature single-photon avalanche detectors (APDs). The source can be utilized by 14 different user pairs simultaneously for long-distance quantum communication or key distribution.

6.2 ITU channel pair correlations and emission spectrum utilization

6.2.1 Characterization of AWG channel pair cross-talk

In the last chapter (Chapter 5), we discussed the broadband source of polarization-entangled photons at telecom wavelengths, which has the potential for WDM QKD.

Here, we want to extend that design into a multi-user source for quantum communication applications by demultiplexing the spectrum width through arrayed wave grating (AWG) (which is a single-stage filter that deploys planar waveguide technology [152]). But to implement a source for a multi-user QKD network, the knowledge of channel pair cross-talk or channel pair correlation is essential because a high cross-talk between the adjacent channel pairs deteriorates the entanglement shared by the user pairs and leads to the bit error rate in key distribution. Therefore here we first find characterize the correlations between the channel pairs. We use a passive athermal 32-channel AWG (AC Photonics: AAWGG132DC50H241011) in the experiment, which has 32 channels (Gaussian shape transmission) from C50 (1537.407 nm) to C19 (1562.23 nm) in the ITU grid (see Fig. 6.1). The nominal channel spacing of the AWG is 100 GHz, and the insertion loss in each channel is $<$ 3 dB.

Figure 6.2(a) shows the experimental setup to characterize the AWG channel pair correlation in Sagnac configuration. We note from Fig. 6.1 that the AWG channel pairs are not symmetrical at about 1550 nm, so simply demultiplexing of the spectral width through AWG will not suffice because our source generates broadband-entanglement degenerate at 1550 nm (when we use a pump wavelength of 775 nm). This may lead to channel pair cross-talk. Here, we first tune the pump wavelength to 775.06 nm such that we have degenerate emission at 1550.12 nm (which corresponds to AWG ITU channel C34). We pump the waveguide with $\sim$ 40 µW near the phase-matching temp 37.5℃ and measure the coincidences between different channel pairs as shown in Fig. 6.2(b). We note that channel C35 is correlated with channel C33, and channel C36 is correlated with channel C32, and so on. However, the correlation weakens as we move from channel pair C42-C26 onward to C49-C19, and the cross-talk also increases.

Test Data Sheet

1×32 Channel Gaussian 100GHz Athermal AWG Demux module										
P/N:		AAWGG132DC50H241011				S/N:		180523000904		
Test Temperature: -5.0 °C										
CHNo	Center WL	WL Diff	1dB BW	FWHM	IL(dB)	Ripple(dB)	PDL(dB)	Adj CT	Total CT	Non Adj CT
C50	1537.407	-0.011	0.156	0.239	2.738	0.435	0.193	-35.455	-31.889	-37.984
C49	1538.187	-0.012	0.162	0.341	2.620	0.444	0.155	-35.800	-34.761	-40.345
C48	1538.967	-0.009	0.157	0.340	2.579	0.547	0.198	-32.039	-32.557	-38.854
C47	1539.774	-0.018	0.148	0.339	2.524	0.494	0.197	-33.075	-30.911	-38.531
C46	1540.567	0.007	0.137	0.312	2.797	0.609	0.152	-31.660	-33.315	-38.775
C45	1541.342	0.005	0.168	0.254	2.520	0.604	0.176	-33.585	-34.585	-38.378
C44	1542.151	0.001	0.122	0.252	2.773	0.607	0.152	-34.429	-31.686	-36.084
C43	1542.926	-0.001	0.166	0.266	2.625	0.496	0.168	-33.281	-32.779	-36.602
C42	1543.731	-0.009	0.161	0.320	2.755	0.545	0.164	-33.770	-34.303	-40.273
C41	1544.536	-0.014	0.127	0.344	2.539	0.624	0.171	-35.262	-33.757	-40.993
C40	1545.340	-0.001	0.129	0.285	2.679	0.619	0.175	-31.758	-30.052	-40.291
C39	1546.125	-0.003	0.132	0.212	2.603	0.584	0.154	-34.683	-30.851	-39.100
C38	1546.921	-0.006	0.141	0.350	2.515	0.434	0.199	-31.288	-31.423	-39.356
C37	1547.721	-0.018	0.169	0.275	2.647	0.521	0.186	-33.654	-31.482	-36.551
C36	1548.533	0.006	0.163	0.316	2.696	0.513	0.180	-35.143	-32.613	-40.621
C35	1549.318	-0.012	0.160	0.300	2.699	0.496	0.185	-34.812	-31.473	-39.921
C34	1550.117	-0.001	0.157	0.227	2.685	0.523	0.172	-32.737	-34.888	-39.872
C33	1550.912	-0.014	0.159	0.236	2.668	0.443	0.197	-32.768	-34.040	-37.459
C32	1551.724	0.008	0.165	0.213	2.734	0.590	0.191	-31.281	-32.444	-38.827
C31	1552.538	0.006	0.167	0.216	2.771	0.566	0.152	-34.079	-30.595	-36.379
C30	1553.322	0.002	0.168	0.279	2.515	0.573	0.151	-35.978	-30.412	-40.702
C29	1554.135	-0.009	0.131	0.324	2.540	0.596	0.191	-33.895	-33.075	-38.033
C28	1554.944	-0.013	0.148	0.345	2.544	0.555	0.198	-35.979	-31.598	-38.676
C27	1555.759	0.002	0.150	0.277	2.562	0.564	0.178	-31.143	-30.901	-39.856
C26	1556.560	-0.019	0.144	0.345	2.515	0.564	0.159	-32.140	-31.815	-40.522
C25	1557.370	-0.018	0.126	0.217	2.777	0.461	0.196	-32.013	-30.028	-40.659
C24	1558.178	0.000	0.148	0.313	2.660	0.571	0.161	-34.399	-33.645	-40.873
C23	1558.997	-0.009	0.142	0.339	2.748	0.618	0.183	-32.538	-30.532	-36.279
C22	1559.803	-0.013	0.139	0.240	2.588	0.496	0.197	-31.799	-31.692	-40.938
C21	1560.619	-0.015	0.156	0.267	2.588	0.515	0.182	-33.885	-31.354	-39.053
C20	1561.420	-0.004	0.170	0.235	2.544	0.594	0.156	-33.788	-30.562	-37.040
C19	1562.230	0.008	0.169	0.333	2.665	0.445	0.191	-33.590	-31.106	-38.774
Tester:VS002						Date:2023-2-25				

FIGURE 6.1: Specification sheet of the arrayed-waveguide grating (AWG).

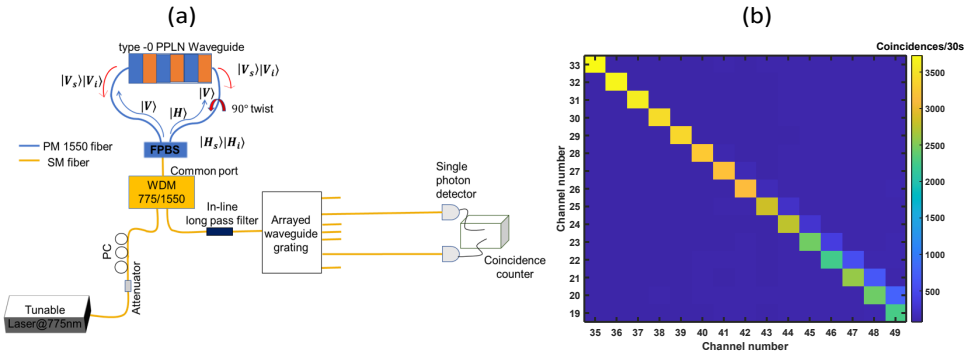

FIGURE 6.2: (a) Experimental setup to characterize the channel pair correlation of AWG in Sagnac configuration. (b) Measured coincidence spectrum between different channel pairs at a pump wavelength of 775.06 nm.

To find the optimum parameters for the best channel pair correlation, we perform a single-pass SPDC and tune both the wavelength and waveguide temperature. The experimental setup is as follows: A CW pump laser, VOA, fiber polarization controller, type-0 Zn-indiffused MgO:PPLN waveguide, WDM at 775/1550 nm, long-pass filter (LPF), AWG, SPAD, and a coincidence counter. We set the pump laser at $\sim$ 774.8938 nm and operate the waveguide (pump power $\sim$ 39 µW) at a temperature of 34.33^{o}C for this single-pass down-conversion process which generates the degenerate spectrum at nearly the central wavelength of channel C35 (1549.318 nm) and C34 (1550.117 nm). The coincidence counts between different wavelength channels of the AWG are measured in a coincidence counter PicoHarp 300 at 512 time-bin-width, which are shown in Fig. 6.3. It is evident that at these parameters, all 16 channel pairs are highly spectrally correlated e.g. channel number 35 (C35) shows a high coincidence with channel 34 (C34) only (C35 has a coincidence of $\sim$ 666/s with C34, $\sim$ 18/s with C33, and $\leq$ 2/s with the rest), and channel 36 shows a high coincidence with channel 33 only, and so on. We find negligible cross-talk throughout the 16 channel pairs. This indicates that all 16 channel pairs can be used to route the entangled photons for multi-user QKD and communication.

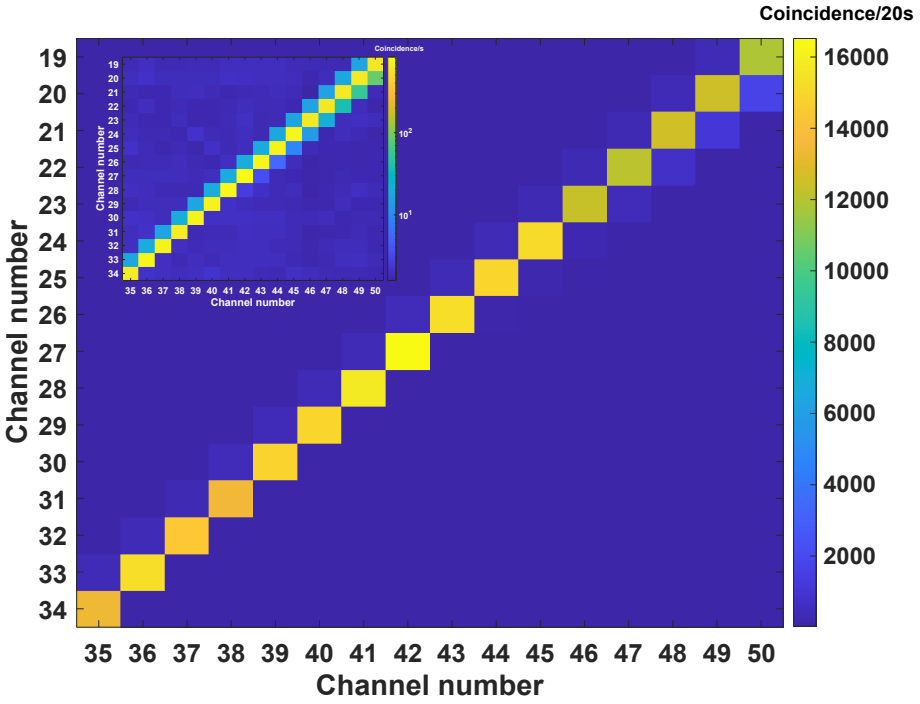

FIGURE 6.3: AWG channel pair correlation at waveguide temperature = 34.33°C, pump wavelength = 774.8938 nm, and pump power ∼ 39 µW. The x and y-axis show the ITU channels, and the color bar indicates the coincidence counts/20s. The Inset image shows the coincidences/s in the log scale.

6.2.2 ITU channel allocation on emission spectrum

The photon pair emission spectrum and the AWG's ITU channel pairs are shown in Fig. 6.4. The pink dots represent the experimentally measured telecom photon pair spectrum, and the dashed blue line is the theoretical sinc^2. The colored bars are the AWG channel wavelengths where red, green, and blue bars on the signal side correspond to channels 37 (C37 = 1547.721 nm), 38 (C38 = 1546.921 nm), and 39 (C39 = 1546.125 nm), respectively. The grey color bar shows channel number 50 (C50 = 1537.407 nm). On the idler side, the color bars in the same sequence correspond to channel numbers 32 (C32 = 1551.724 nm), 31 (C31 = 1552.538 nm), 30 (C30 = 1553.322 nm), and 19 (C19 = 1562.23 nm) respectively. The same colored bars indicate an entangled photon pair; for example, photons of channel C37 are entangled with the photons of C32, and similarly, photons of channel pair C50 are

entangled with photons of channel C19. Here, we characterize the entanglement in 14 channel pairs (C37-C32 to C50-C19) of the AWG that lies only within the highly efficient region of the emission spectrum. It is evident from Fig. 6.4 that more channel pairs (up to ∼ 40) can be exploited for quantum communication/key distribution since a large portion of the emission spectrum is still unused by our 32-channel AWG.

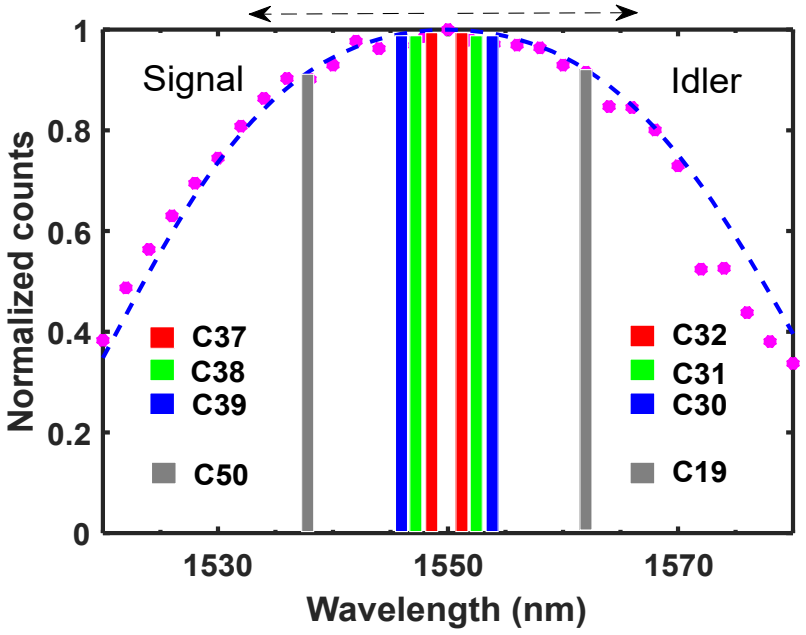

FIGURE 6.4: Telecom photon pairs emission spectrum centered around 1550 nm and ITU channels. The pink dots represent the experimental values of photon counts with respect to wavelength, and the dotted blue line is the theoretical sinc^2. The colored bars show the ITU channels of AWG (channel spacing 100 GHz), and the same color bars on both sides of 1550 nm correspond to an entangled channel pair.

6.3 Multi-user source of polarization entangled photon pairs in low loss telecom C-band

6.3.1 Experimental setup

Figure 6.5(a) shows the experimental setup for polarization-entangled photon pair generation and characterization for multi-user quantum communication and secret key distribution. The experimental setup is partially the same as we discussed in the last chapter (Chapter 5). We use a CW tunable laser to pump the fiber-pigtailed Zn-indiffused MgO:PPLN ridge waveguide (Waveguide 2, phase-matching temperature 36.5℃, length 40-mm) in the Sagnac loop configuration for broadband polarization-entangled photon pair generation. Though the waveguide is type-0 phase-matched for degenerate down-conversion i.e. 775 nm (pump, V-pol) → 1550 nm (signal, V-pol) + 1550 nm (idler, V-pol) at temperature 36.5℃, the generated spectrum's central wavelength can be slightly tuned by tuning the pump wavelength and waveguide temperature. The generated signal (shorter-wavelength) and idler (longer-wavelength) photons are separated into the C- (∼ 1520-1550 nm) and L- (∼ 1550-1580 nm) arms, respectively, of a telecom C-L band splitter and a pair of fiber polarization controllers are used in the C- and L-arm to control the output polarization and to introduce a desired phase in two paths. We then use a combination of a QWP, HWP, and FPBS for entanglement analysis before combining the entangled photon pairs into a single fiber through another C-L band splitter/-combiner. Finally, we demultiplex the entangled photon spectrum into various ITU channels using a 32-channel AWG. The quantum state fidelity, two-photon interference, and violation of CHSH-Bell's inequality are then characterized in 14 channel pairs using QWP, HWP, and an FPBS (that are placed in the C- and L-arms). The

experimental setup is designed in such a manner that once we switch on the source, the entanglement in all 14 channel pairs can be analyzed simultaneously in a single measurement.

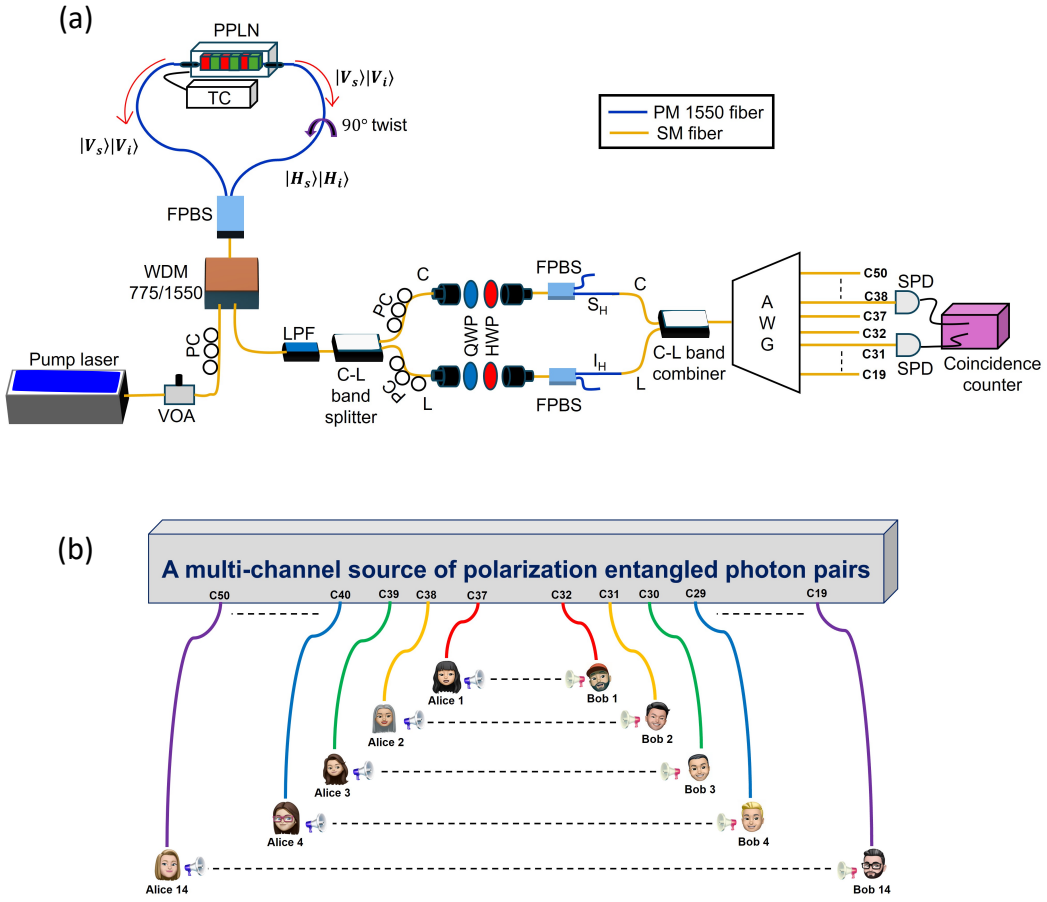

FIGURE 6.5: (a) Experimental setup for polarization-entangled photon pair generation and characterization for multi-user communication and secure key distribution at telecom wavelengths. VOA: Variable optical attenuator, PC: Fiber polarization controller, WDM: Wavelength-division-multiplexer, FPBS: Fiber polarization beam splitter, TC: Temperature controller, LPF: Long-pass filter, QWP: Quarter wave plate, HWP: Half wave plate, SPD: Single photon detector, AWG: Arrayed waveguide grating, $I_H/|H_i\rangle$: Idler with horizontal polarization, $S_H/|H_s\rangle$: Signal with horizontal polarization, $|V_i\rangle$: Idler with vertical polarization, $|V_s\rangle$: Signal with vertical polarization. The blue and brown lines represent the polarization maintaining and single mode fiber, respectively. C19 to C50 are the wavelength channels in the ITU grid (C-band). (b) Schematic for simultaneous multi-user communication using the polarization-entangled photon pair source.

However, here, we characterize the entanglement in all channel pairs one by one

by employing a single pair of single-photon avalanche photodetectors (SPAD) (ID Quantique: ID Qube-NIR-FR-MMF-LN, detection efficiency 20%, dead time 5 µs, timing jitter $\lesssim$ 200 ps, and dark counts $<$ 700 cps) due to the unavailability of 14 detector pairs. Rather than optimizing the setup for maximum fidelity in each channel pair, the setup is optimized once, and the measurement is carried out in all channel pairs (sequentially) to see the realistic application of the source. The coincidence events between the two detectors are recorded in a time-tagger unit (PicoQuant: PicoHarp 300) with a time-bin-width of 512 ps. Figure 6.5(b) shows the schematic of how 14 different user pairs can utilize the source simultaneously for quantum communication and secret key distribution.

6.3.2 Tunable Bell state generation and characterization

As discussed earlier, the cross-talk between the channel pair is minimal at waveguide temperature T = 34.33℃ and pump wavelength λ = 774.8938-nm. Thus, we pump the waveguide at the above-mentioned wavelength and temperature to generate a polarization-entangled Bell state in all channel pairs. We first attenuate the waveguide input pump (λ = 774.8938-nm) power to $\sim$ 50 µW using a variable optical attenuator (VOA) and then use an input fiber polarization controller to adjust the pump polarization for the maximally entangled $|\Phi^+\rangle$ Bell-state generation.

$$\left|\Phi^+\right\rangle = \frac{1}{\sqrt{2}}(|H_s\rangle\,|H_i\rangle + |V_s\rangle\,|V_i\rangle) \tag{6.1}$$

The topology shown in Fig. 6.5(a) allows us to characterize the entanglement in all 14 channel pairs (from C37-C32 to C50-C19) at once without altering the setup.

Here, we leave out channel pair C35-C34 and C36-C33 due to the C-L band splitter's substantial uneven insertion loss at these wavelengths as a result of the band splitter's transmission profile.

The experimental setup can also be tuned to generate the $|\Phi^-\rangle$ Bell state

$$\left|\Phi^-\right\rangle = \frac{1}{\sqrt{2}}(|H_s\rangle\,|H_i\rangle - |V_s\rangle\,|V_i\rangle) \tag{6.2}$$

The approach used here is based on the fact that a unitary transformation on one of the qubits of a Bell state can convert it to another Bell state [153]. The $|\Phi^+\rangle$ Bell state can be converted into the $|\Phi^-\rangle$ Bell state if we use a HWP at 0° (i.e. fast axis of the HWP is aligned at an angle 0° with respect to the horizontal axis) in front of either signal or idler arm's polarization analysis unit. In our case, we achieve this desired phase between the C (signal) and L (idler) arm (to convert one state to another) with the help of two fiber polarization controllers that are placed at the end of the first C-L band splitter.

To experimentally investigate the generation of two different Bell states, we first optimize the source for the entanglement generation in channel pair C38-C31 and observe the two-photon interference (see Fig. 6.6(a) and 6.6(b)). The idler photons traveling in the L-arm are projected into H-V and D-A bases using a HWP and an FPBS, and the polarization of signal photons traveling in the C-arm is continuously varied by rotating the corresponding HWP. While measuring in the D-A basis, we notice that for the $|\Phi^-\rangle$ Bell state, the maximum coincidence occurs when the idler photon is projected into D-polarization, and the signal is A-polarized, whereas, for the $|\Phi^+\rangle$ Bell state, the maximum coincidence occurs when the signal is also D-polarized, certifying the generation of two different Bell states. The behavior of interference fringes for the $|\Phi^-\rangle$ and $|\Phi^+\rangle$ Bell states are similar in H-V basis and are

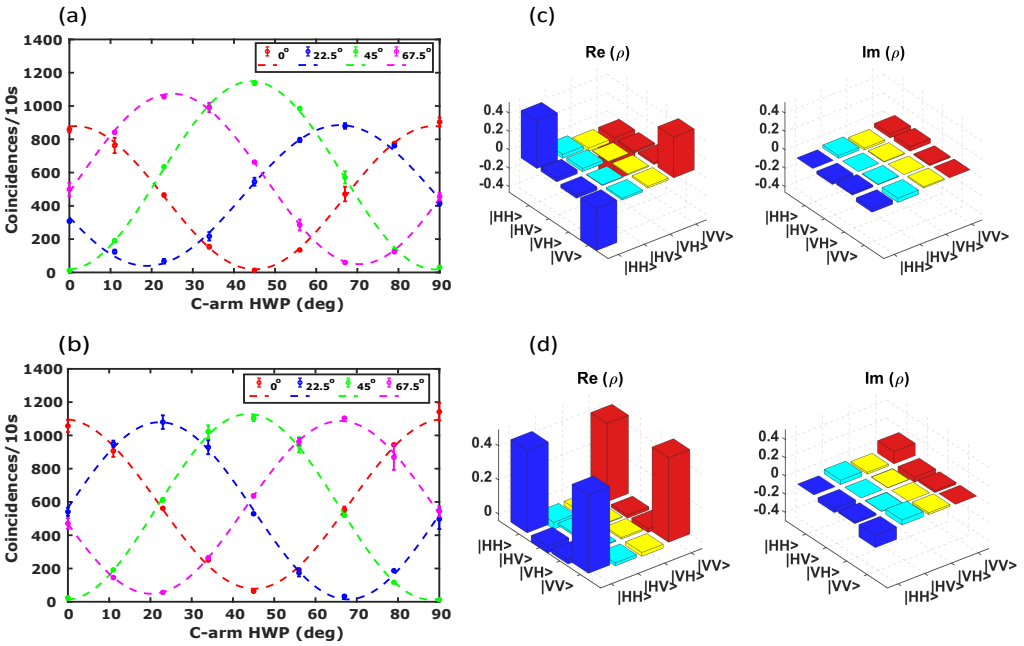

FIGURE 6.6: Two-photon interference fringes for the generated (a) $|\Phi^-\rangle$ Bell state (b) $|\Phi^+\rangle$ Bell state in ITU channel pair C38 (1546.921 nm) - C31 (1552.538 nm). The dots and the dashed lines show the experimental data and sinusoidal fit, respectively. Real and imaginary parts of the reconstructed density matrix of the (c) $|\Phi^-\rangle$ Bell state (d) $|\Phi^+\rangle$ Bell state in channel pair C38-C31. The raw fidelities corresponding to the $|\Phi^-\rangle$ and $|\Phi^+\rangle$ Bell states are $\sim 94\%$ and $\sim 95\%$, respectively. Various colors in the density matrix are intended for presentation purposes only and do not reflect any information.

opposite in the D-A basis (for details, see Chapter 1). In Fig. 6.6(a) and 6.6(b), the dots stand for experimental values, and the dashed lines are the sinusoidal fit. The fringe visibilities in H (0°), D (22.5°), V (45°), and A (67.5°) polarization projections are 95.98%, 88.23%, 96.91%, and 89.38%, respectively, for the $|\Phi^-\rangle$ Bell state, and for the $|\Phi^+\rangle$ Bell state the corresponding visibilities are 86.71%, 94.07%, 97.71%, and 90.01%, respectively.

Further certification for two different Bell state generations is given via QST. TABLE 6.1 shows the measured coincidence counts in channel pair C38-C31 for two Bell states during the QST measurement, and Fig. 6.6(c) and 6.6(d) shows the reconstructed density matrices for $|\Phi^-\rangle$ and $|\Phi^+\rangle$ Bell states, respectively. The raw fidelities for the $|\Phi^-\rangle$ and $|\Phi^+\rangle$ Bell states are $\sim 94\%$ and $\sim 95\%$, respectively. This

TABLE 6.1: Quantum state tomography (QST) measurement for $|\Phi^-\rangle$ and $|\Phi^+\rangle$ Bell states in ITU channel pair C38-C31 [73].

	Signal path (C-arm)		Idler path (L-arm)		$\|\Phi^-\rangle$ Bell state	$\|\Phi^+\rangle$ Bell state
S.N.	QWP angle	HWP angle	QWP angle	HWP angle	Coincidence/10-s (Average counts)	Coincidence/10-s (Average counts)
1	0°	45°	0°	45°	938	1055
2	0°	45°	0°	0°	50	21
3	0°	0°	0°	0°	798	1022
4	0°	0°	0°	45°	22	19
5	0°	22.5°	0°	45°	381	604
6	0°	22.5°	0°	0°	572	454
7	45°	22.5°	0°	0°	467	516
8	45°	22.5°	0°	45°	419	459
9	45°	22.5°	0°	22.5°	443	732
10	45°	22.5°	45°	22.5°	27	1025
11	0°	22.5°	45°	22.5°	626	545
12	0°	45°	45°	22.5°	637	412
13	0°	0°	45°	22.5°	415	485
14	0°	0°	90°	22.5°	373	629
15	0°	45°	90°	22.5°	499	462
16	0°	22.5°	90°	22.5°	46	963

shows that the source can generate both the Bell states with high fidelity, and the output state can be easily tuned from $|\Phi^-\rangle$ to $|\Phi^+\rangle$ or vice-versa with the help of a manual fiber polarization controller.

6.3.3 Polarization-entanglement characterization in all 14 ITU channel pairs

For the scaling of a WDM-based quantum communication network, the source must have the capacity to serve a large number of users, as this will reduce the total number of sources required to build a large quantum network and also the financial cost of the infrastructure [47]. The hardware needed for simultaneous quantum communication between multiple users can be reduced when a large number of wavelength

channels of the source are exploited, enabling all users to be fully connected such that each user shares quantum entanglement with every other user of the network [46, 47]. In this regard, we evaluate the capacity of our source and the number of channel pairs that can be used for secure communication, QKD, and entanglement transmission to remote users. Here, we measure the violation of CHSH inequality, concurrence, and entanglement fidelity (by performing QST) in 14 ITU channel pairs without altering the experimental setup. We first optimize the source once for maximum entanglement generation in channel pair C38-C31 and then use a single pair of SPAD to characterize the entanglement in all channel pairs sequentially. Figures 6.7(a), 6.7(b), and 6.7(c) show the quantum state fidelity, concurrence, and S-parameter, respectively, for both $|\Phi^-\rangle$ and $|\Phi^+\rangle$ Bell states in all 14 ITU channel pairs (C37-C32 to C50-C19). The pink shaded area in 6.7(a) and 6.7(b) shows the classical region for fidelity and concurrence, respectively, which means that if the value falls outside of this range, it indicates the generation of a quantum (non-classical) state. It is evident that, in our case, the generated state is a high-quality quantum state in all channel pairs.

The raw fidelity is $> 90\%$ in all channel pairs for the $|\Phi^-\rangle$ Bell state, and the maximum fidelity is $\sim 94\%$ in channel pair C38-C31 and C39-C30. For the $|\Phi^+\rangle$ Bell state, the raw fidelity is $\gtrsim 89\%$ in all channel pairs, and the maximum fidelity is $\sim 95\%$ in channel pair C38-C31. The raw concurrence is $\gtrsim 0.82$ in all channel pairs for the $|\Phi^-\rangle$ Bell state, and the maximum value is ~ 0.88 in channel pairs C38-C31 and C39-C30. For the $|\Phi^+\rangle$ Bell state, the raw concurrence is $\gtrsim 0.8$ in all channel pairs, and the maximum concurrence is ~ 0.91 in channel pair C38-C31. It is obvious from Fig. 6.7(c) that each channel pair carries an entangled photon pair as it substantially violates the CHSH-Bell's inequality (i.e. $S > 2$) by many standard deviations. The minimum value of S-parameter is $\sim 2.65 \pm 0.03$ and the maximum

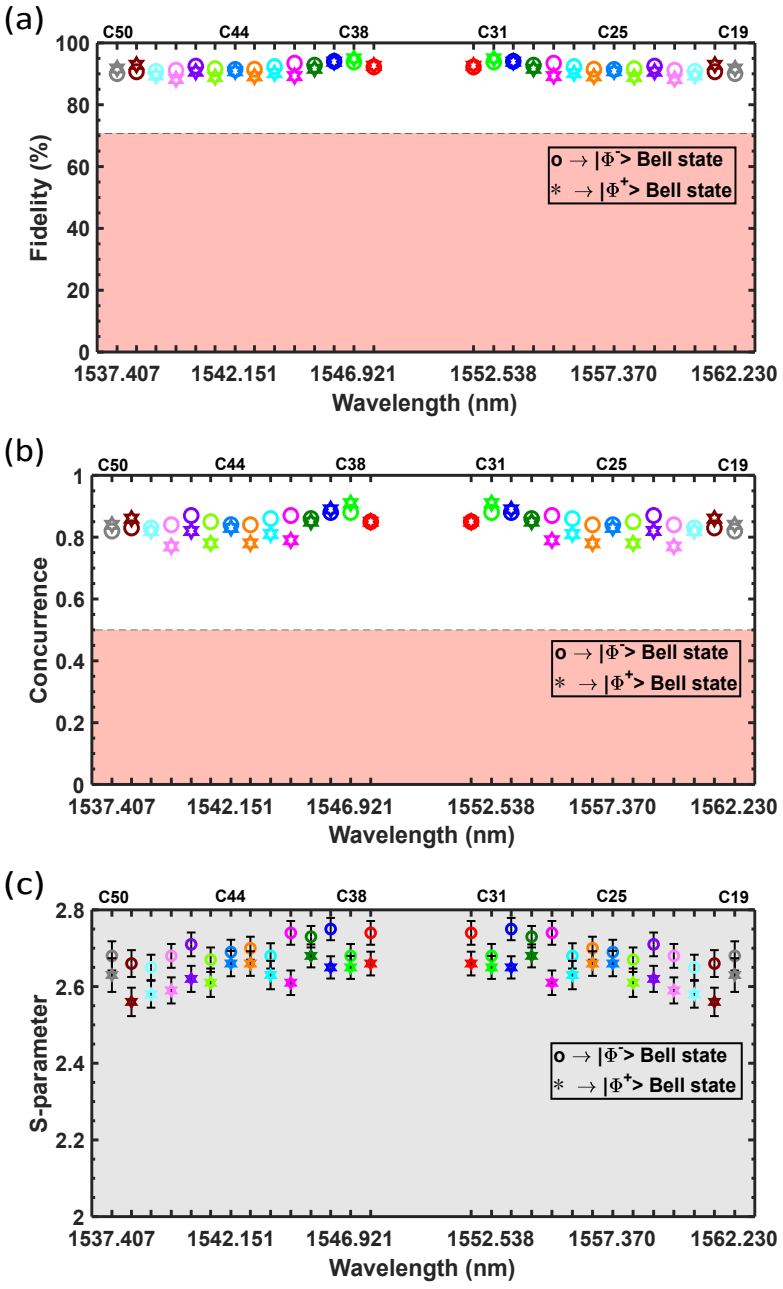

FIGURE 6.7: (a) Raw fidelity (b) raw concurrence and (c) S-parameter for the $|\Phi^-\rangle$ and $|\Phi^+\rangle$ Bell states in 14 different ITU channel pairs. Here, the circles correspond to the $|\Phi^-\rangle$ Bell state, and hexagons (stars) correspond to the $|\Phi^+\rangle$ Bell state. The top x-axis shows the ITU channel number, and the bottom x-axis shows the corresponding wavelength of the channels. The experimental values of a particular Bell state (circles or hexagons) of the same color indicate the same number. For example, the gray circles corresponding to a $|\Phi^-\rangle$ state have the same value of fidelity/concurrence/S-parameter for channel number C50 and C19 because the entanglement is measured in the channel pair C50-C19. The pink-shaded region in fidelity and concurrence shows the classical domain, i.e. if a value falls outside of the pink-shaded region, it indicates that the state is quantum. The gray-shaded region in the S-parameter represents the quantum domain.

value is $\sim 2.75 \pm 0.03$ for the $|\Phi^-\rangle$ Bell state; and for the $|\Phi^+\rangle$ state the minimum value is $\sim 2.56 \pm 0.04$ and the maximum value is $\sim 2.68 \pm 0.03$. The S-parameter for $|\Phi^+\rangle$ Bell state is calculated by $S = |(E(\theta_a, \theta_b) - E(\theta_a, \theta_b^{'}) + E(\theta_a^{'}, \theta_b) + E(\theta_a^{'}, \theta_b^{'})|$ (see Chapter 1 for details) and for $|\Phi^-\rangle$ Bell state is calculated by $S = |(E(\theta_a, \theta_b^{'}) - E(\theta_a, \theta_b) + E(\theta_a^{'}, \theta_b) + E(\theta_a^{'}, \theta_b^{'})|$ using HWP angles $\theta_a = 0°$, $\theta_a^{'} = 22.5°$, $\theta_b = 11.25°$, and $\theta_b^{'} = 33.75°$.

The above results show that all 14 channel pairs carry an independent bipartite polarization-entangled Bell state given by

$$\left|\Phi_n^{\pm}\right\rangle = \frac{1}{\sqrt{2}}(\left|H_{\lambda_{n,s}}\right\rangle \left|H_{\lambda_{n,i}^{'}}\right\rangle \pm \left|V_{\lambda_{n,s}}\right\rangle \left|V_{\lambda_{n,i}^{'}}\right\rangle) \tag{6.3}$$

here $n = 1, 2, 3, ...14$ and $\left|H_{\lambda_{n,s}}\right\rangle$, $\left|H_{\lambda_{n,i}^{'}}\right\rangle$ denotes the horizontally polarized signal and idler photons of n$^{\text{th}}$ wavelength channel pair having a wavelength of λ_n and $\lambda_n^{'}$, respectively; $\left|V_{\lambda_{n,s}}\right\rangle$, $\left|V_{\lambda_{n,i}^{'}}\right\rangle$ denotes the vertically polarized signal and idler photons of n$^{\text{th}}$ wavelength channel pair having a wavelength of λ_n and $\lambda_n^{'}$, respectively. Since each channel pair has unique wavelengths and negligible cross-talk, this indicates the parallel generation of 14 independent bipartite polarization-entangled states that can be exploited in a WDM-based quantum communication network. For example, 14 user pairs can access the source simultaneously for quantum communication and/or secret key distribution if we deploy a two-user communication scheme, as shown in Fig. 6.5(b). Alice 1 can communicate with Bob 1, Alice 2 can communicate with Bob 2, and so on because each user pair owns a unique bipartite entangled state independent of any other user pair. Alice 1 can not communicate with any other user except Bob 1 since they do not share any entangled photons. However, this can be enabled if we use optical switches to route the photons of Bob 1 to any other user with whom Alice 1 wants to communicate [130] or all the channels can be

multiplexed to form a complete network where each user shares entanglement with every other user [46, 47].

6.4 Long-distance (up to 100 km) entanglement transmission

To transfer the entangled photons to remote parties for quantum communication and key distribution, the source needs to be highly efficient. In a realistic scenario, the users of a metropolitan-scale quantum network are located dozens of kilometers apart. Therefore, the source must be able to send entangled photons to these remote users. This requires the multi-user source to have high-fidelity entanglement, compactness, and low bit error rate. We assess our source in this context by observing the fidelity of the transmitted state, coincidence rate, and QBER when these entangled photon pairs are sent over a long distance via fiber spools (Sterlite Technologies Ltd.).

Since we have already characterized and verified the simultaneous entanglement in all channel pairs, we now exclude the two C-L band splitters and directly connect the AWG to the LPF, as this will allow us to exploit all the 16-channel pairs of the AWG and would mimic a more realistic scenario where each user pair of the quantum network will have their separate polarization analysis module for entanglement characterization and key distribution. Figure 6.8 shows the experimental setup for long-distance transmission of entangled photons where we select the ITU channel pair C38-C31 (pertaining to one user pair, Alice and Bob, respectively) and connect a fiber spool in one or both channels and measure the entanglement. Here, we study three different scenarios: a) when C38 and C31 both have 50 km fiber

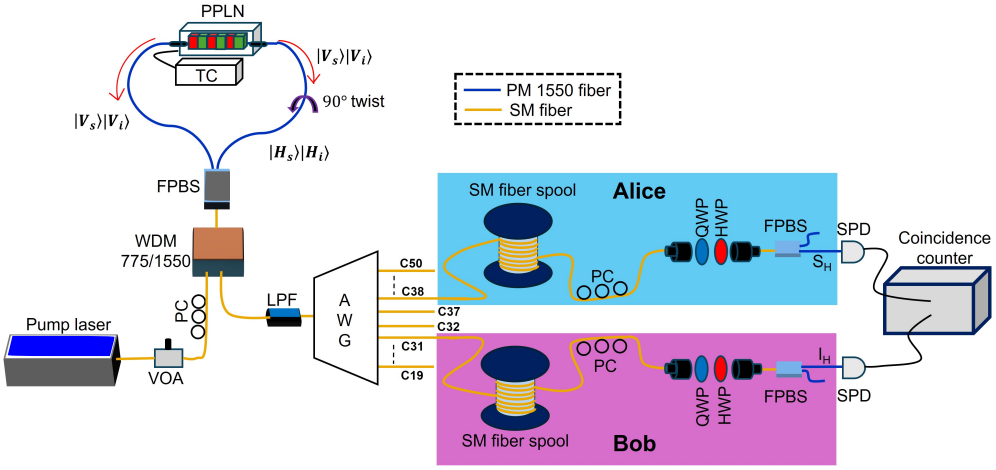

FIGURE 6.8: Experimental setup of a multi-user telecom source for long-distance transmission of polarization-entangled photon pairs. VOA: Variable optical attenuator, PC: Fiber polarization controller, WDM: Wavelength division multiplexer, FPBS: Fiber polarization beam splitter, TC: Temperature controller, LPF: Long-pass filter, AWG: Arrayed waveguide grating, SM fiber spool: Single mode fiber spool, QWP: Quarter wave plate, HWP: Half wave plate, SPD: Single photon detector, $I_H/|H_i\rangle$: Idler with horizontal polarization, $S_H/|H_s\rangle$: Signal with horizontal polarization, $|V_i\rangle$: Idler with vertical polarization, $|V_s\rangle$: Signal with vertical polarization. The blue and brown lines show the polarization maintaining and single mode fiber, respectively. The coincidences are measured in a Swabian time tagger unit with a 512 ps detection window.

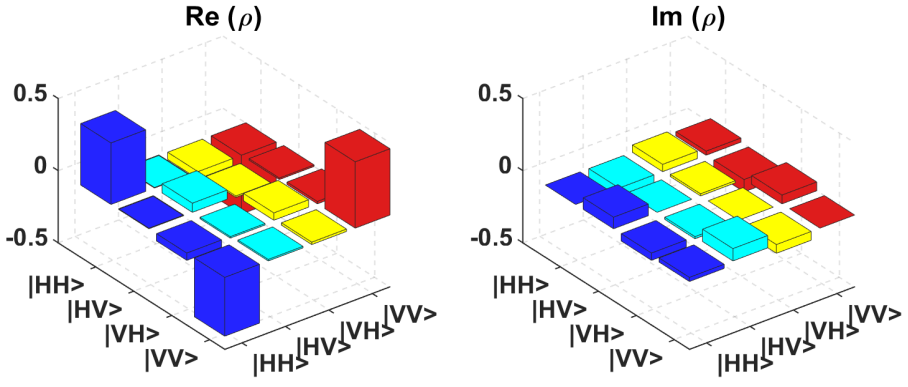

FIGURE 6.9: Real and imaginary part of the reconstructed density matrix of a $|\Phi^-\rangle$ Bell state after transmitting one of the photons (i.e. Bob's Photon) over 100 km distance via fiber spool. Here, we use ITU channel pair C38-C31 for long-distance transmission between two remote users. The observed raw fidelity and concurrence are approximately 85.1% and 0.71, respectively.

spools; b) C31 has a 50 km fiber spool, and C38 does not have any fiber spool; c) C31 has a 100 km fiber (serial connection of two 50 km fiber spools), and C38 does not have any fiber spool. The measured insertion loss of the two 50-km-long fiber spools is 13.5 dB and 13.7 dB, respectively. The measured results are listed in TABLE 6.2. In all three cases, the fidelity is $> 85\%$, and QBER is $< 9\%$ (below the generally accepted 11% threshold for error-correction [154, 155]), which shows that the high-quality entangled photon pairs can be transmitted to remote users for communication and key distribution. Here QBER is estimated via the ratio of wrong bits to the total number of bits ($\frac{N_{wrong}}{N_{wrong}+N_{correct}}$, where N_{wrong} is the sum of the minima of two-photon interference in H-V and D-A basis, and $N_{correct}$ is the sum of the maxima of two-photon interference in H-V and D-A basis). The reconstructed density matrix for the last case when Bob's photon is transmitted over 100 km, and Alice's photon is detected just after the AWG channel C38 is shown in Fig. 6.9. The above results highlight the quality of our source for long-distance multi-user quantum communication.

6.5 Effect of polarization mode dispersion (PMD) on entanglement distribution

PMD is a major reason for entanglement degradation in optical fiber-based quantum communication [156]. When two orthogonal polarizations travel through the birefringent medium, they travel at different speeds, resulting in differential delay/walk-off, known as PMD. The PMD is a concern in optical fiber-based quantum networks for entanglement distribution among remote users due to the introduction of distinguishability between the two polarization components in each photon leading to the

TABLE 6.2: Measurement of coincidence rate, fidelity (F), concurrence (C), and quantum bit error rate (QBER) in long-distance transmission of polarization entangled photons via fiber spools. Three combinations of fiber spools in ITU channel pair C38 (Alice) - C31 (Bob) are used for long-distance entanglement transmission. For cases 2 and 3, when no fiber spool is used in channel C38, an equivalent electronic delay is observed in the coincidence peak and accounted for. Alice and Bob's photons are detected using InGaAs APDs (ID qube NIR, quantum efficiency (Q.E.) 20%, dead time 5 µs, and dark counts < 700 cps), and the coincidence events are counted using Swabian time tagger X (coincidence window 512 ps).

S.N.	Case	Measured coincidence/s with APD (Q.E. = 20%)	Estimated coincidence/s with SNSPD (Q.E. = 95%)	F	C	QBER
1	Alice: 50 km fiber Bob: 50 km fiber	25	564	87.2%	0.82	5%
2	Alice: no fiber Bob: 50 km fiber	120	2707	86.8%	0.79	6.4%
3	Alice: no fiber Bob: 100 km fiber	18	406	85.1%	0.71	9%

degradation of entanglement [156, 157, 158]. Single-mode fibers in the submarine cable environment or aerial exposure experience stress, sudden change in temperature, or change in ambient condition, which induces birefringence, hence PMD, resulting in the deterioration of the quality of the entangled state [159]. Thus, it is necessary to comprehensively understand the effect of PMD on polarization entanglement for effective quantum communication among distant users. Here, we study the change in the concurrence (C) (a parameter to quantify entanglement) of the transmitted entangled state if we use different-length single-mode or polarization-maintaining fibers to transmit the photons of the two channels to a user pair (say, Alice and Bob). The experimental setup used for this study is similar to Fig. 6.8. The SM fibers of the spool have a PMD value of 0.1 ps/$\sqrt{\text{km}}$ and chromatic dispersion of $\leq$ 17.5 ps/nm.km (according to the specification sheet). It is observed that if we use single-mode fibers for the entanglement transmission, the concurrence of the entangled state does not change by a huge amount even if we keep a single-mode fiber length difference of

100 km between the two remote users (see Fig. 6.10(a)), which is also suggested by the theory in the absence of any external environmentally introduced stresses [158]. Here the solid blue line corresponds to the case when we consider a PMD value of 0.1 ps/$\sqrt{\text{km}}$ in single-mode fiber, and the dotted blue line corresponds to the case when we consider a PMD value of 0.35 ps/$\sqrt{\text{km}}$ [160]. Our experimental result agrees well with the theory. We note that a slight drop in concurrence with fiber length could also have contributions from polarization-dependent-loss (PDL), chromatic dispersion, and wavelength-dependent-loss (although expected to be small), and this probably requires a more detailed study on its own. Nonetheless, this suggests that stable single-mode fibers, such as the submarine fibers, will not degrade the entanglement significantly and will require very slow live adjustment, whereas aerial fibers will require faster compensation systems for stability [4]. In order to see the effect of high PMD on concurrence, we put polarization-maintaining fiber patch cords of different lengths in channels C38 and C31 instead of single-mode fiber spools, and it is observed that the concurrence drops significantly even with a very small fiber length difference in the two channels (see Fig. 6.10(b)). The red dots in Fig. 6.10(b) correspond to the experimental result, and the blue lines are the theoretical results. The solid blue line pertains to the case when we consider a beat length (L_b) of 5 mm (also claimed by the manufacturer) for differential group delay (DGD) calculation in these polarization-maintaining fibers, and the dotted blue line pertains to the case when we consider a beat length of 2.5 mm. Our experimental values slightly deviate from the solid blue line (theoretical curve) but agree well with the dotted blue line (theoretical curve). This study suggests that an increase in PMD deteriorates the entanglement quality rapidly, and single-mode fibers encased in stable cables are an excellent media to safely transfer the polarization entanglement to remote users for communication or key distribution in a quantum network. The theoretical curves shown in Fig. 6.10(a) and 6.10(b) are obtained through the

expression [158]

$$C(\tau_a, \tau_b) = exp(-\frac{1}{2}\frac{(\tau_a - \tau_b)^2 B_a^2 B_b^2}{B_a^2 + B_b^2}) \tag{6.4}$$

where $\tau_{a,b}$ is the DGD in Alice and Bob's path, respectively, and $B_{a,b}$ is their respective filter's bandwidth. For single-mode fiber DGD ($\tau_{a,b}$) is calculated using (0.1 ps/$\sqrt{\text{km}}$) $\times \sqrt{L}$ and (0.35 ps/$\sqrt{\text{km}}$) $\times \sqrt{L}$ where L is the fiber length in km; and for the polarization-maintaining fiber, DGD is calculated using $\frac{L\lambda}{cL_b}$, where L is the fiber length, λ is the wavelength propagating through the fiber, c is the speed of light, and L_b is the beat length. The experimental data of Fig. 6.10(a) is obtained from the QST measurement and the experimental data of Fig. 6.10(b) is estimated from the two-photon interference fringes of the H-V and D-A basis (as discussed in Chapter 1) due to experimental difficulty of QST measurement for each data point.

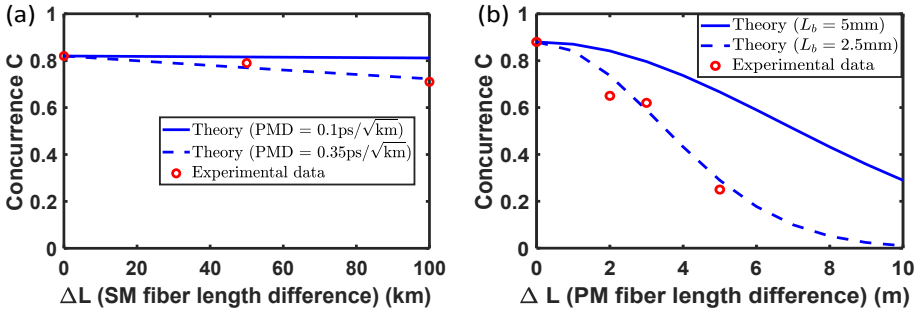

FIGURE 6.10: Variation of concurrence with (a) single-mode (SM) fiber length difference (PMD) in two channels (C38, C31) (b) polarization-maintaining (PM) fiber length difference (PMD) in two channels (C38, C31). The solid and dotted blue lines are the theoretical estimates, and the red dots are the experimental values.

6.6 Conclusion

We have characterized a fully fiber-integrated multi-user source of polarization-entangled photon pairs in the telecom C-band. The source is based on type-0 SPDC

in a fiber-pigtailed Zn-indiffused MgO:PPLN ridge waveguide in Sagnac configuration, and it can be easily tuned with the help of a fiber-polarization controller to generate either $|\Phi^+\rangle$ or $|\Phi^-\rangle$ Bell state. We generate 14 independent bipartite polarization-entangled states simultaneously through the demultiplexing of the emission spectrum with a telecom DWDM AWG. The entanglement is analyzed in all 14 ITU channel pairs (C37-C32 to C50-C19) for both $|\Phi^+\rangle$ and $|\Phi^-\rangle$ Bell states, and the observed raw fidelity $> 90\%$ for $|\Phi^-\rangle$ Bell state and $\gtrsim 89\%$ for $|\Phi^+\rangle$ Bell state. The raw concurrence for both the Bell states ($|\Phi^-\rangle$ and $|\Phi^+\rangle$) is $\gtrsim 0.8$ (in all channel pairs), and the maximum values are ~ 0.88 and ~ 0.91 respectively, pertaining to channel pair C38-C31. The observed S-parameter ($> 2.56 \pm 0.04$) violates the CHSH-Bell's inequality in all the channel pairs for both the Bell states. We test the source's quality by demonstrating entanglement distribution up to 100 km using single-mode fiber spools in channel pair C38-C31. The high fidelity ($>$ 85%) and low QBER ($< 9\%$) values suggest that the source can potentially be used for long-distance multi-user communication and secure key distribution. The PMD study suggests that polarization-maintaining fibers degrade the entanglement much quicker than the single-mode fibers. This indicates that the single-mode fibers in the shielded cables are the best optical media for entanglement distribution among distant users in a quantum communication network. Here, we have shown only 14 independent channel pairs of entangled photons, but more channels (up to $\sim$ 40 channel pairs with 100-GHz spacing) can be exploited since a large part of the photon emission spectrum is still not utilized. Our fiber-coupled source can be a potential candidate for long-distance transmission of entangled photons, multi-user communication, and secure key distribution over a metropolitan-scale quantum network.

Aknowledgement

We thank Sterlite Technologies Ltd. and Prof. Amol Choudhary, Department of Electrical Engineering, Indian Institute of Technology Delhi, New Delhi, India, for providing single-mode fiber spools for long-distance entanglement transmission measurement.

Chapter 7

Conclusions and future directions

7.1 Conclusions

Telecom photons are essential for fiber-based long-distance quantum communication, where they benefit from terrestrial and submarine fiber networks. Adequate sources of these telecom photons have been reported in the literature, but they all either require a lot of optical alignment and/or are not so efficient and easy to deploy. The optical fiber-based remote quantum communication requires efficient, compact, and easily deployable sources of polarization-entangled telecom photons, which are free of any optical alignment. In this regard, a fiber-integrated SPDC source stands out as a potential candidate that requires very little optimization to harness its maximum efficiency and is very easy to implement and deploy in the optical fiber network. These fully guided-wave sources have not been fully explored and investigated for many quantum applications. Therefore, this thesis aimed to explore fiber-integrated and/or compact sources of spectrally pure, spectrally correlated, and polarization-entangled photons at telecom wavelength in PPLN waveguides via SPDC. PPLN stands out as the best candidate for telecom photon pair generation owing to its

wide transparency window (350 nm - 5000 nm) [115], easy dispersion engineering, and high nonlinear strength (d_{31} = 4.85 pm/V, d_{33} = 25.3 pm/V) [115] (which results in large photon flux that is desired for long-distance communication).

In this thesis, we show the generation of two types of quantum state, spectrally pure biphoton state (Chapter 2, theoretical) and spectrally correlated/polarization-entangled biphoton state (Chapter 4 - Chapter 6, experimental) at telecom wavelength. Chapter 3 shows the characterization of PPLN through SHG.

We start with the description of two metrics, i.e., JSI and Schmidt decomposition, which are a measure of the spectral correlation of photon pairs in SPDC. We then present a comprehensible derivation of analytical formulae that can be used to find the Schmidt mode coefficients (λ_n) for spectral correlation measurement. The analytical expression is validated against a set of two published results [89, 91], and it satisfies all the required conditions of Schmidt decomposition and can be easily used to find the spectral correlation between photon pairs generated in any SPDC process. The proposed analysis gives more clarity and details than the existing formulation. We then propose an experimentally feasible LNOI ridge waveguide design to generate spectrally pure telecom photons at 1560 nm utilizing type-II SPDC. The estimated spectral purity of our source is $\sim 90\%$ from the exact numerical solution. The extensive study of the effects of pump bandwidth and waveguide length on spectral purity through both analytical and numerical solutions suggests that analytical expression slightly overestimates the spectral purity (due to side-lobe negligence of sinc function in PMF) and the two methods will converge if the effects of side-lobes of PMF is minimized. The spectral purity can be enhanced in practice by suppressing the side-lobes through an appropriately apodized QPM poling pattern, resulting in a Gaussian-shaped PMF [104] or by filtering the output biphoton state. We also check the effect of scattering losses (due to sidewall roughness) on spectral purity in

the LNOI ridge waveguide, and the results indicate the robustness of our proposed waveguide structure. The proposed on-chip source design generates spectrally pure photons, and it can be used as a heralded pure single-photon source for various quantum applications such as multi-port quantum interferometer-based computing, quantum simulation, and metrology [40, 79, 50, 80, 41]. If we pump the waveguide in a Sagnac configuration or employ a post-selection scheme in a single-pass configuration, the source can also generate photon pairs with simultaneous spectral purity and polarization-entanglement, which is desired for various photonic quantum computing and communication schemes [41, 109, 36, 110].

Next, we characterize a Zn-indiffused MgO:PPLN ridge waveguide (cross-section 10-µm×10-µm) through numerical mode analysis and SHG. The waveguide has a single-mode operation at 1550 nm and multi-mode at 775 nm; the fundamental modes are near circular and well confined (mode overlap $\sim$ 70.9%). We demonstrate the SHG in two Zn-indiffused MgO:PPLN waveguides, and the results show that one waveguide has a phase-matching temperature of $\sim$ 41℃ and SHG conversion efficiency of $\sim$ 30%/W, and another waveguide has a phase-matching temperature of 36.5℃ and SHG conversion efficiency of $\sim$ 40.4%/W. The temperature of the waveguide plays a crucial role in the phase-matching process, and its maximum efficiency can be harnessed only at phase-matching temperature. These efficient waveguides can be used in frequency doubled-lasers, harmonic generation for tissue imaging, ultra-short pulse characterization, and quantum light sources. After the SHG characterization, we use this fiber-coupled waveguide (phase-matching temp $\sim$ 41℃) in a completely fiber-integrated setup for the experimental broadband generation of spectrally and temporally correlated photon pairs at telecom wavelength via SPDC. We demonstrate a broadband emission of spectrally correlated photons (characterized through JSI) near 1550 nm with FWHM bandwidth $\sim$ 46 nm. The generated photon spans

the telecom S-, C-, and L-bands, and the estimated spectral brightness of our source is $\sim 2.5\times10^7$ pairs/s/mW/nm. A CAR value > 650 suggests a very high temporal correlation between the photon pairs and highlights the source's quality. The proposed fiber-integrated source can be used in quantum metrology, WDM-based multi-user QKD, and information processing applications over existing fiber-optic networks.

We then used these telecom photons' polarization degree of freedom to our advantage to generate a polarization-entangled Bell state ($|\Phi^+\rangle$). We pump the type-0 phase-matched Zn-indiffused MgO:PPLN ridge waveguide (phase-matching temp 36.5℃) in the Sagnac configuration to generate the broadband polarization-entangled photon pairs at telecom wavelength. The emission spectrum of the source is centered at 1550 nm with FWHM $\sim$ 52 nm, and it has an estimated spectral brightness of $\sim 2\times10^8$ pairs/s/mW/nm and CAR > 1000. We experimentally demonstrate the generation of broadband polarization entanglement through this fiber-coupled source where the entangled photon pairs span the telecom C- and L-bands. The polarization-entangled state has a raw fidelity of $> 89\%$, concurrence of ~ 0.83, and fringe visibility of $> 88\%$ and >86 % in H-V and D-A basis, respectively. The generated broadband entangled state violates the CHSH-Bell's inequality by 29 standard deviations ($S = 2.49 \pm 0.017$). This is the best-reported combination of fidelity, brightness, and bandwidth to date for a fiber-integrated source characterized using standard room temperature APD detectors, to the best of our knowledge [131, 133, 134, 151, 138, 139]. The results indicate that this simple fiber-integrated bright source mainly generates polarization-entangled photons over the entire broadband spectrum, and it can be directly used in a WDM-based QKD network by demultiplexing the spectral width, long-distance optical-fiber-based quantum communication, and in the investigation of the fundamental aspects of quantum optics.

Finally, we explored this fiber-integrated source for multi-user quantum communication applications. We experimentally demonstrate and characterize a fully fiber-integrated multi-user source of polarization-entangled photon pairs in the low-loss telecom C-band. We make use of an SPDC process in type-0 phase-matched and fiber-pigtailed Zn-indiffused MgO:PPLN ridge waveguide in Sagnac configuration to generate the polarization entanglement in multiple channels of the ITU grid. The source generates 14 independent bipartite polarization-entangled Bell states ($|\Phi^+\rangle$ or $|\Phi^-\rangle$) simultaneously through the demultiplexing of the emission spectrum with a telecom DWDM AWG (100 GHz spacing), and the output state can be easily flipped from $|\Phi^+\rangle$ to $|\Phi^-\rangle$ or vice-versa with the help of a fiber-polarization controller. We analyze the entanglement in 14 channel pairs of the ITU-grid (C37-C32 to C50-C19) through various entanglement witness parameters (for both Bell states). The observed raw fidelity $> 90\%$ for $|\Phi^-\rangle$ Bell state and $\gtrsim 89\%$ for $|\Phi^+\rangle$ Bell state in all channel pairs. The raw concurrence for both the Bell states ($|\Phi^-\rangle$ and $|\Phi^+\rangle$) is $\gtrsim 0.8$ (in all channel pairs), and the observed S-parameter ($> 2.56 \pm 0.04$) violates the CHSH-Bell's inequality by more than 14 standard deviations. The source's suitability for long-distance entanglement transmission is demonstrated by successfully transferring the entangled photons up to a distance of 100 km via single-mode fiber spools. The high fidelity ($> 85\%$) and low QBER ($< 9\%$) values suggest that the source can potentially be used for long-distance multi-user quantum communication and secure key distribution. We note that PMD degrades the entanglement quality very rapidly, and single-mode fiber is the best optical media for entanglement distribution among distant users in a quantum communication network. Though we have shown only 14 independent channel pairs of entangled photons in this multi-user source (which can further be multiplexed to create a complete network [46, 47]), more channels (up to ~ 40 channel pairs with 100-GHz spacing) can be exploited for quantum communication since a large part of the photon emission spectrum is

still not utilized. Our proposed fiber-coupled source can be a potential candidate for long-distance entanglement transmission, multi-user communication, and secure key distribution over a metropolitan-scale fiber-optic network.

Therefore, this thesis investigated PPLN-waveguide based telecom sources of spectrally pure, spectrally and temporally correlated, and polarization-entangled photons. We have explored completely fiber-integrated PPLN-waveguide based entangled-photon sources, which can be used for multi-user QKD and communication over metropolitan-scale fiber optic networks. The proposed and prototype sources can be easily deployed in the existing optical fiber infrastructure, and they could potentially boost the scaling of the quantum communication and information network.

7.2 Future directions

7.2.1 Field demonstration of the source for entanglement distribution to distant users

The source's compatibility and potential for entanglement distribution to real users over the existing fiber networks can be tested by performing a field demonstration of the source. The source can studied in two different scenarios (see Fig. 7.1) by transferring the photons through the deployed optical fiber within the Indian Institute of Technology Delhi (IITD) campus. Figure 7.1(a) shows the first scenario where we exploit one channel pair (say C38-C31) of the multi-user source such that we keep the source in the lab (Department of Physics, red circle in Fig. 7.1(a)) and send only the photons of channel C31 through the deployed dark optical fiber to JNU gate of IITD campus and then direct the photons back to the lab through

another dark fiber (from JNU gate to the lab). In this scenario, both photons can be detected in the lab, and entanglement can be characterized.

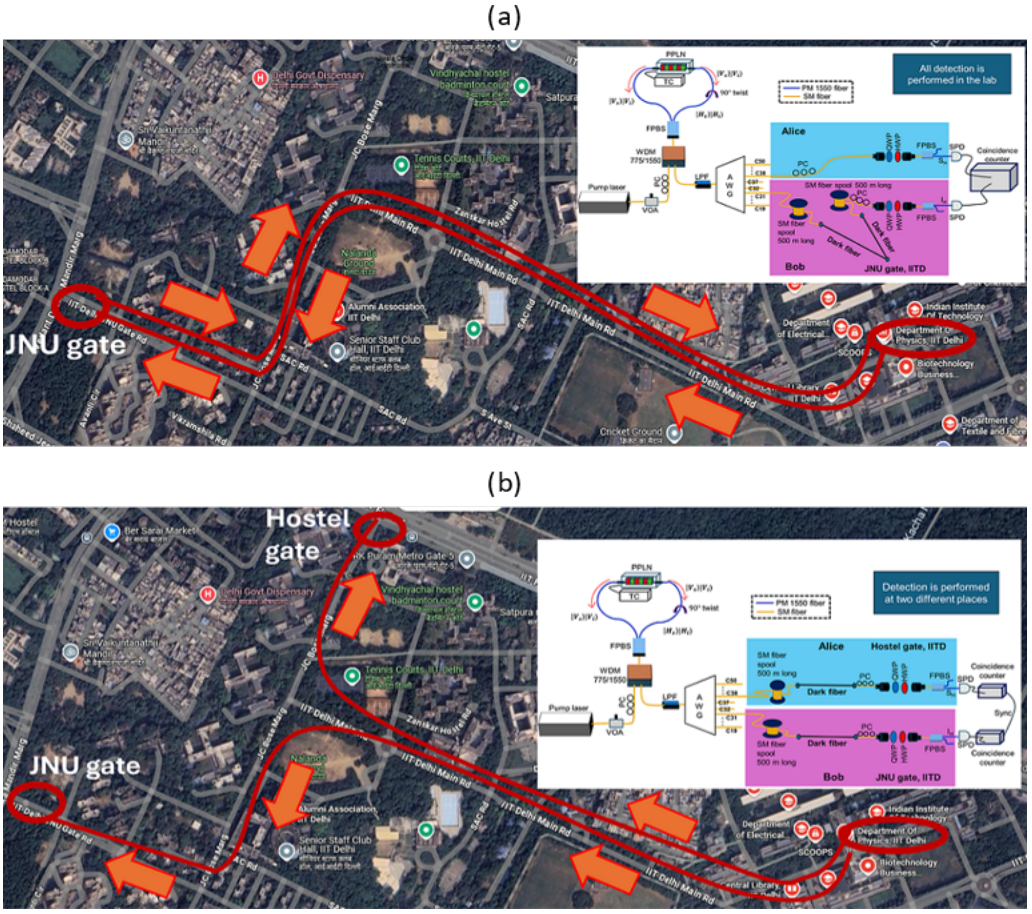

FIGURE 7.1: Field demonstration of the source for entanglement distribution to distant users through the deployed dark fibers in IIT Delhi campus. The photons are detected in two different scenarios: (a) in the lab and (b) at two different places outside the lab.

In the second scenario (see Fig. 7.1(b)), we can keep the source in the lab and send the photons of both channels (C38 and C31) to two different places (in this case, JNU gate and Hostel gate of IITD Campus) through the deployed dark fibers. Here, photons are detected at two different places (i.e. JNU gate and Hostel gate), so their time tags can be recorded in two separate coincidence counter devices, which are synchronized through a master clock. The time tags can be analyzed, and coincidence events between two photons can be counted in this fashion. We

can measure the entanglement by projecting the photons in different polarization bases, and we can see the realistic potential of the source for multi-user QKD over the existing fiber network.

7.2.2 A quantum network of user pairs

The proposed multi-user source can enhance the scalability or connectivity of the quantum communication network by exploiting more channel pairs. As mentioned earlier, the complete spectrum of polarization-entangled photons is not utilized by our 32-channel AWG (see Fig. 6.4). We can utilize the complete spectrum of the PPLN waveguide by de-multiplexing it with an 80-channel dense WDM/AWG with 100 GHz ($\sim$ 0.8 nm) channel spacing (see Fig. 7.2(a)). Here, the vertical red lines represent the channel position on the emission spectrum. Figure 7.2(b) shows the wavelengths of these 80 ITU channels, where the 1st channel has a wavelength of 1518.917 nm and the 80th channel has 1580.518 nm. These 80 channels constitute 40 pairs, where each pair shares a polarization-entangled state. For example, channels 1549.318 nm and 1550.117 nm will form one pair, and their photons are entangled in polarization. Similarly, channels 1518.917 nm and 1580.518 nm are entangled, and thus, the source's whole spectrum can be utilized by 40 user pairs (with a two-party communication scheme), say Alice 1 - Bob 1 to Alice 40 - Bob 40 (see Fig. 7.2(c)). These channel pairs can be further multiplexed with the schemes of Ref. [46, 47] or with a novel approach to interconnect the user pair to create a complete quantum communication network. The coincidence rate of each channel pair can also be enhanced by using SNSPD detectors and low-loss fiber optical components. Since we have already shown that entanglement can be transmitted to a distance of 100 km, the proposed work can be extended to create a citywide quantum communication network for practical users like banking, hospitals, financial companies, etc.

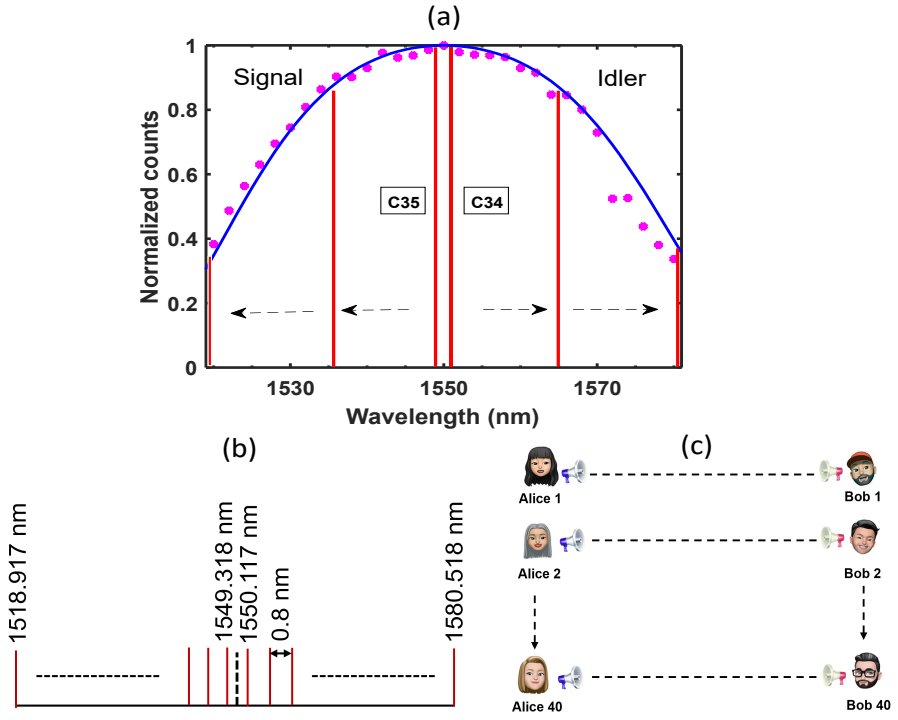

FIGURE 7.2: (a) 80 channels allocated on the emission spectrum with 100 GHz channel spacing. Pink dots represent the experimental data point, and the solid blue line is the theoretical sinc^2 function. The vertical red lines represent the channels. (b) Wavelengths of 80 ITU channels. (c) Schematic of 40 different user pairs performing quantum communication with unique/independent polarization-entangled states.

7.2.3 Multi-user source of hyper-entangled photon pairs

Hyper-entanglement adds another layer of security because now the photons are simultaneously entangled in two degrees of freedom. If, due to decoherence, the entanglement of photons in one degree of freedom washes away, then the entanglement of another degree of freedom can still be used. From our proposed fully guided wave schemes, completely fiber-integrated hyper-entangled or hybrid-entangled multi-user sources can also be explored. Along with polarization, the photons can also be entangled in another degree of freedom, like energy-time or time-bin, to get a hyper-entangled state in the output. For example, our presented multi-user source can be used to generate a hyper-entangled state (polarization and energy-time) by passing

the polarization-entangled photons further through the Franson interferometer to create an energy-time entanglement [22, 23, 151]. The fiber-integrated approach can also be explored to implement a hybrid-entangled source, where the photon is entangled in, say, path and polarization [28].

7.2.4 On-chip integrated source

On-chip integrated photonics is a fast-growing field where components such as waveguides, modulators, detectors, and lasers can be integrated into a single chip, and these systems can manipulate and transmit optical signals very efficiently. Their compatibility with existing electronic circuits allows seamless integration, which can enhance the overall performance of computing systems. The proposed work can also be extended into an on-chip integrated photonics for a compact and miniaturized quantum source, which can be easily mass-manufactured and deployed outside of a laboratory.

Appendix A

Appendix: Characterization of fiber-optical components

In this section, we show the characterization of fiber optical components that were used in the experiments. We measure these passive optical components' insertion loss, bandwidth, and transmission profile, which is essential for understanding the expected change in the detected photon counts and their effect on the output results.

A.1 Characterization of WDM 775/1550nm

A wavelength division multiplexer (WDM) is a passive fiber-optical device that is used in optical communication. It can multiplex multiple wavelengths into one optical channel, and in the reverse direction, it can be used as a de-multiplexer. The WDM 775/1550 (FONTCANADA: FWDM-7815-FA-Y) is a 1x2 port configured bench top box packaged device to combine/split 780±50 nm and 1550±80 nm wavelengths. One port is known as the common port in which all these wavelengths

can propagate, and the other two ports are the 775-nm port and 1550-nm port. The 775-nm port allows 780±50 nm wavelength to propagate through it, and the 1550-nm port allows only 1550±80 nm to propagate. All three ports have single-mode fibers with FC/APC connectors, and the device's operating temperature is -20℃ to 60℃. The insertion loss of wavelength 775 nm and 1550 nm are ∼3 dB and ∼ 20 dB, respectively, in the 775-nm port, whereas ∼ 17 dB and ∼ 0.5 dB, respectively, in the 1550-nm port (as specified by the manufacturer).

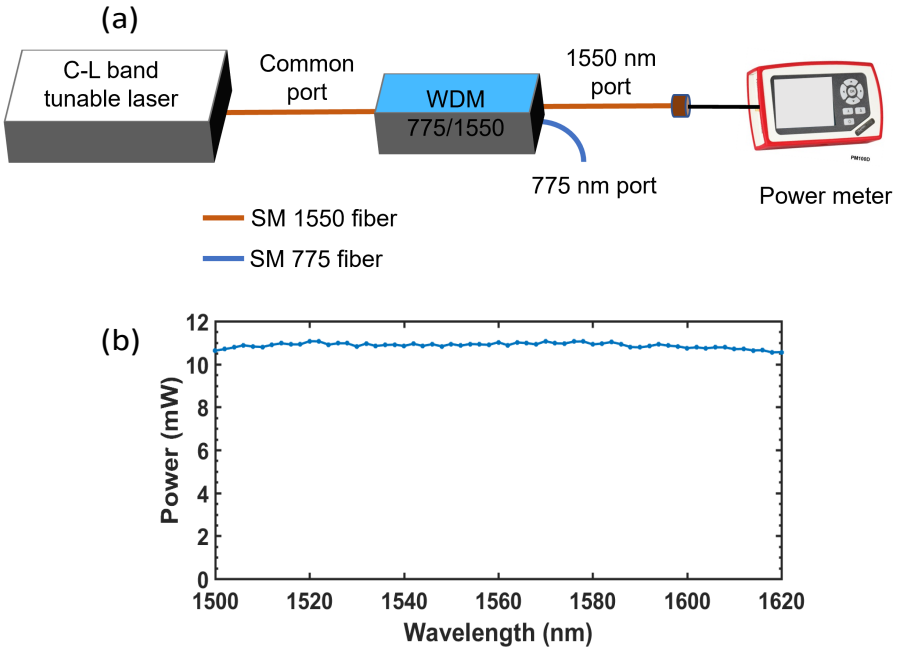

FIGURE A.1: (a) Experimental setup to measure the transmission profile, bandwidth, and insertion loss of the 1550-nm port of WDM 775/1550. (b) Transmission profile of 1550-nm port of WDM 775/1550 i.e., measured output power (at constant input power 15 mW) versus input wavelength.

Figure A.1(a) shows the experimental setup to measure the transmission profile, insertion loss, and bandwidth of the 1550-nm port of the WDM 775/1550 for telecom wavelengths. We connect the common port of WDM to a C-L band tunable laser (EXFO, T100S-HP-CL), which operates at constant power (15 mW), and the 1550-nm port to a photodiode and a power meter (Thorlabs). We tune the C-L band tunable laser to change the input wavelength of the WDM and record the output

TABLE A.1: Insertion loss of WDM at different telecom wavelengths. The insertion loss is calculated using $10 \times log_{10}(\frac{P_{out}}{P_{in}})$.

Wavelength (nm)	Insertion loss (dB)	Wavelength (nm)	Insertion loss (dB)
1500	-1.495	1556	-1.378
1502	-1.467	1558	-1.386
1504	-1.434	1560	-1.339
1506	-1.3946	1562	-1.394
1508	-1.418	1564	-1.343
1510	-1.426	1566	-1.354
1512	-1.386	1568	-1.378
1514	-1.358	1570	-1.319
1516	-1.378	1572	-1.358
1518	-1.378	1574	-1.362
1520	-1.319	1576	-1.327
1522	-1.323	1578	-1.323
1524	-1.382	1580	-1.378
1526	-1.358	1582	-1.362
1528	-1.358	1584	-1.335
1530	-1.418	1586	-1.374
1532	-1.362	1588	-1.426
1534	-1.406	1590	-1.434
1536	-1.390	1592	-1.410
1538	-1.382	1594	-1.374
1540	-1.406	1596	-1.402
1542	-1.366	1598	-1.414
1544	-1.406	1600	-1.446
1546	-1.374	1602	-1.434
1548	-1.414	1604	-1.450
1550	-1.370	1606	-1.434
1552	-1.402	1608	-1.434
1554	-1.370	1610	-1.467

power of the 1550-nm port. The transmission profile is shown in Fig. A.1(b) and TABLE A.1 indicates that the insertion loss has a negligible dependency on the telecom wavelength, and the WDM can easily pass 1500 nm to 1620 nm wavelengths. We measure an insertion loss of $\sim$ 1.37 dB in the 1550-nm port of WDM at 1550 nm.

A.2 Characterization of C-L band digital tunable filter

A digital tunable filter is an active optical device i.e. it requires an external power supply to operate, though this does not amplify or modify the signal. This device is used in optical telecommunication to filter out the selected wavelength from a band (i.e. it allows only the selected wavelength to pass through it and rejects the other wavelengths).

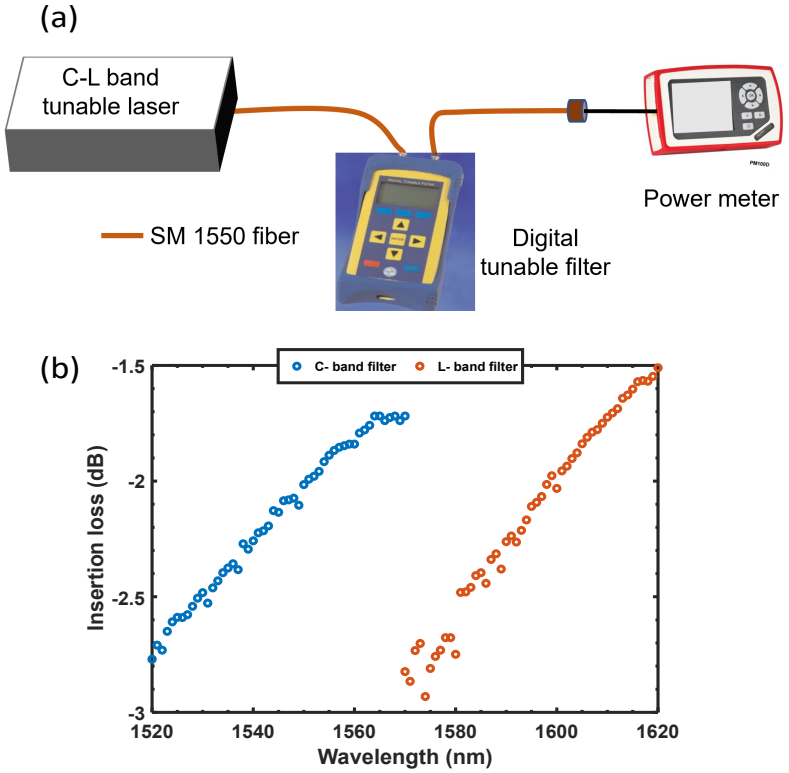

FIGURE A.2: (a) Experimental setup to characterize the digital tunable filter insertion loss at different wavelengths. (b) Insertion loss versus pump wavelength.

The C and L band digital tunable filters (OZ Optics: TF-100-3A3A-1520/1570-9/125-S-60-1.2 and TF-100-3A3A-1570/1620-9/125-S-60-1.2) are 1x1 port-configured packaged devices that can be tuned to filter the required wavelength from a band.

TABLE A.2: Insertion loss of C-L band digital tunable filters at different telecom wavelengths. The insertion loss is calculated using $10 \times log_{10}(\frac{P_{out}}{P_{in}})$.

Wavelength (nm)	Insertion loss (dB)	Wavelength (nm)	Insertion loss (dB)
1520	-2.769	1572	-2.732
1522	-2.731	1574	-2.931
1524	-2.608	1576	-2.758
1526	-2.589	1578	-2.676
1528	-2.541	1580	-2.748
1530	-2.482	1582	-2.479
1532	-2.461	1584	-2.408
1534	-2.395	1586	-2.442
1536	-2.357	1588	-2.314
1538	-2.271	1590	-2.261
1540	-2.258	1592	-2.263
1542	-2.214	1594	-2.168
1544	-2.127	1596	-2.091
1546	-2.084	1598	-2.014
1548	-2.073	1600	-2.031
1550	-2.015	1602	-1.935
1552	-1.978	1604	-1.877
1554	-1.915	1606	-1.810
1556	-1.867	1608	-1.777
1558	-1.846	1610	-1.723
1560	-1.839	1612	-1.686
1562	-1.778	1614	-1.627
1564	-1.718	1616	-1.570
1566	-1.738	1618	-1.568
1568	-1.718	1620	-1.510
1570	-1.718		

The C-band digital tunable filter has a tuning range of 1520-1570 nm, and the L-band digital tunable filter has a tuning range of 1570-1620 nm. The filter has a full-width half-maximum bandwidth (FWHM) of $\sim$ 1-1.2 nm, and the specified insertion loss is less than 3 dB. We characterize the digital tunable filter by measuring its insertion loss profile and maximum insertion loss at different C-L band telecom wavelengths.

The experimental setup to measure the insertion loss of the digital tunable filter is

shown in Fig. A.2(a). We connect the input of the tunable filter to a C-L band tunable laser via a single mode (SM) 1550 fiber and the output to a photodiode and power meter via another SM 1550 fiber. For the transmission profile characterization, we set the laser at one particular wavelength and then tune the filter wavelength around that set wavelength, and we find that the filter has a Gaussian transmission profile with $\sim$ 1-1.2 nm FWHM bandwidth (result not shown here). To measure the insertion loss at different wavelengths (see Fig. A.2(b)), we operate the laser at constant power, set the filter at exactly the same wavelength as the laser, and record the power in the power meter. We then simultaneously tune the laser and filter wavelength to find the insertion loss at different wavelengths. It is evident from Fig. A.2(b) and TABLE A.2 that the insertion loss of digital tunable filter depends on wavelength and higher wavelengths of both tunable filters have a lower loss.

A.3 Characterization of C-L band splitter

The C-L band splitter (Lightel Technologies USA: Model number 500-48947-02-1) is a 1x2 port configured rugged packaged passive device to split the C-L telecom band into two parts such that the C-band goes in one port and the L-band goes into another port. All three ports of the C-L band splitter have single-mode fibers of 1-meter length with FC/APC connectors. According to the manufacturer, the C-band port (arm) has a wavelength range of $\sim$ 1500 nm - 1550 nm, and the L-band port (arm) $\sim$ 1550 nm - 1620 nm. In the reverse direction, this acts as a C-L band combiner. Fig. A.3(a) shows the experimental setup to characterize the C-L band splitter. We connect the common port of the C-L band splitter to a C-L band tunable laser and the output port to a photodiode and power meter. We vary the wavelength of the tunable laser (by keeping the laser power constant) and record the

output power of the C and L-arm. The observed transmission profile and insertion loss at different telecom wavelengths are shown in Fig. A.3(b) and TABLE A.3, respectively. The C-L band splitter splits at 1550 nm, and both C- and L-band ports have an insertion loss of < 1 dB.

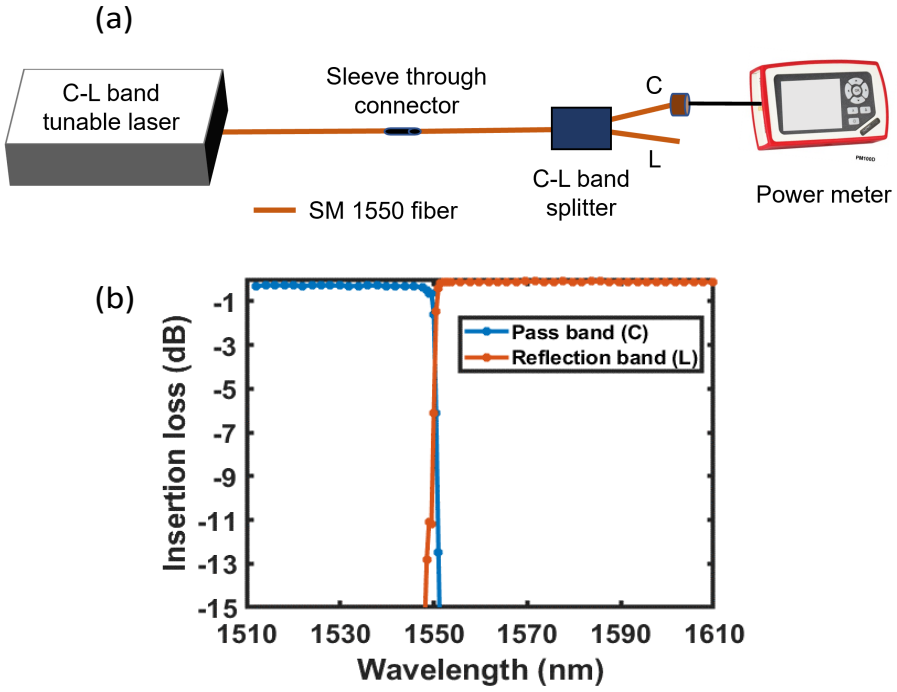

FIGURE A.3: (a) Setup for insertion loss measurement of C-L band splitter (Lightel, USA). (b) Transmission profile and insertion loss at different wavelengths.

A.4 Characterization of inline long-pass filter

Inline long pass fixed filter (OZ Optics: FF-21-1518:1650-9/125-S-50-3A3A-1-1-LP/REJ775) is a miniature package optimized to achieve high transmission for 1518 nm - 1650 nm. It is a passive optical device that is pigtailed on both sides with a single-mode fiber of 1 m length and terminated with FC/APC connectors. The device has a long pass filter installed to reject the lower wavelengths. The experimental setup to measure the insertion loss of the long pass filter at different telecom wavelengths is shown in Fig. A.4(a). The input side of the filter is connected to a

TABLE A.3: Insertion loss of C-L band splitter at different telecom wavelengths. The insertion loss is calculated using $10 \times log_{10}(\frac{P_{out}}{P_{in}})$.

C-arm/band response		L-arm/band response	
Wavelength (nm)	Insertion loss (dB)	Wavelength (nm)	Insertion loss (dB)
1512.03	-0.297	1545.78	-21.718
1514.05	-0.261	1547.7	-18.239
1516.03	-0.270	1548.5	-12.810
1518.07	-0.270	1549	-11.075
1519.99	-0.279	1549.5	-11.187
1521.97	-0.287	1550	-6.088
1523.95	-0.270	1550.5	-1.452
1525.94	-0.272	1551	-0.385
1527.92	-0.280	1551.5	-0.171
1529.89	-0.282	1552	-0.119
1531.88	-0.289	1552.5	-0.102
1533.87	-0.299	1553	-0.110
1535.85	-0.282	1553.73	-0.110
1537.84	-0.280	1555.71	-0.101
1539.82	-0.289	1557.71	-0.109
1541.8	-0.297	1559.69	-0.109
1543.79	-0.306	1561.68	-0.109
1545.78	-0.324	1563.68	-0.100
1547.7	-0.350	1565.66	-0.101
1548.5	-0.518	1567.65	-0.101
1549	-0.644	1569.64	-0.093
1549.5	-0.635	1571.64	-0.093
1550	-1.587	1573.64	-0.101
1550.5	-6.131	1575.62	-0.102
1551	-12.489	1577.62	-0.093
1551.5	-18.477	1579.61	-0.111
1552	-23.892	1581.61	-0.102
1552.5	-28.801	1583.6	-0.095
1553	-34.068	1585.6	-0.095
		1587.59	-0.104
		1589.58	-0.104
		1591.59	-0.104
		1593.58	-0.104
		1595.58	-0.104
		1597.57	-0.104
		1599.62	-0.104
		1601.58	-0.104
		1603.57	-0.113
		1605.57	-0.104
		1607.58	-0.113
		1609.58	-0.129

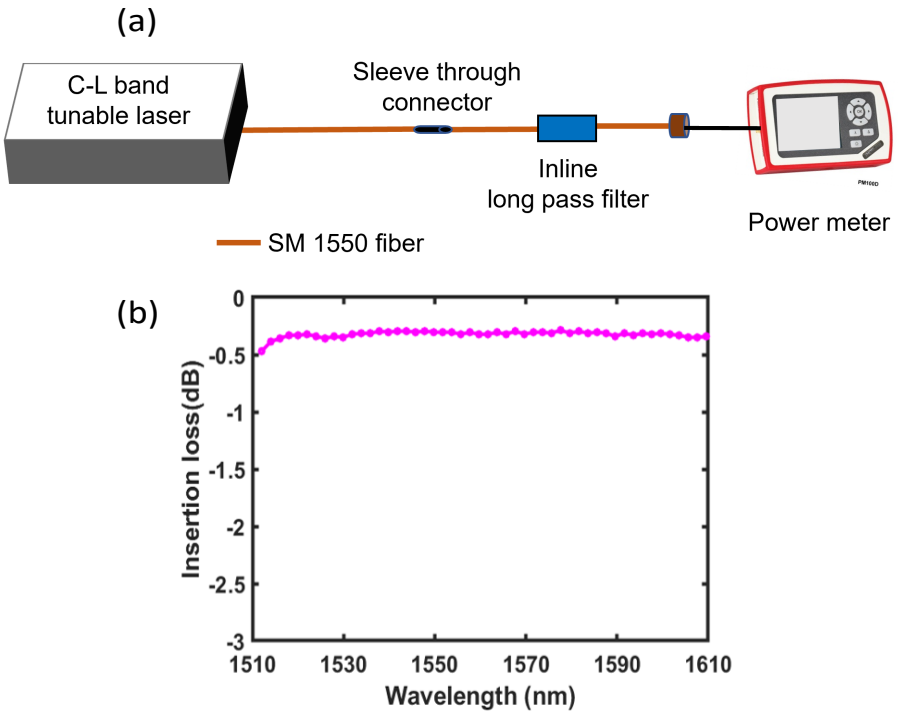

FIGURE A.4: (a) Experimental setup to measure the insertion loss of inline long pass fixed filter. (b) Insertion losses at different telecom wavelengths.

telecom band tunable laser, and the output is connected to a photodiode and power meter. We varied the wavelength of the laser from 1510 to 1610 nm and measured the insertion loss (see Fig. A.4(b)). We find that the filter has an insertion loss of < 0.5 dB within 1518 nm - 1610 nm. To measure the insertion loss of the long-pass filter at 775 nm, we replace the C-L band tunable laser with a tunable laser at 775 nm. We measure a high insertion loss of ≥ 74 dB at 775 nm.

All these fiber optical components were first characterized by classical light at the telecom wavelength, and then they were used in the experiments discussed in this thesis.

TABLE A.4: Insertion loss of inline long-pass filter at different telecom wavelengths. The insertion loss is calculated using $10 \times log_{10}(\frac{P_{out}}{P_{in}})$.

Wavelength (nm)	Insertion loss (dB)	Wavelength (nm)	Insertion loss (dB)
1512.04	-0.469	1563.68	-0.304
1514.05	-0.386	1565.67	-0.322
1516.04	-0.358	1567.66	-0.295
1518.01	-0.331	1569.65	-0.322
1519.99	-0.331	1571.64	-0.304
1521.97	-0.322	1573.64	-0.304
1523.96	-0.340	1575.63	-0.313
1525.94	-0.358	1577.62	-0.286
1527.92	-0.340	1579.62	-0.313
1529.89	-0.349	1581.62	-0.295
1531.88	-0.322	1583.6	-0.313
1533.87	-0.313	1585.6	-0.304
1535.85	-0.313	1587.59	-0.313
1537.84	-0.295	1589.58	-0.340
1539.82	-0.304	1591.59	-0.313
1541.8	-0.295	1593.58	-0.331
1543.79	-0.295	1595.59	-0.313
1545.78	-0.304	1597.58	-0.322
1547.76	-0.295	1599.58	-0.313
1549.75	-0.304	1601.58	-0.322
1551.74	-0.304	1603.57	-0.331
1553.73	-0.304	1605.61	-0.349
1555.72	-0.322	1607.58	-0.349
1557.71	-0.304	1609.57	-0.340
1559.69	-0.322	1611.65	-0.377
1561.68	-0.322		

A.5 Specs of other optical components and detectors

A.5.1 Variable optical attenuator

We have used OZ optics (BB-700-11-780-5/125-S-50-3A3A-1-1-LL) and Thorlabs (VOA780-APC) variable optical attenuator (VOA) in the experiments. These attenuators work at 775 nm, e.g., The BB-700-11-780-5/125-S-50-3A3A-1-1-LL has an operating range of 760 to 800 nm and an attenuation range of 0.8 to 65 dB; the VOA780-APC has an operating wavelength range of 760 to 800 nm and an attenuation range of 2.1 to 50 dB. VOA is a bidirectional device with a 1-m long single-mode fiber pigtail on each side. Each attenuator has a lens to collimate the light from the input fiber, a blocking device (which can be manually adjusted by a screw), and then a second lens, which is used to couple the light into the output fiber. The blocking device can be moved up and down through the screw to block/unblock the light from the collimating lens to the coupling lens. Thus, the coupling efficiency is changed until the desired attenuation is obtained. By manually adjusting the screw, we can get the desired attenuation.

A.5.2 Detectors and coincidence counters

In our experiments, we have used single-photon avalanche photodetectors (APDs) from two manufacturers, Aurea Technology and ID Quantique in free-running mode. The specifications of both detectors are listed below.

Aurea Technology: Model Number- SPD_OEM_NIR
(Serial number: SN_20030254030 and SN_20060254030)

Detection wavelengths	$900 - 1700$ nm
Detection efficiencies/Q.E. at 1550 nm	$10\%, 20\%, 30\%$
Dead time	10%Q.E. : $5 - 1000\,\mu s$
Dead time	20%Q.E. : $15 - 1000\,\mu s$
Dead time	30%Q.E. : $20 - 1000\,\mu s$
Dark counts	$< 1000\,$cps@10%Q.E. & 5 µs dead time
Timimg jitter	$\leq 200\,$ps@20%Q.E.

The absolute maximum detector input optical power is −65dBm CW i.e. the input power of the optical signal must not exceed −65dBm because higher power may cause permanent damage on the APD.

ID Quantique: Model Number- ID Qube-NIR-FR-MMF-LN

(Serial number: 2314006X010 and 2149040X010)

Detection wavelengths	$900 - 1700$ nm
Detection efficiencies/Q.E. @ 1550 nm	$10\%, 15\%, 20\%, 25\%, 30\%, 35\%$
Dead time	$100\,$ns $- 80\,\mu s$ in steps of 100 ns
Dark counts @ 50 µs dead time	$170\,$cps@10%Q.E.
Dark counts @ 50 µs dead time	$290\,$cps@15%Q.E.
Dark counts @ 50 µs dead time	$510\,$cps@20%Q.E.
Dark counts @ 50 µs dead time	$710\,$cps@25%Q.E.
Dark counts @ 50 µs dead time	$1070\,$cps@30%Q.E.
Dark counts @ 50 µs dead time	$1810\,$cps@35%Q.E.
Dark counts	$< 700\,$cps@20%Q.E. & 5 µs dead time
Timimg jitter	$\leq 200\,$ps@20%Q.E.

Both detectors generate the TTL pulse signal of 5V in the output, which can be further attenuated or inverted to match the compatibility of the time tagging or coincidence counter device.

We have used two time-tagging devices for coincidence measurement, which are discussed below.

PicoQuant: Model Number- PicoHarp 300

PicoHarp 300 TCSPC module has two independent channels with 4-ps temporal resolution suited for one sync and one detector or two detectors. It can perform histogramming with 65535 time-bins and 16-bit depth. The time-bin-width of PicoHarp 300 can be varied in 2^n ps, where n $\geq$ 2 (i.e. One can fix the coincidence window at 4, 8, 16, 32, 64, 128, 256, and 512 ps). The input pulse of PicoHarp 300 should be inverted, and the voltage level should be $<$ 1 V. So, we first attenuate the TTL pulse of detectors with a SIA400 attenuator/inverter (20 dB attenuation) and then feed this signal through SMA signal cable to PicoHarp 300.

Swabian Instruments: Model Number- Time Tagger X

Time tagger X has a 2-ps time resolution, and it can process 4 to 18 input channels, where each input signal must be -1.5 V to 1.5 V or a maximum of -3 V to 3 V. Here also, we first attenuate the TTL pulse of detectors with a SIA400 attenuator/inverter (20 dB attenuation) and then feed this signal through SMA signal cable to Time tagger X.

A.6 Sellmeier equations

The Sellmeier equation used in this thesis for 5% MgO doped lithium niobate is given as [103]

$$n^2 = a_1 + b_1 f + \frac{a_2 + b_2 f}{\lambda^2 - (a_3 + b_3 f)^2} + \frac{a_4 + b_4 f}{\lambda^2 - a_5^2} - a_6 \lambda^2 \tag{A.1}$$

where n is the refractive index, λ is wavelength, $a_{1,2,...6}$ and $b_{1,2,3,4}$ are constants and f is a function of temperature ($f = (T - 24.5)(T + 24.5 + 2 \times 273.16)$, T is the temperature in ℃). The coefficients a and b for the extraordinary ray refractive index (n_e) and the ordinary ray refractive index (n_o) are listed below.

n_e	n_o
$a_1 = 5.756$	$a_1 = 5.653$
$a_2 = 0.0983$	$a_2 = 0.1185$
$a_3 = 0.202$	$a_3 = 0.2091$
$a_4 = 189.32$	$a_4 = 89.61$
$a_5 = 12.52$	$a_5 = 10.85$
$a_6 = 1.32 \times 10^{-2}$	$a_6 = 1.97 \times 10^{-2}$
$b_1 = 2.86 \times 10^{-6}$	$b_1 = 7.94 \times 10^{-7}$
$b_2 = 4.7 \times 10^{-8}$	$b_2 = 3.13 \times 10^{-8}$
$b_3 = 6.11 \times 10^{-8}$	$b_3 = -4.64 \times 10^{-9}$
$b_4 = 1.52 \times 10^{-4}$	$b_4 = -2.19 \times 10^{-6}$

The Sellmeier equation used in this thesis for SiO_2 is given as [102]

$$n^2 = 1 + \frac{0.6961663\lambda^2}{\lambda^2 - (0.0684043)^2} + \frac{0.4079426\lambda^2}{\lambda^2 - (0.1162414)^2} + \frac{0.8974794\lambda^2}{\lambda^2 - (9.896161)^2} \tag{A.2}$$

where n is the refractive index and λ is the wavelength.

References

[1] Christopher C Gerry and Peter L Knight. *Introductory quantum optics*. Cambridge university press, 2023.

[2] Hugo Defienne, Matthew Reichert, and Jason W Fleischer. Adaptive quantum optics with spatially entangled photon pairs. *Physical review letters*, 121(23): 233601, 2018.

[3] Rupert Ursin, Felix Tiefenbacher, T Schmitt-Manderbach, Henning Weier, Thomas Scheidl, M Lindenthal, Bibiane Blauensteiner, Thomas Jennewein, J Perdigues, Pavel Trojek, et al. Entanglement-based quantum communication over 144 km. *Nature physics*, 3(7):481–486, 2007.

[4] Sören Wengerowsky, Siddarth Koduru Joshi, Fabian Steinlechner, Julien R Zichi, Bo Liu, Thomas Scheidl, Sergiy M Dobrovolskiy, René van der Molen, Johannes WN Los, Val Zwiller, et al. Passively stable distribution of polarisation entanglement over 192 km of deployed optical fibre. *npj Quantum Information*, 6(1):5, 2020.

[5] Vittorio Giovannetti, Seth Lloyd, and Lorenzo Maccone. Advances in quantum metrology. *Nature photonics*, 5(4):222–229, 2011.

[6] Paul-Antoine Moreau, Ermes Toninelli, Thomas Gregory, and Miles J Padgett. Imaging with quantum states of light. *Nature Reviews Physics*, 1(6):367–380, 2019.

[7] Milena D'Angelo and YH Shih. Quantum imaging. *Laser Physics Letters*, 2 (12):567, 2005.

[8] Stefano Pirandola, B Roy Bardhan, Tobias Gehring, Christian Weedbrook, and Seth Lloyd. Advances in photonic quantum sensing. *Nature Photonics*, 12(12):724–733, 2018.

[9] Lov K Grover. Quantum mechanics helps in searching for a needle in a haystack. *Physical review letters*, 79(2):325, 1997.

[10] Nicolas Gisin, Grégoire Ribordy, Wolfgang Tittel, and Hugo Zbinden. Quantum cryptography. *Reviews of modern physics*, 74(1):145, 2002.

[11] Thomas Jennewein, Christoph Simon, Gregor Weihs, Harald Weinfurter, and Anton Zeilinger. Quantum cryptography with entangled photons. *Physical review letters*, 84(20):4729, 2000.

[12] Matthias Keller, Birgit Lange, Kazuhiro Hayasaka, Wolfgang Lange, and Herbert Walther. Continuous generation of single photons with controlled waveform in an ion-trap cavity system. *Nature*, 431(7012):1075–1078, 2004.

[13] Guido Burkard. Connect the dots. *Nature Physics*, 2(12):807–808, 2006.

[14] Alain Aspect, Philippe Grangier, and Gérard Roger. Experimental realization of einstein-podolsky-rosen-bohm gedankenexperiment: a new violation of bell's inequalities. *Physical review letters*, 49(2):91, 1982.

[15] Hatam Mahmudlu, Robert Johanning, Albert Van Rees, Anahita Khodadad Kashi, Jörn P Epping, Raktim Haldar, Klaus-J Boller, and Michael

Kues. Fully on-chip photonic turnkey quantum source for entangled qubit/qudit state generation. *Nature Photonics*, 17(6):518–524, 2023.

[16] Michel H Devoret, Andreas Wallraff, and John M Martinis. Superconducting qubits: A short review. *arXiv preprint cond-mat/0411174*, 2004.

[17] Irfan Siddiqi. Engineering high-coherence superconducting qubits. *Nature Reviews Materials*, 6(10):875–891, 2021.

[18] Hartmut Häffner, Christian F Roos, and Rainer Blatt. Quantum computing with trapped ions. *Physics reports*, 469(4):155–203, 2008.

[19] Morten Kjaergaard, Mollie E Schwartz, Jochen Braumüller, Philip Krantz, Joel I-J Wang, Simon Gustavsson, and William D Oliver. Superconducting qubits: Current state of play. *Annual Review of Condensed Matter Physics*, 11(1):369–395, 2020.

[20] Jeremy L O'brien, Akira Furusawa, and Jelena Vučković. Photonic quantum technologies. *Nature Photonics*, 3(12):687–695, 2009.

[21] Dik Bouwmeester, Jian-Wei Pan, Klaus Mattle, Manfred Eibl, Harald Weinfurter, and Anton Zeilinger. Experimental quantum teleportation. *Nature*, 390(6660):575–579, 1997.

[22] DV Strekalov, TB Pittman, AV Sergienko, YH Shih, and PG Kwiat. Postselection-free energy-time entanglement. *Physical Review A*, 54(1):R1, 1996.

[23] Yin-Hai Li, Zhi-Yuan Zhou, Lan-Tian Feng, Wen-Tan Fang, Shi-long Liu, Shi-Kai Liu, Kai Wang, Xi-Feng Ren, Dong-Sheng Ding, Li-Xin Xu, et al. On-chip multiplexed multiple entanglement sources in a single silicon nanowire. *Physical Review Applied*, 7(6):064005, 2017.

[24] Paul G Kwiat, Klaus Mattle, Harald Weinfurter, Anton Zeilinger, Alexander V Sergienko, and Yanhua Shih. New high-intensity source of polarization-entangled photon pairs. *Physical Review Letters*, 75(24):4337, 1995.

[25] Ramesh Kumar, Vikash Kumar Yadav, and Joyee Ghosh. Postselection-free, hyperentangled photon pairs in a periodically poled lithium-niobate ridge waveguide. *Physical Review A*, 102(3):033722, 2020.

[26] Manuel Erhard, Mario Krenn, and Anton Zeilinger. Advances in high-dimensional quantum entanglement. *Nature Reviews Physics*, 2(7):365–381, 2020.

[27] Francesco Vedovato, Costantino Agnesi, Marco Tomasin, Marco Avesani, Jan-Åke Larsson, Giuseppe Vallone, and Paolo Villoresi. Postselection-loophole-free bell violation with genuine time-bin entanglement. *Physical review letters*, 121(19):190401, 2018.

[28] Sebastien Sauge, Marcin Swillo, Maria Tengner, and Anders Karlsson. A single-crystal source of path-polarization entangled photons at non-degenerate wavelengths. *Optics express*, 16(13):9701–9707, 2008.

[29] FNC Wong, JH Shapiro, and T Kim. Efficient generation of polarization-entangled photons in a nonlinear crystal. *Laser physics*, 16:1517–1524, 2006.

[30] Pisek Kultavewuti, Eric Y Zhu, Xingxing Xing, Li Qian, Vincenzo Pusino, Marc Sorel, and J Stewart Aitchison. Polarization-entangled photon pair sources based on spontaneous four wave mixing assisted by polarization mode dispersion. *Scientific reports*, 7(1):5785, 2017.

[31] Linda Sansoni, Fabio Sciarrino, Giuseppe Vallone, Paolo Mataloni, Andrea Crespi, Roberta Ramponi, and Roberto Osellame. Polarization entangled state measurement on a chip. *Physical review letters*, 105(20):200503, 2010.

[32] R Hafenbrak, SM Ulrich, P Michler, L Wang, A Rastelli, and OG Schmidt. Triggered polarization-entangled photon pairs from a single quantum dot up to 30 k. *New Journal of Physics*, 9(9):315, 2007.

[33] Jiho Park, Jinhyuk Bae, Heonoh Kim, and Han Seb Moon. Direct generation of polarization-entangled photons from warm atomic ensemble. *Applied Physics Letters*, 119(7), 2021.

[34] Stefano Pirandola. Limits and security of free-space quantum communications. *Physical Review Research*, 3(1):013279, 2021.

[35] Tae-Gon Noh, Heonoh Kim, Taehyoung Zyung, and Jaewan Kim. Efficient source of high purity polarization-entangled photon pairs in the 1550nm telecommunication band. *Applied physics letters*, 90(1), 2007.

[36] Philip G Evans, Ryan S Bennink, Warren P Grice, Travis S Humble, and Jason Schaake. Bright source of spectrally uncorrelated polarization-entangled photons with nearly single-mode emission. *Physical Review Letters*, 105(25): 253601, 2010.

[37] Panagiotis Vergyris, Florian Kaiser, Elie Gouzien, Grégory Sauder, Tommaso Lunghi, and Sébastien Tanzilli. Fully guided-wave photon pair source for quantum applications. *Quantum Science and Technology*, 2(2):024007, 2017.

[38] Thomas Lutz, Piotr Kolenderski, and Thomas Jennewein. Demonstration of spectral correlation control in a source of polarization-entangled photon pairs at telecom wavelength. *Optics letters*, 39(6):1481–1484, 2014.

[39] Olivier Alibart, Virginia D'Auria, Marc De Micheli, Florent Doutre, Florian Kaiser, Laurent Labonté, Tommaso Lunghi, Éric Picholle, and Sébastien Tanzilli. Quantum photonics at telecom wavelengths based on lithium niobate waveguides. *Journal of Optics*, 18(10):104001, 2016.

[40] Emanuel Knill, Raymond Laflamme, and Gerald J Milburn. A scheme for efficient quantum computation with linear optics. *nature*, 409(6816):46–52, 2001.

[41] Caterina Taballione, Tom AW Wolterink, Jasleen Lugani, Andreas Eckstein, Bryn A Bell, Robert Grootjans, Ilka Visscher, Dimitri Geskus, Chris GH Roeloffzen, Jelmer J Renema, et al. 8× 8 reconfigurable quantum photonic processor based on silicon nitride waveguides. *Optics express*, 27(19):26842–26857, 2019.

[42] Pawan Kumar, Mohammadreza Younesi, Sina Saravi, Frank Setzpfandt, and Thomas Pertsch. Group-index-matched frequency conversion in lithium niobate on insulator waveguides. *Frontiers in Photonics*, 3:951949, 2022.

[43] Xiongfeng Ma, Chi-Hang Fred Fung, and Hoi-Kwong Lo. Quantum key distribution with entangled photon sources. *Physical Review A—Atomic, Molecular, and Optical Physics*, 76(1):012307, 2007.

[44] James F Dynes, Hiroki Takesue, Zhiliang L Yuan, Andrew W Sharpe, K Harada, Toshimori Honjo, Hidehiko Kamada, Osamu Tadanaga, Yoshiki Nishida, Masaki Asobe, et al. Efficient entanglement distribution over 200 kilometers. *Optics express*, 17(14):11440–11449, 2009.

[45] Takahiro Inagaki, Nobuyuki Matsuda, Osamu Tadanaga, Masaki Asobe, and Hiroki Takesue. Entanglement distribution over 300 km of fiber. *Optics express*, 21(20):23241–23249, 2013.

[46] Sören Wengerowsky, Siddarth Koduru Joshi, Fabian Steinlechner, Hannes Hübel, and Rupert Ursin. An entanglement-based wavelength-multiplexed quantum communication network. *Nature*, 564(7735):225–228, 2018.

[47] Siddarth Koduru Joshi, Djeylan Aktas, Sören Wengerowsky, Martin Lončarić, Sebastian Philipp Neumann, Bo Liu, Thomas Scheidl, Guillermo Currás Lorenzo, Željko Samec, Laurent Kling, et al. A trusted node–free eight-user metropolitan quantum communication network. *Science advances*, 6(36): eaba0959, 2020.

[48] Rui Wang, Obada Alia, Marcus J Clark, Sima Bahrani, Siddarth Koduru Joshi, Djeylan Aktas, George T Kanellos, Matej Peranić, Martin Lončarić, Mario Stipčević, et al. A dynamic multi-protocol entanglement distribution quantum network. In *2022 Optical Fiber Communications Conference and Exhibition (OFC)*, pages 1–3. IEEE, 2022.

[49] Marcus J Clark, Obada Alia, Rui Wang, Sima Bahrani, M Peranić, Djeylan Aktas, George T Kanellos, Martin Loncaric, Ž Samec, Anton Radman, et al. Entanglement distribution quantum networking within deployed telecommunications fibre-optic infrastructure. In *Quantum Technology: Driving Commercialisation of an Enabling Science III*, volume 12335, pages 96–103. SPIE, 2023.

[50] H-J Briegel, Wolfgang Dür, Juan I Cirac, and Peter Zoller. Quantum repeaters: the role of imperfect local operations in quantum communication. *Physical Review Letters*, 81(26):5932, 1998.

[51] Han Chuen Lim, Akio Yoshizawa, Hidemi Tsuchida, and Kazuro Kikuchi. Broadband source of telecom-band polarization-entangled photon-pairs for

wavelength-multiplexed entanglement distribution. *Optics express*, 16(20): 16052–16057, 2008.

[52] Robert W Boyd. *Nonlinear optics*. Academic press, 2020.

[53] Bahaa EA Saleh and Malvin Carl Teich. *Fundamentals of photonics*. john Wiley & sons, 2019.

[54] Amnon Yariv, Pochi Yeh, and Amnon Yariv. *Photonics: optical electronics in modern communications*, volume 6. Oxford university press New York, 2007.

[55] A K Ghatak and K Thyagarajan. Optical electronics cambridge university press, 2004.

[56] Morton H Rubin, David N Klyshko, YH Shih, and AV Sergienko. Theory of two-photon entanglement in type-ii optical parametric down-conversion. *Physical Review A*, 50(6):5122, 1994.

[57] Yanhua Shih. Entangled biphoton source-property and preparation. *Reports on Progress in Physics*, 66(6):1009, 2003.

[58] Timothy E Keller and Morton H Rubin. Theory of two-photon entanglement for spontaneous parametric down-conversion driven by a narrow pump pulse. *Physical Review A*, 56(2):1534, 1997.

[59] Ramesh Kumar and Joyee Ghosh. Parametric down-conversion in ppln ridge waveguide: a quantum analysis for efficient twin photons generation at 1550 nm. *Journal of Optics*, 20(7):075202, 2018.

[60] Lufti Arif Bin Ngah. *All-optical synchronization for quantum networking*. PhD thesis, Université Nice Sophia Antipolis, 2015.

[61] MV Jabir and Goutam K Samanta. Robust, high brightness, degenerate entangled photon source at room temperature. *Scientific reports*, 7(1):12613, 2017.

[62] Hiroki Takesue and Kyo Inoue. 1.5-μm band quantum-correlated photon pair generation in dispersion-shifted fiber: suppression of noise photons by cooling fiber. *Optics express*, 13(20):7832–7839, 2005.

[63] Shin Arahira, Naoto Namekata, Tadashi Kishimoto, Hiroki Yaegashi, and Shuichiro Inoue. Generation of polarization entangled photon pairs at telecommunication wavelength using cascaded χ (2) processes in a periodically poled linbo 3 ridge waveguide. *Optics express*, 19(17):16032–16043, 2011.

[64] Xiyuan Lu, Wei C Jiang, Jidong Zhang, and Qiang Lin. Biphoton statistics of quantum light generated on a silicon chip. *ACS Photonics*, 3(9):1626–1636, 2016.

[65] Verification of single-photon output. `https://www.thorlabs.com/newgrouppage9.cfm?objectgroup_id=13675`.

[66] Leonard Mandel. Quantum effects in one-photon and two-photon interference. *Reviews of Modern Physics*, 71(2):S274, 1999.

[67] Ali Anwar, Chithrabhanu Perumangatt, Fabian Steinlechner, Thomas Jennewein, and Alexander Ling. Entangled photon-pair sources based on three-wave mixing in bulk crystals. *Review of Scientific Instruments*, 92(4), 2021.

[68] John F Clauser, Michael A Horne, Abner Shimony, and Richard A Holt. Proposed experiment to test local hidden-variable theories. *Physical review letters*, 23(15):880, 1969.

[69] Michael A Nielsen and Isaac L Chuang. *Quantum computation and quantum information*. Cambridge university press, 2010.

[70] John S Bell. On the einstein podolsky rosen paradox. *Physics Physique Fizika*, 1(3):195, 1964.

[71] Goh Koon Tong. *Possible Statistics from Bell Violations*. PhD thesis, National University of Singapore, 2014.

[72] Joseph B. Altepeter, Daniel F.V. James, and Paul G. Kwiat. *Qubit Quantum State Tomography*, pages 113–145. Springer Berlin Heidelberg, Berlin, Heidelberg, 2004. ISBN 978-3-540-44481-7. doi: 10.1007/978-3-540-44481-7_4. URL `https://doi.org/10.1007/978-3-540-44481-7_4`.

[73] Daniel FV James, Paul G Kwiat, William J Munro, and Andrew G White. Measurement of qubits. *Physical Review A*, 64(5):052312, 2001.

[74] Richard Jozsa. Fidelity for mixed quantum states. *Journal of modern optics*, 41(12):2315–2323, 1994.

[75] William K Wootters. Entanglement of formation of an arbitrary state of two qubits. *Physical Review Letters*, 80(10):2245, 1998.

[76] Alexander Ling, Matt Peloso, Ivan Marcikic, Antía Lamas-Linares, and Christian Kurtsiefer. Experimental e91 quantum key distribution. In *Advanced Optical Concepts in Quantum Computing, Memory, and Communication*, volume 6903, pages 129–133. SPIE, 2008.

[77] Jun Chen, Aaron J Pearlman, Alexander Ling, Jingyun Fan, and Alan L Migdall. A versatile waveguide source of photon pairs for chip-scale quantum information processing. *Optics express*, 17(8):6727–6740, 2009.

[78] Onur Kuzucu, Marco Fiorentino, Marius A Albota, Franco NC Wong, and Franz X Kärtner. Two-photon coincident-frequency entanglement via extended phase matching. *Physical review letters*, 94(8):083601, 2005.

[79] Alexios Beveratos, Rosa Brouri, Thierry Gacoin, André Villing, Jean-Philippe Poizat, and Philippe Grangier. Single photon quantum cryptography. *Physical review letters*, 89(18):187901, 2002.

[80] Paul G Kwiat, Aephraim M Steinberg, and Raymond Y Chiao. High-visibility interference in a bell-inequality experiment for energy and time. *Physical Review A*, 47(4):R2472, 1993.

[81] So-Young Baek and Yoon-Ho Kim. Spectral properties of entangled photon pairs generated via frequency-degenerate type-i spontaneous parametric down-conversion. *Physical Review A—Atomic, Molecular, and Optical Physics*, 77 (4):043807, 2008.

[82] Q Lin and Govind P Agrawal. Silicon waveguides for creating quantum-correlated photon pairs. *Optics letters*, 31(21):3140–3142, 2006.

[83] Akanksha Angural and Joyee Ghosh. Fully-guided polarization-correlated photon pairs at 1560 nm from a type-ii spdc-based source. *Optics Letters*, 49(3): 442–445, 2024.

[84] Ashish Samantaray, Vikash Kumar Yadav, Joyee Ghosh, and Vivek Venkataraman. Frequency-correlated photon-pairs tunable across the telecom spectrum via cascaded shg+ spdc in ppln. *Optics Communications*, 550: 129961, 2024.

[85] Shivani Sharma, Vivek Venkataraman, and Joyee Ghosh. Spectrally-pure integrated telecom-band photon sources in silicon. *Journal of Lightwave Technology*, 40(23):7529–7537, 2022.

[86] Rainer Kaltenbaek, Bibiane Blauensteiner, Marek Żukowski, Markus Aspelmeyer, and Anton Zeilinger. Experimental interference of independent photons. *Physical review letters*, 96(24):240502, 2006.

[87] Zachary H Levine, Jingyun Fan, Jun Chen, Alexander Ling, and Alan Migdall. Heralded, pure-state single-photon source based on a potassium titanyl phosphate waveguide. *Optics express*, 18(4):3708–3718, 2010.

[88] Peter J Mosley, Jeff S Lundeen, Brian J Smith, Piotr Wasylczyk, Alfred B U'Ren, Christine Silberhorn, and Ian A Walmsley. Heralded generation of ultrafast single photons in pure quantum states. *Physical Review Letters*, 100 (13):133601, 2008.

[89] Warren P Grice, Alfred B U'Ren, and Ian A Walmsley. Eliminating frequency and space-time correlations in multiphoton states. *Physical Review A*, 64(6): 063815, 2001.

[90] Andreas Christ, Kaisa Laiho, Andreas Eckstein, Thomas Lauckner, Peter J Mosley, and Christine Silberhorn. Spatial modes in waveguided parametric down-conversion. *Physical Review A—Atomic, Molecular, and Optical Physics*, 80(3):033829, 2009.

[91] CK Law, Ian A Walmsley, and JH Eberly. Continuous frequency entanglement: effective finite hilbert space and entropy control. *Physical Review Letters*, 84 (23):5304, 2000.

[92] Artur Ekert and Peter L Knight. Entangled quantum systems and the schmidt decomposition. *American Journal of Physics*, 63(5):415–423, 1995.

[93] Inna Krasnokutska, Jean-Luc J Tambasco, Xijun Li, and Alberto Peruzzo. Ultra-low loss photonic circuits in lithium niobate on insulator. *Optics express*, 26(2):897–904, 2018.

[94] Boris Desiatov, Amirhassan Shams-Ansari, Mian Zhang, Cheng Wang, and Marko Lončar. Ultra-low-loss integrated visible photonics using thin-film lithium niobate. *Optica*, 6(3):380–384, 2019.

[95] Cheng Wang, Xiao Xiong, Nicolas Andrade, Vivek Venkataraman, Xi-Feng Ren, Guang-Can Guo, and Marko Lončar. Second harmonic generation in nano-structured thin-film lithium niobate waveguides. *Optics express*, 25(6): 6963–6973, 2017.

[96] Iman Jizan, Luke G Helt, Chunle Xiong, Matthew J Collins, Duk-Yong Choi, Chang Joon Chae, Marco Liscidini, Michael J Steel, Benjamin J Eggleton, and Alex S Clark. Bi-photon spectral correlation measurements from a silicon nanowire in the quantum and classical regimes. *Scientific reports*, 5(1):12557, 2015.

[97] Martin Cordier. *Photon-pair generation in hollow-core photonic-crystal fiber*. PhD thesis, Université Paris Saclay (COmUE), 2019.

[98] Peter J Mosley, Jeff S Lundeen, Brian J Smith, and Ian A Walmsley. Conditional preparation of single photons using parametric downconversion: a recipe for purity. *New Journal of Physics*, 10(9):093011, 2008.

[99] Alfred B U'Ren, Konrad Banaszek, and Ian A Walmsley. Photon engineering for quantum information processing. *arXiv preprint quant-ph/0305192*, 2003.

[100] Mian Zhang, Cheng Wang, Rebecca Cheng, Amirhassan Shams-Ansari, and Marko Lončar. Monolithic ultra-high-q lithium niobate microring resonator. *Optica*, 4(12):1536–1537, 2017.

[101] Cheng Wang, Mian Zhang, Xi Chen, Maxime Bertrand, Amirhassan Shams-Ansari, Sethumadhavan Chandrasekhar, Peter Winzer, and Marko Lončar. Integrated lithium niobate electro-optic modulators operating at cmos-compatible voltages. *Nature*, 562(7725):101–104, 2018.

[102] Ian H Malitson. Interspecimen comparison of the refractive index of fused silica. *Josa*, 55(10):1205–1209, 1965.

[103] O Gayer, Z Sacks, E Galun, and A Arie. Temperature and wavelength dependent refractive index equations for mgo-doped congruent and stoichiometric linbo 3. *Applied Physics B*, 91:343–348, 2008.

[104] Marc Jankowski, Jatadhari Mishra, and MM Fejer. Dispersion-engineered nanophotonics: a flexible tool for nonclassical light. *Journal of Physics: Photonics*, 3(4):042005, 2021.

[105] LG Helt, MJ Steel, and JE Sipe. Spontaneous parametric downconversion in waveguides: what's loss got to do with it? *New Journal of Physics*, 17(1): 013055, 2015.

[106] Richard Wolf, Ingo Breunig, Hans Zappe, and Karsten Buse. Scattering-loss reduction of ridge waveguides by sidewall polishing. *Optics express*, 26(16): 19815–19820, 2018.

[107] Omshankar, Vivek Venkataraman, and Joyee Ghosh. Bright source of narrowband polarization-entangled photons from a thick type-ii ppktp crystal. *Optics Express*, 32(3):3470–3479, 2024.

[108] Taehyun Kim, Marco Fiorentino, and Franco NC Wong. Phase-stable source of polarization-entangled photons using a polarization sagnac interferometer. *Physical Review A—Atomic, Molecular, and Optical Physics*, 73(1):012316, 2006.

[109] Jianwei Wang, Stefano Paesani, Yunhong Ding, Raffaele Santagati, Paul Skrzypczyk, Alexia Salavrakos, Jordi Tura, Remigiusz Augusiak, Laura Mančinska, Davide Bacco, et al. Multidimensional quantum entanglement with large-scale integrated optics. *Science*, 360(6386):285–291, 2018.

[110] Evan Meyer-Scott, Nidhin Prasannan, Christof Eigner, Viktor Quiring, John M Donohue, Sonja Barkhofen, and Christine Silberhorn. High-performance source of spectrally pure, polarization entangled photon pairs based on hybrid integrated-bulk optics. *Optics express*, 26(25):32475–32490, 2018.

[111] Francesco S Pavone and Paul J Campagnola. *Second harmonic generation imaging*. CRC Press Boca Raton, 2014.

[112] André Müller, Ole Bjarlin Jensen, Angelika Unterhuber, Tuan Le, Andreas Stingl, Karl-Heinz Hasler, Bernd Sumpf, Götz Erbert, Peter E Andersen, and Paul Michael Petersen. Frequency-doubled dbr-tapered diode laser for direct pumping of ti: sapphire lasers generating sub-20 fs pulses. *Optics Express*, 19 (13):12156–12163, 2011.

[113] Ivan Sytcevich, Chen Guo, Sara Mikaelsson, Jan Vogelsang, Anne-Lise Viotti, Benjamín Alonso, Rosa Romero, Paulo T Guerreiro, Íñigo J Sola, Anne L'Huillier, et al. Characterizing ultrashort laser pulses with second harmonic dispersion scans. *Journal of the Optical Society of America B*, 38(5):1546–1555, 2021.

[114] Christophe Couteau. Spontaneous parametric down-conversion. *Contemporary Physics*, 59(3):291–304, 2018.

[115] *https://www.hcphotonics.com/ppln-guide-overview*.

[116] Sam A Berry, Lewis G Carpenter, Alan C Gray, Peter GR Smith, and Corin BE Gawith. Zn-indiffused diced ridge waveguides in mgo: Ppln generating 1 watt 780 nm shg at 70% efficiency. *OSA continuum*, 2(12):3456–3464, 2019.

[117] Lewis G Carpenter, Sam A Berry, Rex HS Bannerman, Alan C Gray, and Corin BE Gawith. Zno indiffused mgo: Ppln ridge waveguides. *Optics express*, 27(17):24538–24544, 2019.

[118] WM Young, Martin M Fejer, Michel JF Digonnet, AF Marshall, and RS Feigelson. Fabrication, characterization and index profile modeling of high-damage resistance zn-diffused waveguides in congruent and mgo: lithium niobate. *Journal of lightwave technology*, 10(9):1238–1246, 1992.

[119] Alan C Gray, Sam A Berry, Lewis G Carpenter, James C Gates, Peter GR Smith, and Corin BE Gawith. Investigation of ppln waveguide uniformity via second harmonic generation spectra. *IEEE Photonics Technology Letters*, 32 (1):63–66, 2019.

[120] Matteo Santandrea, Michael Stefszky, Vahid Ansari, and Christine Silberhorn. Fabrication limits of waveguides in nonlinear crystals and their impact on quantum optics applications. *New Journal of Physics*, 21(3):033038, 2019.

[121] Djeylan Aktas, Bruno Fedrici, Florian Kaiser, Tommaso Lunghi, Laurent Labonté, and Sébastien Tanzilli. Entanglement distribution over 150 km in wavelength division multiplexed channels for quantum cryptography. *Laser & Photonics Reviews*, 10(3):451–457, 2016.

[122] Andrzej Gajewski and Piotr Kolenderski. Spectral correlation control in down-converted photon pairs. *Physical Review A*, 94(1):013838, 2016.

[123] Xian-Min Jin, Ji-Gang Ren, Bin Yang, Zhen-Huan Yi, Fei Zhou, Xiao-Fan Xu, Shao-Kai Wang, Dong Yang, Yuan-Feng Hu, Shuo Jiang, et al. Experimental free-space quantum teleportation. *Nature photonics*, 4(6):376–381, 2010.

[124] Gonzalo Carvacho, Emanuele Roccia, Mauro Valeri, Francesco Basso Basset, Davide Poderini, Claudio Pardo, Emanuele Polino, Lorenzo Carosini, Michele B Rota, Julia Neuwirth, et al. Quantum violation of local causality in an urban network using hybrid photonic technologies. *Optica*, 9(5): 572–578, 2022.

[125] Sébastien Tanzilli, Hugues De Riedmatten, Wolfgang Tittel, Hugo Zbinden, Pascal Baldi, Marc De Micheli, Daniel Barry Ostrowsky, and Nicolas Gisin. Highly efficient photon-pair source using periodically poled lithium niobate waveguide. *Electronics Letters*, 37(1):26–28, 2001.

[126] James Schneeloch, Samuel H Knarr, Daniela F Bogorin, Mackenzie L Levangie, Christopher C Tison, Rebecca Frank, Gregory A Howland, Michael L Fanto, and Paul M Alsing. Introduction to the absolute brightness and number statistics in spontaneous parametric down-conversion. *Journal of Optics*, 21(4): 043501, 2019.

[127] Marco Fiorentino, Sean M Spillane, Raymond G Beausoleil, Tony D Roberts, Philip Battle, and Mark W Munro. Spontaneous parametric down-conversion in periodically poled ktp waveguides and bulk crystals. *Optics express*, 15(12): 7479–7488, 2007.

[128] Valerio Scarani, Helle Bechmann-Pasquinucci, Nicolas J Cerf, Miloslav Dušek, Norbert Lütkenhaus, and Momtchil Peev. The security of practical quantum key distribution. *Reviews of modern physics*, 81(3):1301–1350, 2009.

[129] Artur K Ekert. Quantum cryptography based on bell's theorem. *Physical review letters*, 67(6):661, 1991.

[130] Isabelle Herbauts, Bibiane Blauensteiner, Andreas Poppe, Thomas Jennewein, and Hannes Huebel. Demonstration of active routing of entanglement in a multi-user network. *Optics express*, 21(23):29013–29024, 2013.

[131] Qiang Zhou, Wei Zhang, Tian-zhu Niu, Shuai Dong, Yi-dong Huang, and Jiang-de Peng. A polarization maintaining scheme for 1.5 μ m polarization entangled photon pair generation in optical fibers. *The European Physical Journal D*, 67:1–6, 2013.

[132] Yin-Hai Li, Zhi-Yuan Zhou, Zhao-Huai Xu, Li-Xin Xu, Bao-Sen Shi, and Guang-Can Guo. Multiplexed entangled photon-pair sources for all-fiber quantum networks. *Physical Review A*, 94(4):043810, 2016.

[133] Yiwen Huang, Juan Feng, Yuanhua Li, Zhantong Qi, Chuangyi Lu, Yuanlin Zheng, and Xianfeng Chen. High-performance hyperentanglement generation and manipulation based on lithium niobate waveguides. *Physical Review Applied*, 17(5):054002, 2022.

[134] Yun-Kun Jiang and Akihisa Tomita. The generation of polarization-entangled photon pairs using periodically poled lithium niobate waveguides in a fibre loop. *Journal of Physics B: Atomic, Molecular and Optical Physics*, 40(2):437, 2007.

[135] Bao-Sen Shi and Akihisa Tomita. Generation of a pulsed polarization entangled photon pair using a sagnac interferometer. *Physical Review A*, 69(1): 013803, 2004.

[136] Rui-Bo Jin, Ryosuke Shimizu, Kentaro Wakui, Mikio Fujiwara, Taro Yamashita, Shigehito Miki, Hirotaka Terai, Zhen Wang, and Masahide Sasaki. Pulsed sagnac polarization-entangled photon source with a ppktp crystal at telecom wavelength. *Optics Express*, 22(10):11498–11507, 2014.

[137] Yan Li, Zhi-Yuan Zhou, Dong-Sheng Ding, and Bao-Sen Shi. Cw-pumped telecom band polarization entangled photon pair generation in a sagnac interferometer. *Optics Express*, 23(22):28792–28800, 2015.

[138] Yoshiaki Tsujimoto, Motoki Tanaka, Nobuo Iwasaki, Rikizo Ikuta, Shigehito Miki, Taro Yamashita, Hirotaka Terai, Takashi Yamamoto, Masato Koashi, and Nobuyuki Imoto. High-fidelity entanglement swapping and generation of three-qubit ghz state using asynchronous telecom photon pair sources. *Scientific reports*, 8(1):1446, 2018.

[139] Meritxell Cabrejo-Ponce, Christopher Spiess, André Luiz Marques Muniz, Philippe Ancsin, and Fabian Steinlechner. Ghz-pulsed source of entangled photons for reconfigurable quantum networks. *Quantum Science and Technology*, 7(4):045022, 2022.

[140] Zhao-Huai Xu, Yin-Hai Li, Zhi-Yuan Zhou, Shi-Long Liu, Yan Li, Shi-Kai Liu, Chen Yang, Guang-Can Guo, and Bao-Sen Shi. High-quality versatile photonic sources for multiple quantum optical experiments. *Optics Express*, 28(4):5077–5084, 2020.

[141] Sebastian Philipp Neumann, Thomas Scheidl, Mirela Selimovic, Matej Pivoluska, Bo Liu, Martin Bohmann, and Rupert Ursin. Model for optimizing

quantum key distribution with continuous-wave pumped entangled-photon sources. *Physical review A*, 104(2):022406, 2021.

[142] Hiroki Takesue and Kaoru Shimizu. Effects of multiple pairs on visibility measurements of entangled photons generated by spontaneous parametric processes. *Optics Communications*, 283(2):276–287, 2010.

[143] Dietrich Dehlinger and MW Mitchell. Entangled photons, nonlocality, and bell inequalities in the undergraduate laboratory. *American Journal of Physics*, 70 (9):903–910, 2002.

[144] Alicia Negre, Renaud Mathevet, Benoit Chalopin, and Sébastien Massenot. Unexpected optimal measurement protocols in bell's inequality violation experiments. *American Journal of Physics*, 91(1):64–73, 2023.

[145] Nobuyuki Matsuda, Hanna Le Jeannic, Hiroshi Fukuda, Tai Tsuchizawa, William John Munro, Kaoru Shimizu, Koji Yamada, Yasuhiro Tokura, and Hiroki Takesue. A monolithically integrated polarization entangled photon pair source on a silicon chip. *Scientific reports*, 2(1):817, 2012.

[146] Xiaoying Li, Paul L Voss, Jay E Sharping, and Prem Kumar. Optical-fiber source of polarization-entangled photons in the 1550 nm telecom band. *Physical review letters*, 94(5):053601, 2005.

[147] Thomas Scheidl, Rupert Ursin, Alessandro Fedrizzi, Sven Ramelow, Xiao-Song Ma, Thomas Herbst, Robert Prevedel, Lothar Ratschbacher, Johannes Kofler, Thomas Jennewein, et al. Feasibility of 300 km quantum key distribution with entangled states. *New Journal of Physics*, 11(8):085002, 2009.

[148] Sören Wengerowsky, Siddarth Koduru Joshi, Fabian Steinlechner, Julien R Zichi, Sergiy M Dobrovolskiy, Rene Van der Molen, Johannes WN Los, Val

Zwiller, Marijn AM Versteegh, Alberto Mura, et al. Entanglement distribution over a 96-km-long submarine optical fiber. *Proceedings of the National Academy of Sciences*, 116(14):6684–6688, 2019.

[149] Toshimori Honjo, Sae Woo Nam, Hiroki Takesue, Qiang Zhang, H Kamada, Y Nishida, O Tadanaga, M Asobe, Burm Baek, Robert Hadfield, et al. Long-distance entanglement-based quantum key distribution over optical fiber. *Optics Express*, 16(23):19118–19126, 2008.

[150] Sebastian Philipp Neumann, Alexander Buchner, Lukas Bulla, Martin Bohmann, and Rupert Ursin. Continuous entanglement distribution over a transnational 248 km fiber link. *Nature Communications*, 13(1):6134, 2022.

[151] Panagiotis Vergyris, Florent Mazeas, Elie Gouzien, Laurent Labonté, Olivier Alibart, Sébastien Tanzilli, and Florian Kaiser. Fibre based hyperentanglement generation for dense wavelength division multiplexing. *Quantum Science and Technology*, 4(4):045007, 2019.

[152] Hiroshi Takahashi, Yoshinori Hibino, and Isao Nishi. Polarization-insensitive arrayed-waveguide grating wavelength multiplexer on silicon. *Optics letters*, 17(7):499–501, 1992.

[153] Nikolai Kiesel. *Experiments on multiphoton entanglement*. PhD thesis, lmu, 2007.

[154] Antonio Acín, Nicolas Brunner, Nicolas Gisin, Serge Massar, Stefano Pironio, and Valerio Scarani. Device-independent security of quantum cryptography against collective attacks. *Physical Review Letters*, 98(23):230501, 2007.

[155] Stefano Pirandola, Ulrik L Andersen, Leonardo Banchi, Mario Berta, Darius Bunandar, Roger Colbeck, Dirk Englund, Tobias Gehring, Cosmo Lupo, Carlo

Ottaviani, et al. Advances in quantum cryptography. *Advances in optics and photonics*, 12(4):1012–1236, 2020.

[156] Hyang-Tag Lim, Kang-Hee Hong, and Yoon-Ho Kim. Effects of polarization mode dispersion on polarization-entangled photons generated via broadband pumped spontaneous parametric down-conversion. *Scientific Reports*, 6(1): 25846, 2016.

[157] Misha Brodsky, Elizabeth C George, Cristian Antonelli, and Mark Shtaif. Loss of polarization entanglement in a fiber-optic system with polarization mode dispersion in one optical path. *Optics letters*, 36(1):43–45, 2010.

[158] Mark Shtaif, Cristian Antonelli, and Misha Brodsky. Nonlocal compensation of polarization mode dispersion in the transmission of polarization entangled photons. *Optics express*, 19(3):1728–1733, 2011.

[159] BW Hakki. Polarization mode dispersion in a single mode fiber. *Journal of lightwave technology*, 14(10):2202–2208, 1996.

[160] G. P. Agrawal. *Nonlinear Fiber Optics, 3rd edition.* Academic Press, 2001.

List of Publications

Journal publication included in this thesis

Published:-

1. **Vikash Kumar Yadav**, Vivek Venkataraman, and Joyee Ghosh, "Broadband telecom photon pairs from a fiber-integrated PPLN ridge waveguide", **Optics Letters** 47 (19), 5132-5135 (2022).

2. **Vikash Kumar Yadav**, Vivek Venkataraman, and Joyee Ghosh, "High-brightness fiber-coupled source of polarization-entangled photon pairs spanning the telecom C-and L-bands", **Optics** & **Laser Technology** 175, 110774 (2024).

3. **Vikash Kumar Yadav**, Vivek Venkataraman, and Joyee Ghosh, "Spectral purity of telecom photon pairs from on-chip LNOI waveguides: comparison between analytical and numerical calculations" **Quantum Inf Process** 24, 11 (2025).

4. **Vikash Kumar Yadav**, Vivek Venkataraman, and Joyee Ghosh, "Telecom source of tunable polarization-entanglement distribution up to 100-km for multi-user QKD over metro-area fiber-optic networks", **APL Quantum** 2 (1) (2025).

Other contributed publications

1. Ramesh Kumar, **Vikash Kumar Yadav**, and Joyee Ghosh, "Postselection-free, hyperentangled photon pairs in a periodically poled lithium-niobate ridge waveguide", **Physical Review A** 102(3), 033722 (2020).

2. Ashish Samantaray, **Vikash Kumar Yadav**, Joyee Ghosh, and Vivek Venkataraman, "Frequency-correlated photon pairs tunable across the telecom spectrum via cascaded SHG+SPDC in PPLN", **Optics Communications** 550, 129961 (2024).

Conference Proceedings

1. **Vikash Kumar Yadav**, Vivek Venkataraman, and Joyee Ghosh, "An efficient fiber-integrated broadband source of telecom photon-pairs", in **Frontiers in Optics + Laser Science 2022 (FIO, LS)**, Technical Digest Series (Optica PublishingGroup, 2022), paper JTu5A.38.

2. **Vikash Kumar Yadav**, Vivek Venkataraman, and Joyee Ghosh, "Fiber-coupled source of polarization-entanglement at $\sim$ 1550-nm," in **Optica Quantum 2.0 Conference and Exhibition**, Technical Digest Series (Optica Publishing Group, 2023), paper QW2A.39.

3. **Vikash Kumar Yadav**, Vivek Venkataraman, and Joyee Ghosh, "An Efficient Source of Polarization-Entangled Photon-Pairs at Telecom Wavelength," in **Frontiers in Optics + Laser Science 2023 (FiO, LS)**, Technical Digest Series (Optica Publishing Group, 2023), paper JTu5A.19.

4. **Vikash Kumar Yadav**, Omshankar, Akanksha Angural, and Joyee Ghosh, "Spectral correlations of photon-pairs: a comparison of SPDC-based sources," Bulletin of the **American Physical Society (2024)**.

5. Ramesh Kumar, **Vikash Kumar Yadav**, Vivek Venkataraman, and Joyee Ghosh, "Temporal Properties and Schmidt Decomposition of the Biphoton State in a ppLN Ridge Waveguide," in **Frontiers in Optics + Laser Science 2021 (FiO, LS)**, Technical Digest Series (Optica Publishing Group, 2021), paper JW7A.94.

6. Ashish Samantaray, **Vikash Kumar Yadav**, Joyee Ghosh, and Vivek Venkataraman, "Temperature-Tunable Telecom Photon-Pairs via Cascaded $\chi^{(2)}$ Process in PPLN Waveguide," in **Frontiers in Optics + Laser Science 2023 (FiO, LS)**, Technical Digest Series (Optica Publishing Group, 2023), paper JM7A.127.

Presentations in International/National Conferences

1. Oral presentation (Virtual): Efficient Second Harmonic Generation from a Telecom Laser in a Zn-indiffused MgO:PPLN Ridge waveguide.
   XLIV OSI Symposium on Frontiers in Optics and Photonics (FOP-OSI 2021), IIT Delhi, India, September 2021.

2. Poster presentation (Virtual): An efficient fiber-integrated broadband source of telecom photon-pairs.
   Frontiers in Optics and Laser Science (FiO+LS 2022), Rochester, New York, USA, October 2022.

3. Poster presentation: Analytical formulation of Schmidt decomposition in SPDC.
   XLV OSI Symposium in Optics, Photonics and Quantum Optics (COPaQ 2022), IIT Roorkee, India, November 2022.

4. Poster presentation (Virtual): Fiber-coupled source of polarization-entanglement at $\sim$ 1550 nm.
   Optica Quantum 2.0, Denver, Colorado, USA, June 2023.

5. Poster presentation: An Efficient Source of Polarization-Entangled Photon-Pairs at Telecom Wavelength.
   Frontiers in Optics and Laser Science (FiO+LS 2023), Tacoma, USA, October 2023.

6. Oral presentation (Virtual): Spectral correlations of photon-pairs: a comparison of SPDC-based sources.
   APS March Meeting 2024, Minneapolis, USA, March 2024.

Patents: Filed/Granted

1. **Filed Indian patent: Fiber-integrated broadband source of polarization-entangled photons in the telecom C- and L-bands**
   Inventors - Vikash Kumar Yadav, Joyee Ghosh
   Application number - 202311046589

2. **Granted Indian patent: System for generation of entangled photon pair for multi-user quantum communication**
   Inventors - Vikash Kumar Yadav, Joyee Ghosh
   Application number - 202411033430
   Patent number - 560305

Biography

Vikash Kumar Yadav was born in Ramchandrapura, Alwar, Rajasthan, India. He is currently a PhD scholar in Quantum Photonics Lab, Department of Physics, Indian Institute of Technology Delhi (IIT Delhi), where he is researching on PPLN-waveguide based entangled-photon sources for multi-user QKD over metropolitan-scale fiber-optic networks. He holds a Master of Science degree in Physics from IIT Madras, where he worked on Photoconductivity study of Methyl ammonium lead Iodide with degradation and device fabrication for solar cell applications. He completed his Bachelor of Science degree in Physics from Sri Venkateswara College, University of Delhi. His research interest spans quantum optics, quantum communication, quantum information, and integrated photonics. His work includes designing and characterization of fully fiber-integrated PPLN-waveguide based sources of spectrally correlated and polarization-entangled photons in telecom-band, efficient fiber-integrated quantum light source for multi-user QKD and communication over metro-area network, and on-chip source of spectrally pure telecom photon. He has authored and co-authored several peer-reviewed publications in international journals such as Optics Letters, Physical Review A, Optics and Laser Technology, Quantum Information Processing, Optics Communications, and APL Quantum. He has also presented his research work in several international conferences including Quantum 2.0, Frontiers in Optics and Laser Science, and APS March Meetings. He

hold an Indian patent on his name which was granted on 14th Feb 2025. His current research interest revolves around SPDC-based novel quantum light sources and integrated photonics.